A Thesis Submitted for the Degree of PhD at the University of Warwick

CROSSED BEAM STUDIES OF ION-MOLECULE REACTIONS.

by

MARTIN F JARROLD.

A thesis submitted for the degree of
Doctor of Philosophy
in the
University of Warwick
Department of Chemistry
and Molecular Sciences.

July 1980

CONTENTS

Acknowledgements.

I would like to thank my supervisor Dr D M Hirst for his encouragement and help during the course of this work. My thanks also go to Prof K R Jennings and members of the Warwick mass spectrometry research group for encouragement and useful discussion. I would also like to thank Mr C W Worland and Mr A H Wiles in the mechanical workshop for fabricating many of the components of the instrument referred to in this thesis. In addition I would like to thank Mr D Wreford-Bush for help and advice on some of the electronic components of the instrument. Finally I would like to thank Dr K Birkinshaw for teaching me so much in the early stages of this work.

An SRC studentship and financial support is acknowledged.

Declaration.

Parts of the work described in this thesis have been published, or accepted or submitted for publication in the scientific literature with the following references:

K Birkinshaw, D M Hirst, and M F Jarrold, J Phys E, 11, 1037, (1978).

M F Jarrold, K Birkinshaw, and D M Hirst, Mol Phys, 39, 787, (1980).

M F Jarrold and D M Hirst, Mol Phys, in press, (1980).

M F Jarrold and D M Hirst, Mol Phys, submitted, (1980).

In addition parts of this work have been presented at a NATO Advanced Study Institute on the "Kinetics of Ion-Molecule Reactions" at La Baule, France in 1978; a Faraday Discussion of the Chemical Society on the "Kinetics of State Selected Species" at Birmingham in 1979; and at the 28th Annual Conference on Mass Spectrometry and Allied Topics at New York, USA in 1980.

Some of the development work on the instrument described in this thesis was performed by Dr K Birkinshaw before I started, and some was performed in conjunction with Dr K Birkinshaw before he departed.

Summary.

A new crossed beam instrument for the study of ion-molecule collision processes is described. During the development work a novel method of focussing an ion beam from a quadrupole mass filter was devised. Using an electrostatic octopole lens it is possible to obtain low energy ion beams with narrow energy distributions and with intensities and angular distributions close to the fundamental space charge limit.

The aim of this work has been to investigate the dynamics of the reactions of diatomic ions with diatomic molecules. The results of a detailed study of the reactions

$$CO^+ + O_2 = CO_2^+ + O$$

$$CO^+ + NO = CO_2^+ + N$$

$$CO^+ + NO = (NCO)^+ + O$$

are presented and discussed. All the reactions were found to proceed by a direct mechanism over the energy range studied although there is substantial evidence for the coupling of the motion of all atoms in reactive collisions. At high energy the total cross sections decline as the dynamics become dominated by product stability restrictions and there is evidence for the formation of electronically excited product.

List of tables.

List of figures.

List of figures.

List of abbreviations.

QMF - quadrupole mass filter.

RPD - retarding potential difference.

S/N - signal to noise ratio.

FWHM - full width at half maximum.

CI - chemical ionisation or configuration interaction where applicable.

CM - centre of mass.

T - initial relative translational energy.

T' - final relative translational energy.

Q - translational exoergicity.

Q_{MP} - most probable translational exoergicity.

ΔE - standard energy change.

χ - centre of mass scattering angle.

CHAPTER 1.

Introduction.

The observation of reactive scattering provides the most direct probe of the collision dynamics of reacting particles. Historically the application of molecular beam techniques has progressed most rapidly in the field of neutral-neutral collisions. However since the difficulties in producing low energy ion beams were overcome, molecular beam techniques have been used in several laboratories to study ion-molecule reactions.

Because of the fundamental nature of the information obtained, molecular beam techniques provide the opportunity for strong interaction between theory and experiment, and have contributed much to our current understanding of the dynamics of simple ion-molecule reactions, and the effects of relative translational energy on chemical reactions in general.

A crossed beam apparatus is a useful tool for studying the dynamics of ion-molecule reactions because it provides information on both the velocity and angular distributions of the products. In addition some information on the total cross section can be derived from the data. By varying the translational energy of the ionic reactant it is possible to study the dynamics of an ion-molecule reaction as a function of initial translational energy.

As part of this work a new crossed beam apparatus has been developed for the study of ion-molecule collision processes. This will be described in detail in chapter 3. During the development work a novel simple method of focussing an ion beam from a quadrupole mass filter was devised. Using an electrostatic octopole lens it is possible to obtain ion beams with narrow energy distributions and with intensities and angular distributions close to the fundamental space charge limit.

A brief summary of the theoretical concepts applicable to the discussion of the kinematics, energetics, and dynamics of ion-molecule reactions is given in chapter 2, with a brief survey of the simple models used by previous workers to rationalise their experimental results. Some instrumental aspects of the study of the dynamics of ion-molecule reactions, and the presentation and interpretation of experimental data are also discussed in chapter 2.

A wide variety of ion-molecule reactions has been investigated by the molecular beam method, but with the exception of a few reactions of the type

$$A^+ + BC = AB^+ + C$$

the majority have been H atom abstraction or proton transfer reactions. In particular many reactions of the type

$$A^+ + H_2 = AH^+ + H$$

$$A^+ + BH = AH^+ + B$$

have been studied. Our current understanding of the dynamics of ion-molecule reactions is thus largely derived from many reactions which are likely to be special cases, not only because of the rapid transfer of a light atom, but also because the interaction times are short at the high relative velocities at which these studies were made. This is particularly true for the reactions with hydrogen even at very low energies. These features might be expected to promote the ultra direct dynamics observed in many studies.

The dynamics of the reactions of diatomic ions with diatomic molecules have not been extensively studied except for a few reactions of the type

$$AB^+ + H_2 = ABH^+ + H$$

Our understanding of these reactions is much less well developed than in the case of the reactions of an atomic ion with a diatomic molecule. This is in contrast to the situation in neutral chemistry, where there is substantial interest in the dynamics of reactions between two neutral diatomic species [1].

The aim of this work has been to investigate a series of atom transfer reactions of the type

$$AB^+ + CD = ABC^+ + D$$

The substantial experimental data measured during the course of this work for the reactions

$$CO^+ + O_2 = CO_2^+ + O \qquad 1.1$$

$$CO^+ + NO = CO_2^+ + N \qquad 1.2$$

$$CO^+ + NO = (NCO)^+ + O \qquad 1.3$$

are presented and discussed in chapters 4-6. This work produced the first reported observations of reactions 1.1-1.3. Previously the only reported reactions between CO^+

and O_2, and CO^+ and NO were charge transfer.

Reaction 1.1, although 0.58 ev [2] exothermic and spin allowed apparently possesses a translational energy threshold, as no CO_2^+ product is detected in thermal energy SIFT experiments. The reaction between CO^+ and NO was found to have two atom transfer channels. The first (reaction 1.2) is 0.81 ev [2] endothermic, and provides interesting contrasts with reaction 1.1. The second channel (reaction 1.3) is estimated to be 2.70 ev endothermic on the basis of <u>ab initio</u> SCF-CI calculations [3]. $(NCO)^+$ appears to be a minor product except in the high energy regime where the dynamics are dominated by product stability restrictions.

In the final chapter some general conclusions derived from the study of these reactions are discussed. Areas in which the instrument described here could be improved and suggestions for future work are also discussed.

CHAPTER 2.

Molecular beam studies of ion-molecule reactions.

2.1 Instrumentation.

A number of different molecular beam techniques have been developed to study the dynamics of ion-molecule reactions. The different techniques and instrumental advances have recently been reviewed [4]. A brief summary of the salient features of each technique, and a comparison of their advantages and disadvantages is given below.

Crossed beam and ion beam-collision cell instruments provide information on the angular and velocity distribution of the products. In general the crossed beam configuration is prefered because target gas motion in the collision cell instrument reduces resolution. However the gain in resolution obtained in the crossed beam configuration is achieved by sacrificing sensitivity. Absolute cross section measurements are possible with both types of instrument, but easier with the ion beam-collision cell configuration, since this simply requires measurement of target gas pressure and temperature, rather than absolute neutral beam speed and angular distributions. However there remain the additional problems of determining absolute detector efficiency and acceptance function. The lowest relative collision energy that can be achieved depends on the kinematics of the system being studied and the lower limit to the LAB ion kinetic energy. This is determined by the space charge defocussing of the ion beam and the surface charge effects and patch effects which afflict traditional electrostatic ion optics. Current state of the art instruments do not perform reliably at LAB energies very much below 1 ev.

Merged beam instruments, in which a high energy ion beam is merged with a high energy neutral beam (produced by charge transfer) are capable of attaining extremely low relative collision energies with high kinetic energy resolution in the CM system. However angular resolution is lost and merged beam instruments yield information only on the axial components of the product CM velocity. Absolute total cross section measurements require accurate measurement of the 3D spatial intensity distribution of the two beams. However high energy ion and neutral beams can be detected with high efficiency, so absolute cross section measurements are fairly routine. An advantage of the merged beam configuration is that exotic neutral species can be studied, though it is difficult to characterise the internal state distribution of the neutral.

Guided beam instruments are similar to beam-collision cell experiments except that high frequency multipole fields along the primary and secondary ion paths guide the beam from source to collision cell and from collision cell to detector. The use of rf guide fields in the collision zone enables low relative collision energies to be attained, but precludes measurement of angular distributions. However absolute total cross sections can be measured very accurately.

Ion beam fluorescence experiments are similar to beam-collision cell experiments except that the fluorescence from the collision products is detected. Even crude optical detectors provide much better resolution than can be obtained with translational energy selectors. However fluorescence detection can only be used for products in excited states having transitions within the acceptable range, with radiative lifetimes which are shorter than about 10^{-4} s. Under normal conditions the radiative distribution is expected to be spatially isotropic, so no information is available on the product angular distribution. Measurement of absolute total cross sections for production of a specific state is possible, but difficult since calibration involves a large number of optical and geometric factors. A real possibility for the future is the application of the laser-induced fluorescence method to ion-molecule reactions. This would permit measurement of product state populations for channels which are not spontaneously fluorescent. So far this method has only been applied to neutral beam collision experiments.

2.2 Presentation of data.

2.2.1 Velocity vector diagrams.

The interpretation of velocity and angular distribution data measured in the crossed beam experiment requires transformation from the laboratory (LAB) frame to the centre of mass (CM) coordinate system. Figure 1 shows a velocity vector Newton diagram relevant to the crossed beam problem, ie for the reaction $M1^+ + M2 = M3^+ + M4$ in which $M3^+$ is the detected product, the initial ion velocity vector is perpendicular to the neutral velocity vector, and scattering is considered in the plane of the two initial velocity vectors. The velocity vector diagram first introduced by Herschbach [5], is simply a way of expressing conservation of linear momentum for the collision.

2.2.2 Representation of intensities.

If the detector measures ion intensities $I_L(v,\theta,\phi)$ as a function of velocity and angle θ and ϕ, from figure 2 it can be seen that the fraction of incident flux scattered into solid angle dw and between v and v + dv is given by

$$I_L(v,\theta,\phi)\ v^2 \sin\theta\ d\theta\ d\phi = I_L(v,\theta,\phi)\ v^2\ dw\ dv.$$

Thus the volume elements in velocity space are not equal but tend to zero at the laboratory origin. This will distort the data and make any forward backward symmetry difficult to see.

If the volume elements are divided by v^2 , or equivalently if the scattered intensity is divided by v^2, the velocity space will have equal volume elements, and is called cartesian space. This representation first suggested by Wolfgang and Cross [6] is now extensively used. To be rigorous the transformation is given by [6]

$$P_c(v_x, v_y, v_z) = I(v, \theta, \phi)/v^2$$

where P_c is the probability function in cartesian coordinates and the intensities plotted on the contour diagram are proportional to the probability of finding a product ion with velocity vector of magnitude between v_x and $v_x + dv_x$,etc. This representation has the advantage that it introduces minimum distortion due to uncertainties in the centre of mass velocity, but the disadvantage that intensities are not directly related to the differential cross sections for forming products with a given relative velocity and scattering angle.

This problem can be overcome by using the CM polar coordinate system which has also been widely used. This representation also removes the distortion produced by laboratory polar coordinates but requires assumptions about the precise value of the CM velocity. In addition this representation can introduce more distortion into the data because of the limited resolving power of the instrument. These problems can be avoided by the use of the cartesian coordinate system. If distributions are not sharply peaked, however, care is required in interpreting the energetic implications of experimental results in cartesian coordinates.

If the detector, as is the case in this work, measures kinetic energy then the data must be first transformed to velocity space. In velocity space we require dv to be constant and so the energy distribution $I_L(E)$ is multiplied by the LAB velocity, v, to obtain the velocity distribution in LAB coodinates, $I_L(v)$.

As a result of these two transformations, if the energy distribution of the intensity is divided by the LAB velocity, v, then the transformation to a cartesian velocity space is achieved. These velocity distributions are now plotted along the directions in which they where measured, and finally points of equal intensity are joined together to give the intensity contour diagram.

2.2.3 Energetics.

A useful quantity for discussing the reaction energetics is the reaction exoergicity, Q, defined as

$$Q = T' - T$$

where T and T' are the initial and final relative translational energies. By conservation of energy

$$Q = -\Delta E - \Delta U$$

where $-\Delta E$ is the reaction exoergicity (ΔE is the standard energy change for the process) and ΔU is the difference between the internal energies of the reactants and products. For reactions in which the neutral product is atomic, and assuming that the reactants are in their ground states and the products in their ground electronic states, U', the product internal excitation must lie between zero and D, the dissociation energy of the product ion. Thus Q is bounded according to

$$-\Delta E > Q > -(D + \Delta E)$$

Circles of constant Q corresponding to these limits can then be drawn on the contour diagrams, and significant intensity outside the stability zone indicates either that the product is formed in an electronically excited state ($Q < -(D + \Delta E)$), or that the product is derived from the reaction of excited reactants ($Q > -\Delta E$).

2.3 Dynamics.

Neutral-neutral reactions generally take place on the ground electronic potential surface and there is often a large separation between the ground and first excited surface. In contrast in ion-molecule reactions there are usually several electronic states close to the ground state. This is because the systems involved are often "open shell", and thus there may be several surfaces which lie within a few ev of the ground state, and the situation is further complicated by the two manifolds of surfaces due to eg A^+ + BC and A + BC^+. Since ionisation energies usually differ by less than 5 ev these are apt to be interwoven in a potentially complicated manner. The dynamics of ion-molecule reactions are thus often profoundly influenced by intersections and avoided crossings of potential surfaces.

There are two types of curve crossing, adiabatic and diabatic. In the former, reactants approach slowly and states of the same symmetry do not cross. In the latter, reactants approach each other rapidly and retain their original electronic configuration even though, for their particular symmetry and spins, this results in their being on a surface which may not be of the lowest potential energy.

A rigourous theoretical treatment of the dynamics of an ion-molecule system would first require *ab initio* calculation of all the energetically accessible potential surfaces and then trajectory calculations on these surfaces

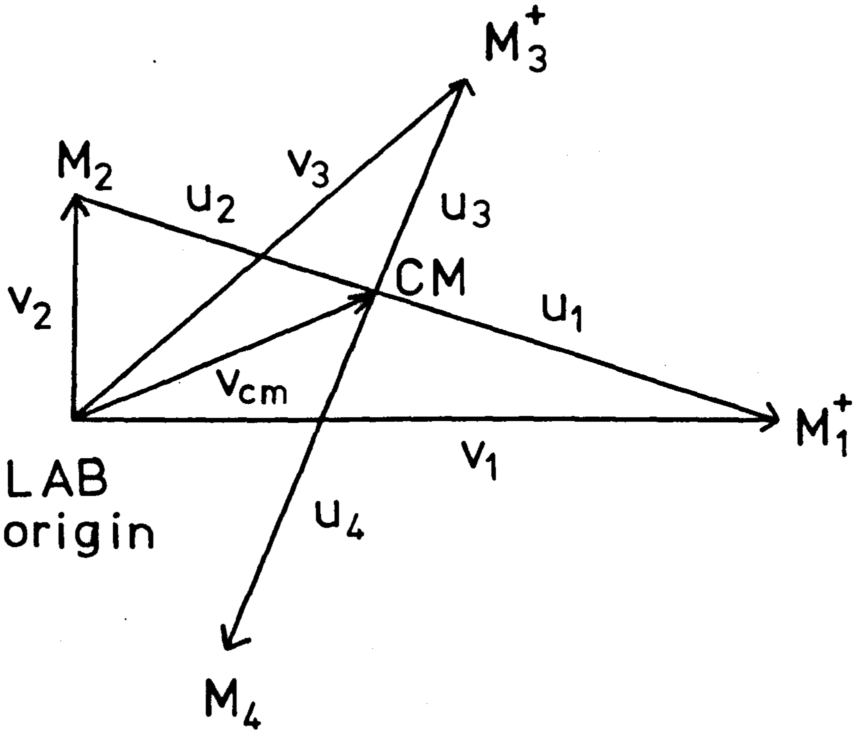

Figure 1. Velocity vector Newton diagram relevant to the crossed beam experiment. $V_{1,2,3}$ represent the LAB velocities and $U_{1,2,3,4}$ represent the CM velocities.

using monte carlo methods to select the initial conditions. To date such calculations have been performed for only a few of the simplest systems, because the calculation of potential surfaces of sufficient quality for trajectory calculations requires a large amount of computer time. For example trajectory calculations have been performed for $Ar^+ + H_2$ [7] and $H^+ + H_2$ [8], which can be considered representative of the present state of the art. In these examples potential surfaces were calculated using the diatomics in molecules method. Classical trajectories on the surface were calculated by numerical integration of the equations of motion, and the probability of a non-adiabatic transition occurring when passing an avoided crossing seam was assessed using the Landau-Zener expression. In both examples excellent agreement was found with experimental results.

For more complicated systems <u>ab initio</u> calculations of the relevant potential surfaces have been performed, eg N_2O^+ [9], CH_2^+ [10], and NH_2^+ [11], and these have been successfully used to rationalise the behaviour of the series of reactions involving the "intermediate quasi-molecule". For example the recent <u>ab initio</u> configuration interaction (CI) calculations of the triplet states of NH_2^+ [11], which can be considered as representative of the present state of the art, have been successfully used to rationalise the experimental data on the reactions

$$N^+ + H_2 = NH^+ + H$$

$$D_2^+ + N = ND^+ + D$$

Systems in which extensive ab initio calculations have been performed are obviously exceptions. In other systems it may be possible to derive certain features of the potential surfaces from orbital [12], or electronic [13] state correlations.

It is often useful in understanding the dynamics of ion-molecule reactions to use simple models which can be used as rigorous limiting cases to illuminate experimental results. Reaction mechanisms can be conveniently divided into two classes - direct and complex. Two types of limiting behaviour can be identified, situated at opposite extremes of the interaction spectrum. These are intermediate complex, and spectator stripping or ideal knockout which represent the sudden limit to direct reactions.

The term intermediate complex is not well defined, but here it will be taken to mean that the constituents of the system remain in normal bonding distances for a period which is sufficiently long for internal energy equilibration to occur and the subsequent unimolecular decomposition of the complex may be described by statistical theories. This then represents a rigorous limiting case.

As the intermediate complex may undergo several rotations before decomposing the intensity distribution is symmetric with respect to the plane passing through the centre of mass normal to the initial relative velocity vector. It should be noted though that care is required in interpreting symmetric distributions in terms of intermediate complex formation, since direct interactions can also give symmetric distributions, and such phenomena have been observed [14].

The shape of the CM angular distribution is determined solely by the partitioning of angular momentum of the complex between orbital and rotational motion of the products [15]. Product energy distributions P[T′] should be statistical and can be compared with the predictions of statistical theories. Early RRKM calculations [16] for the reaction

$$C_2H_4^+ + C_2H_4 = [C_4H_8^+]^* = C_3H_5^+ + CH_3$$

suggested that incomplete energy equilibration occurred, although more recent calculations [17] using a phase space approach suggest that this may not be the case. The failure of the earlier RRKM theory calculations probably arises from an inadequate treatment of angular momentum.

When a complex is formed at low energy there is normally a transition to a direct mechanism as the relative kinetic energy is increased, and the intermediate lifetime decreases. Examples of this behaviour are found in the reactions [18,19],

$$C_2H_4^+ + C_2H_4 = [C_4H_8^+]^* = C_3H_5^+ + CH_3$$

$$C_2H_2^+ + C_2H_4 = [C_4H_6^+]^* = C_3H_3^+ + CH_3$$

In low energy collisions substantial spiralling or snarling of trajectories due to the long range ion-induced dipole potential would be expected. Thus a question that arises is how low in initial kinetic energy can one go before the angular distribution characteristic of short range chemical forces is smeared out by long range interactions to give an isotropic intensity distribution, characteristic of intermediate complex formation. Both model calculations [20] and merged beam experiments [21] show that the differential cross sections can be anisotropic at very low energy (<0.015 ev) where substantial spiralling might be expected. Whether or not an intermediate complex is formed on collision (ie after spiralling) will depend on a number of factors [22]. Even if a potential well exists it may not be accessible to the reactants. Surface hopping as the reactants approach may make the ground state potential well inaccessible, as can configurational barriers. For example in the reaction

$$N_2^+ + D_2 = N_2D^+ + D$$

although the intermediate $N_2D_2^+$ is stable, no evidence is found for complex formation [23]. $N_2D_2^+$ presumably has the configuration $DNND^+$ which would require the D_2 to stretch to the point of dissociation as it approaches the N_2^+. The role played by configurational barriers might be expected to become more important as the complexity of the reactants increases.

Even if an accessible potential well exists intermediate complex formation still requires complete transformation of translational energy to internal energy. This is more favourable for polyatomic reagents because of the larger density of internal states.

In some cases short lived complexes with a lifetime comparable to the rotational period have been observed [24]. The dynamics of these reactions have been discussed using the osculating complex model [25].

Contour diagrams asymmetric with respect to the ±90° axis are generally interpreted in terms of a direct mechanism. An example of this is the well studied reaction [26]

$$Ar^{+} + H_2 = ArH^{+} + H$$

Here the interaction period is less than the rotational period.

The apparent directness of the interactions in H atom abstraction reactions initially studied by beam techniques invited the interpretation of some experimental results in terms of simple dynamical models which addressed themselves mainly to explaining the dependence of T' on T. A number of direct interaction models have been proposed.

The most simple is the spectator stripping model [27], which for the reaction $A^{+} + BC = AB^{+} + C$ predicts that the velocity of C is constant, ie there is no transfer of momentum from A^{+} to C. The model predicts that the internal energy of the product is equal to the sum of the reaction exoergicity and the kinetic energy of the ion relative to the abstracted atom. This model represents the sudden limit to direct reactions. Polanyi [28] has discussed the circumstances under which an ideal spectator stripping mechanism might operate, and it has been suggested [28,29] that the dynamical behaviour of some reactions may approach spectator stripping at sufficiently high energy. The main significance of this simple if unrealistic model is that it provides a reference point for discussing the dynamics of ion-molecule reactions.

The spectator stripping model was found to account satisfactorily for the experimental results on several systems involving H atom transfer at intermediate energies [30]. However substantial deviations have been found in both the low and high energy regimes. To account for these deviations a number of extensions have been proposed.

The modified stripping or polarisation model [31] proposes that the low energy deviations can be explained by considering the long range ion-induced dipole potential to accelerate the reactants as they approach, and decelerate them as they recede. Thus if the polarisability of the neutral product is less than the reactant neutral, the products will have a higher relative velocity than predicted by spectator stripping. This model accounts quantitatively for the hydrogen atom abstraction reactions of Ar^+, N_2^+, and CO^+ [26,31,32], although subsequent work using isotopic analogs suggested that a polarisation reflection model provided better agreement with experimental results [26].

Another model considers the deviations at low energy to arise from BC internal energy [33]. A further model, the DIPR (direct interaction with product repulsion) model [34], is conceptually quite different from spectator stripping, and assumes that the dynamics are dominated by the strong forces involved in breaking the BC bond. This model can also rationalise the results on a number of ion-molecule reactions and can also provide angular distributions.

It is somewhat surprising that these models which explain the deviations from spectator stripping in ways which are conceptually quite different, can all explain some of the experimental results on a number of H atom transfer reactions. This would suggest that variation of T' with T is a rather insensitive probe of the potential surfaces involved. This conjecture is supported by trajectory calculations [35]. In addition all these models predict either delta function or very narrow velocity distributions, which are not observed experimentally.

Classical trajectory calculations for $Ar^+ + D_2$ [35] have shown that the reaction proceeds by a mechanism that is quite different from spectator stripping, and that it is unlikely that an ideal stripping mechanism will be approached even at high energy. The dominance of the stripping features apparently arises from the special features of this mass combination which favour little momentum transfer to the departing atom.

These calculations showed that forward scattering can arise not only from grazing collisions, but also from a migration mechanism which involves strong interaction between all three atoms, and can lead to appreciable momentum transfer. This mechanism, in which A^+ initially interacts with B and finally forms a bond with C, is similar in some respects to the modified hard sphere impulsive model of George and Suplinskas [36]. The essence of this model is that the reactant ion, represented by a sphere, is incident upon a molecule represented by two hard spheres nearly in contact. Trajectories up to contact are governed by the ion-induced dipole potential. Energy and momentum transfer upon collision are regarded as occuring by a series of two body hard sphere interactions. The criteria for reaction is that the relative energy of the atoms of the proposed product molecule be less than the bond dissociation energy of that molecule. This model was applied to predicting the detailed dynamics of the $Ar^+ + D_2$ reactive, and non-reactive scattering, good agreement with experiment being found. An important conclusion from this work is that, within the framework of the model, the forward peaking of the differential cross sections is entirely dependent upon the attractive potential between the receding products a strongly backward peaked differential cross section being obtained when the potential is not present.

A simplified treatment of the three particle system has been given by Chang and Light [37]. Their model is essentially a polarisation reflection model in which the reactive configuration is fixed. Good agreement was found between theory and experiment for $Ar^+ + D_2$ reactive scattering angular and velocity distributions.

The modified elastic spectator model of Vestal et al [38,39] incorporates concepts employed in the impulsive reaction model of Chang and Light [37], the elastic spectator model of Herschbach [40], and the modified stripping model of Wolfgang et al [31]. This model was applied to proton transfer reactions in several polyatomic systems. Satisfactory agreement between theory and experiment was found for product CM angular distributions, and average relative translational energies.

The apparent success of these grossly over-simplified models in predicting the major features of the product distribution for a substantial number of H atom abstraction and proton transfer reactions suggests that for these reactions the major features of the product distributions are determined by kinematics and long range interactions, and the experimental data contain very little information about the short range interactions. The reasons for this may well lie in the special features of these reactions discussed in chapter 1.

In the high energy regime the dynamics are dominated by repulsive forces and product stability restrictions. The sequential impulse model, originally proposed by Bates, Cook, and Smith [41], but considerably refined by Mahan and coworkers [42], is a hard sphere impulse limit model, and shows how a series of sequential impulses, A^+ with B, and B with C, can lead to product stabilisation. The model can predict angular distributions and has been successful in rationalising the high energy behaviour of a number of H atom abstraction reactions [43].

CHAPTER 3.

Instrumentation and experimental techniques.

3.1 General description.

A crossed beam apparatus consists of three basic components - a source of a collimated beam of near mono-energetic ions, a neutral beam source, and a detector with an energy analyser and mass filter that can be scanned in at least one plane about the crossing region. These components are enclosed in a vacuum chamber that is rapidly pumped to attain a low working pressure.

Figure 3 shows a photograph of the apparatus. The vacuum chamber is in the centre of the photograph, with the lid raised showing the beam sources and detector. All the pumps are mounted beneath the vacuum chamber. The instrument consoles on the right contain detector and data aquisition control units. The console on the left contains control units for the beam sources and pumps.

Figures 4 and 5 show a photograph and diagram of the components inside the vacuum chamber. In figure 4 the ion beam source is on the left, and the neutral beam source in the centre. The detector which can be rotated in both planes about the crossing region is on the right.

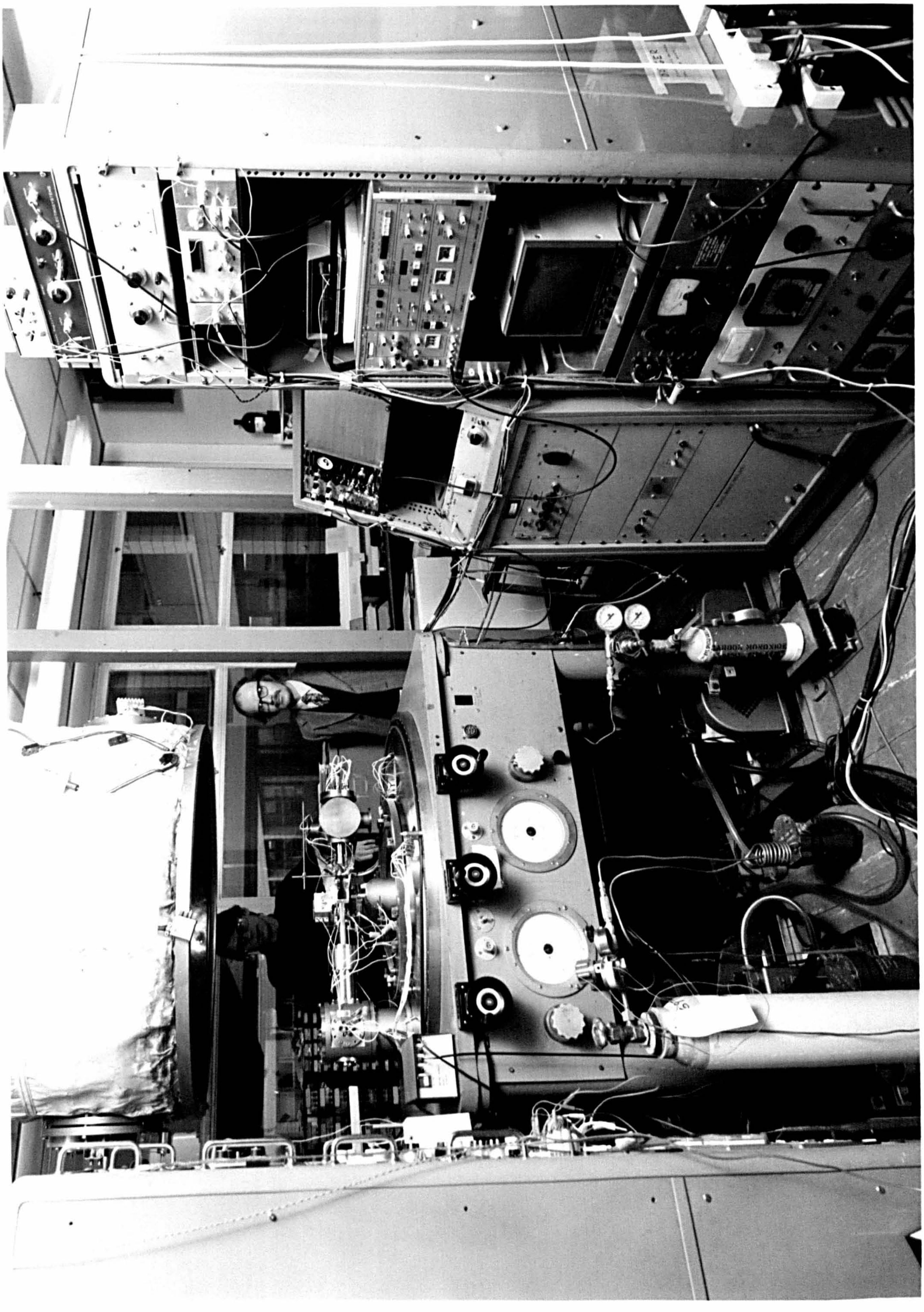

Figure 3. Photograph of the main components of the instrument.

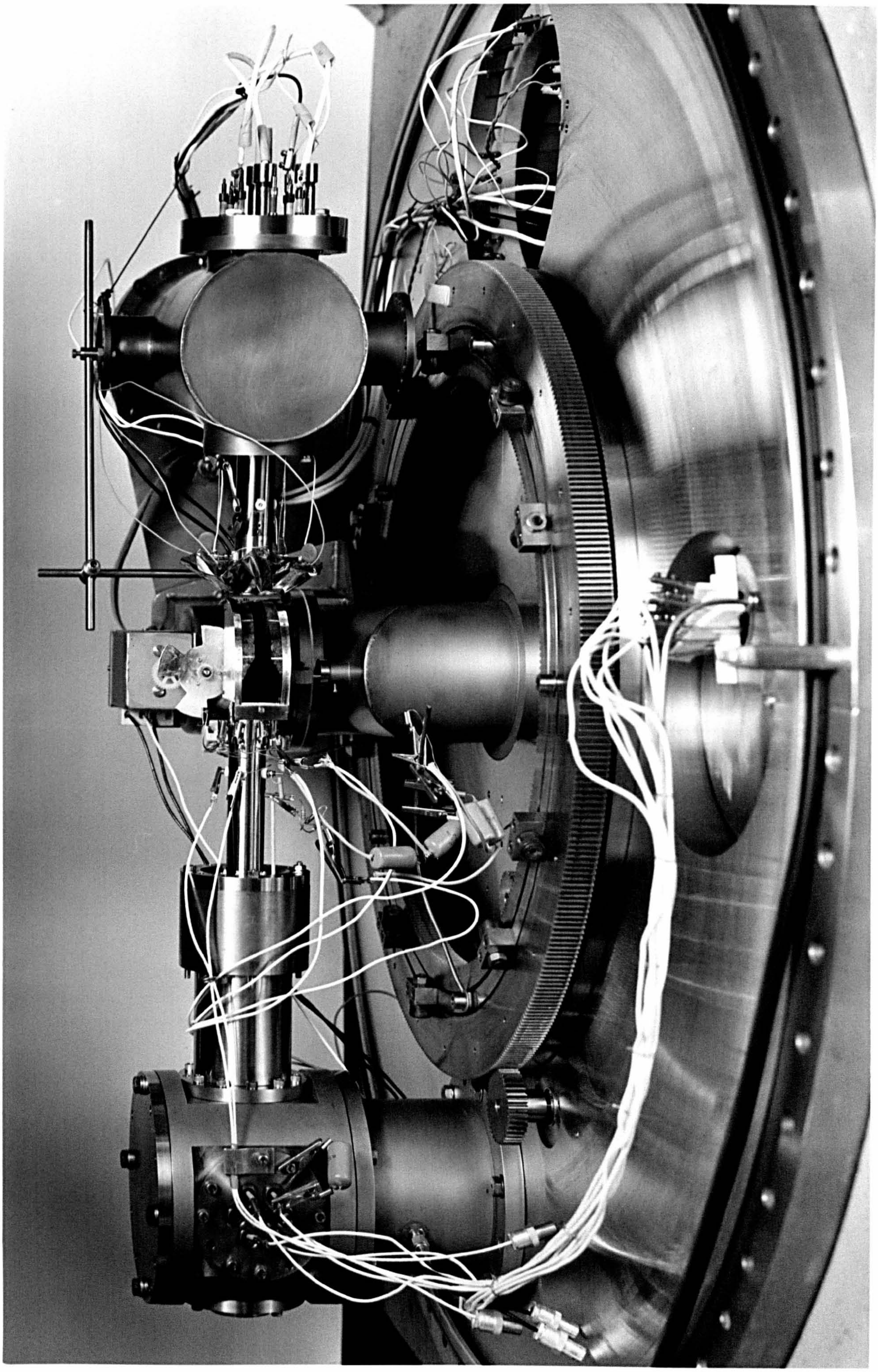

Figure 4. Photograph of the components inside the vacuum chamber.

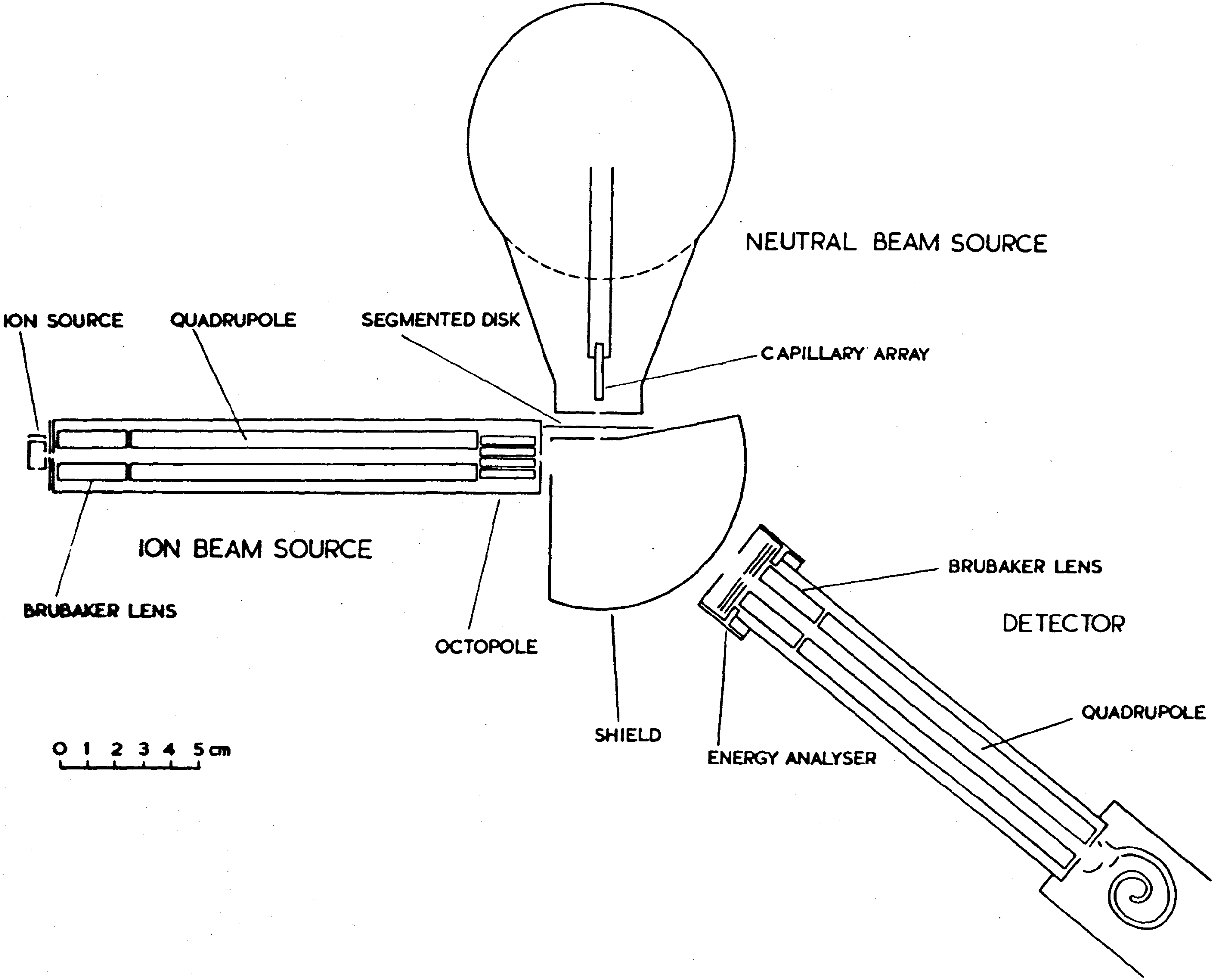

Figure 5. Diagram of the components inside the vacuum chamber.

3.2 Vacuum system.

The vacuum system consists of a large stainless steel chamber (see figure 3) originally constructed in 1965 for Shell (Thornton) Research Ltd. It is approximately 70 cm high and 100 cm in diameter, and totally encloses both beam sources and the detector. The chamber can be raised from the stainless steel base plate by means of a hoist. Most demountable joints are sealed by Viton-A O-rings, the remainder being sealed by gold O-rings.

Around the inside of the main chamber is a cold shield which can be maintained at liquid Nitrogen temperatures by means of a toroidal reservoir.

The main chamber is pumped by a 2000 l s^{-1} diffusion pump (Edwards "Diffstak" 250/1700M), backed by a 33.3 $m^3 h^{-1}$ rotary pump (Edwards ISC450B). The ion source housing and neutral beam chamber are both differentially pumped by 270 l s^{-1} diffusion pumps (Edwards "Diffstak" 100/300M), backed by 9 $m^3 h^{-1}$ rotary pumps (Edwards ES150). The advantages of the single structure pumping group have been discussed [44]. Of particular importance in the present application is the low back-streaming rate, and it was thus thought that the use of baffles over the pumps could be avoided, giving a higher effective pumping speed. However it was found that there was a degree of contamination derived from the pumps which was minimised by maintaining the cold shield at liquid Nitrogen temperatures. The level in the liquid Nitrogen reservoir was maintained by auto refill equipment (Thor Cryogenics S5050). After cleaning, instrument stability lasts for approximately 7 days, after which ion beam intensities begin to decline and the instrument must be dismantled and cleaned.

Pressures are monitored at various points in the system using a Vacuum Generators TCS5 ionisation gauge control unit. Ionisation gauge heads (Vacuum Generators VIG21) are mounted on both the main chamber and the neutral beam chamber, and connected to the control unit through a selector switch. Pirani gauges (Edwards model B5 gauge, Vacuum Generators PVG1 head) are mounted on the three backing lines to monitor the rough pressure. Typical pressures in the main chamber are 5×10^{-8} torr with both beam sources off, and 2×10^{-6} torr under operating conditions.

3.3 Ion beam source.

The design goal for the primary ion beam source was the production of a low energy, stable, intense, well collimated, mass analysed ion beam with narrow internal and translational energy distributions. Low angular and velocity distributions are important because, as consideration of a velocity vector diagram will show, these make major contributions to the total resolution.

In the ion beam source described here ions are produced by electron impact, mass analysed by a quadrupole mass filter, and focussed using an electrostatic octopole lens.

3.3.1 Ion source.

Electron impact (EI) is the most convenient and widely used technique for the production of reactant ions [4]. However, EI can produce uncertainties in the internal energy of the ion, due to long lived excited electronic states, and vibrational and rotational excitation in polyatomic ions. Beam attenuation [45] can be used to give an indication of the proportion of ions in excited electronic states in the beam. Chemical ionisation (CI) [46] and charge transfer ionisation [47] have been used in some studies. Both these techniques have limited applicability, although the CI source can be used to generate ions such as H_3^+ which cannot be made under EI conditions in any quantity. Photoionisation remains the best candidate for a source of internally state selected positive ions. However the development of a general purpose high intensity photoionisation source will probably have to await further development of laser technology.

In this instrument reactant ions are produced by electron impact in an EAI Quad 150 ioniser. The ions are formed in an ionisation chamber (the potential of the chamber determining the final ion energy) by an electron beam derived from a Tungsten wire filament of 0.15 mm diameter. They are then extracted through a 1 mm diameter hole in the ionisation chamber, and focussed into the quadrupole mass filter. Electrical supplies to the ion source are derived from the source quadrupole control unit (VG Q8). The ion intensities and energy distributions obtained with this ion source have proved entirely adequate.

3.3.2 Mass analysis.

Mass analysis of the primary ion beam is performed by a quadrupole mass filter (QMF) preceded by a Brubaker lens (see below). The theory of operation of a QMF and design criteria have been extensively reviewed [48], but will be briefly considered here as QMFs are used in both the source and detector, and an understanding of how the QMF functions is essential to understanding how the ion beam is focussed from the QMF.

A quadrupole mass filter consists of four conducting rods mounted equidistant from and parallel to a central axis. Although ideally the resultant field should have a hyperbolic cross section it can be adequately approximated by a set of circular rods of radius $1.148.r_o$, where r_o is the field radius. The four rods are connected in pairs and supplied with rf and superimposed dc voltages with adjacent rods being of opposite phase and polarity.

The equations of motion of the ions cannot be solved directly but require transformation to the standard Mathieu equation,

$$\frac{d^2x}{d\tau^2} + (a + 2\,q\,\cos2\tau)\,x = 0$$

$$\frac{d^2y}{d\tau^2} - (a + 2\,q\,\cos2\tau)\,y = 0$$

$$\text{where} \quad a = \frac{8\,e\,V_{DC}}{m\,r_o^2\,\omega^2}\,; \quad q = \frac{4\,e\,V_{RF}}{m\,r_o^2\,\omega^2}\,; \quad \tau = \frac{\omega t}{2}.$$

where V_{DC} and V_{RF} are the dc and peak rf voltages and ω is the angular frequency. Solutions of the Mathieu equation are characterised by regions of stability and instabilty. In stable regions the amplitude of the variable, x or y, remains bound, whereas in unstable regions it increases without bound. Whether the trajectory is stable or unstable is determined solely by the value of a and q. Solutions of the Mathieu equation are conveniently represented on a stability diagram, obtained by determining a region in the a,q plane which contains all those values of a,q which yield stable solutions. The stability diagram for the specific case of the mass filter is shown in figure 6.

For fixed values of r_o, ω, V_{DC}, and V_{RF} all ions of identical m/z will have the same operating point (a,q), and

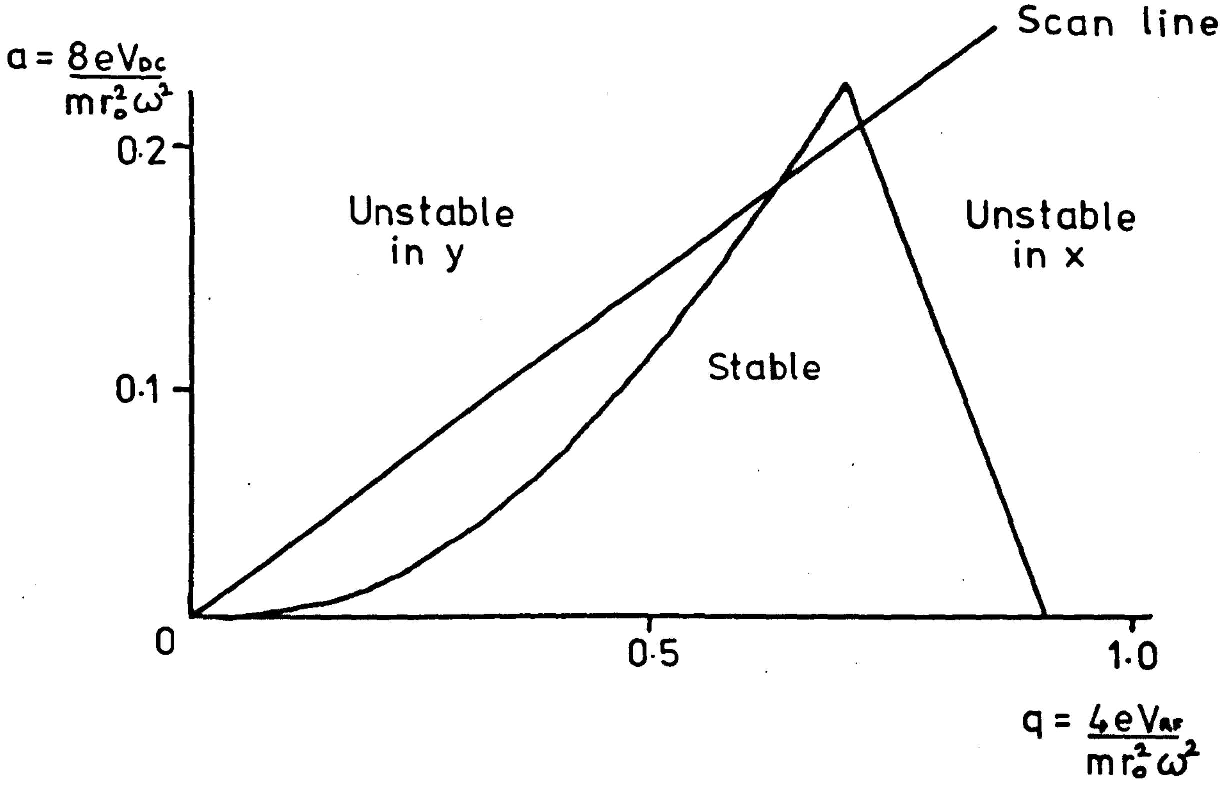

Figure 6. The stability diagram for the quadrupole mass filter

for a given ratio of V_{DC} to V_{RF} all values of a and q lie on a scan line which passes through the origin. Points on this line correspond to specific values of the ratio m/z and the interval of this value which lies within the stable region defines the range of masses with stable trajectories. If the ratio of V_{DC} to V_{RF} is increased the slope of the scanline is increased and passes nearer the apex of the stable region thus increasing the resolving power.

A simple physical appreciation of how a QMF works can be obtained by considering that in the x plane the ions sit in a potential well due to the positive dc potential on the rods. When the rf is applied light ions which respond sufficiently to the changing potential oscillate with increasing amplitude and are lost to the rods. The x plane is thus a high pass filter. In the y plane the ions sit on top of a potential hill due to the negative potential on the rods. In the absence of the rf all ions would thus be lost to the rods, however the rf stabilises the trajectories of the light ions as these ions are able to follow the rapidly changing potential. The y plane is thus a low pass filter. The combination of the x and y planes together gives a mass filter with a certain pass band.

The operation of the QMF has been extensively studied using computer simulation (ref. 49 gives an exhaustive bibliography to date). The mathematical methods that have been employed are analytical solution of the Mathieu equation , numerical integration of the Mathieu equation, matrix methods, and phase space dynamics. Interest has focussed mainly on examining the transmission of ions as a function of the ion entrance conditions and operating parameters of the QMF.

Fringing fields have a marked effect on the acceptance of the QMF [50,51]. As the ion enters the QMF a and q vary from zero to the full value. During this transit the working point lies above the y stability limit, and the ion receives a y directed momentum impulse which varies approximately exponentially with ramp length. This leads to a small effective aperture in the y direction, and discrimination against ions of low velocity and high mass. To overcome this problem Brubaker has suggested the use of a delayed dc ramp [52]. Computer studies indicate a large improvement in the maximum ion displacement - initial phase relationships [50]. A Brubaker lens (one form of delayed dc ramp), which consists of four short rods supplied only with rf voltages, precedes both the source and detector quadrupoles.

The primary ion beam QMF consists of a Vacuum Generators Q8 control unit, and an EAI analyser with rods 1/4" diameter and 5" long mounted on precision ground ceramic cylinders. The control unit has been modified so that the quadrupole axis potential can be floated in the range ±15 volts with respect to ground.

The resolution of a QMF depends on a number of factors: a) the number of rf cycles experienced and hence analyser length, rf frequency, and ion velocity; b) quadrupole entrance aperture diameter; and c) the ratio of peak rf voltage to dc voltage, which can be readily varied. In the work described here a relatively low resolution has been employed to maximise the transmission efficiency and obtain high ion currents.

3.3.3 Electrostatic octopole lens.

The use of quadrupole mass filters in ion beam sources has been avoided because of the wide angular and energy distribution of the emerging ions. Instead magnetic sector momentum analysers have been used. However these have the disadvantage that the ions must first be accelerated into the magnet and then retarded and focussed using a many element lens [46,53].

Before attempting to design a suitable focussing lens it is important to consider how the ions emerge from the QMF. The energy distribution of the emerging ions has been measured [54], and shows a low intensity high energy tail. Consideration of Paul's idealised quadrupole model shows that ions can have transverse energies as high as $E = 0.7\ V_{RF}$ ev [54] in the filter. If the quadrupole fields are terminated abruptly the emerging ions could have a correspondingly high transverse velocity. In a real quadrupole the output characteristics will be extensively modified by the exit ramp, and in addition the x, y, and z motion of the ions can become coupled in the fringing fields and provide a mechanism for broadening the lateral velocity distribution. It is relatively simple to remove the ions with high transverse velocities by only focussing ions emerging close to the quadrupole axis. In addition the broadening in the lateral velocity distribution can be minimised by accelerating the ions out of the quadrupole and reducing the time spent in the fringing fields.

Since no previous measurements of the angular distribution of ions emerging from the QMF have been reported a series of experiments were performed in which this was measured by scanning the detector. These experiments showed the angular distribution to be cross shaped with the extremities of the cross pointing towards the rods. The lobes pointing towards the negative rods were larger than those pointing towards the positive rods. Figure 7 shows the profile of an N_2^+ beam which displays the lobes clearly. Recent calculations of the ion exit distribution using numerical integration of the equations of motion [49], and of the ion spatial distribution in the mass filter [55], show a similar distorted cross shaped distribution, and indeed such a distorted cross shape would be expected - the emerging ions being to a certain extent focussed in the x plane, and defocussed in the y plane in the fringing fields.

To focus such a beam in two planes simultaneously an octopole was designed as shown in figure 8. The rods are 3.175 mm diameter and 20 mm long. They are mounted on a precision ground ceramic spacer on the same PCD as the quadrupole rods, with four of the rods coaxial with the quadrupole rods. Equipotential lines are shown in figure 9. The four rods marked positive are connected together as are those marked negative. It can be seen that the two

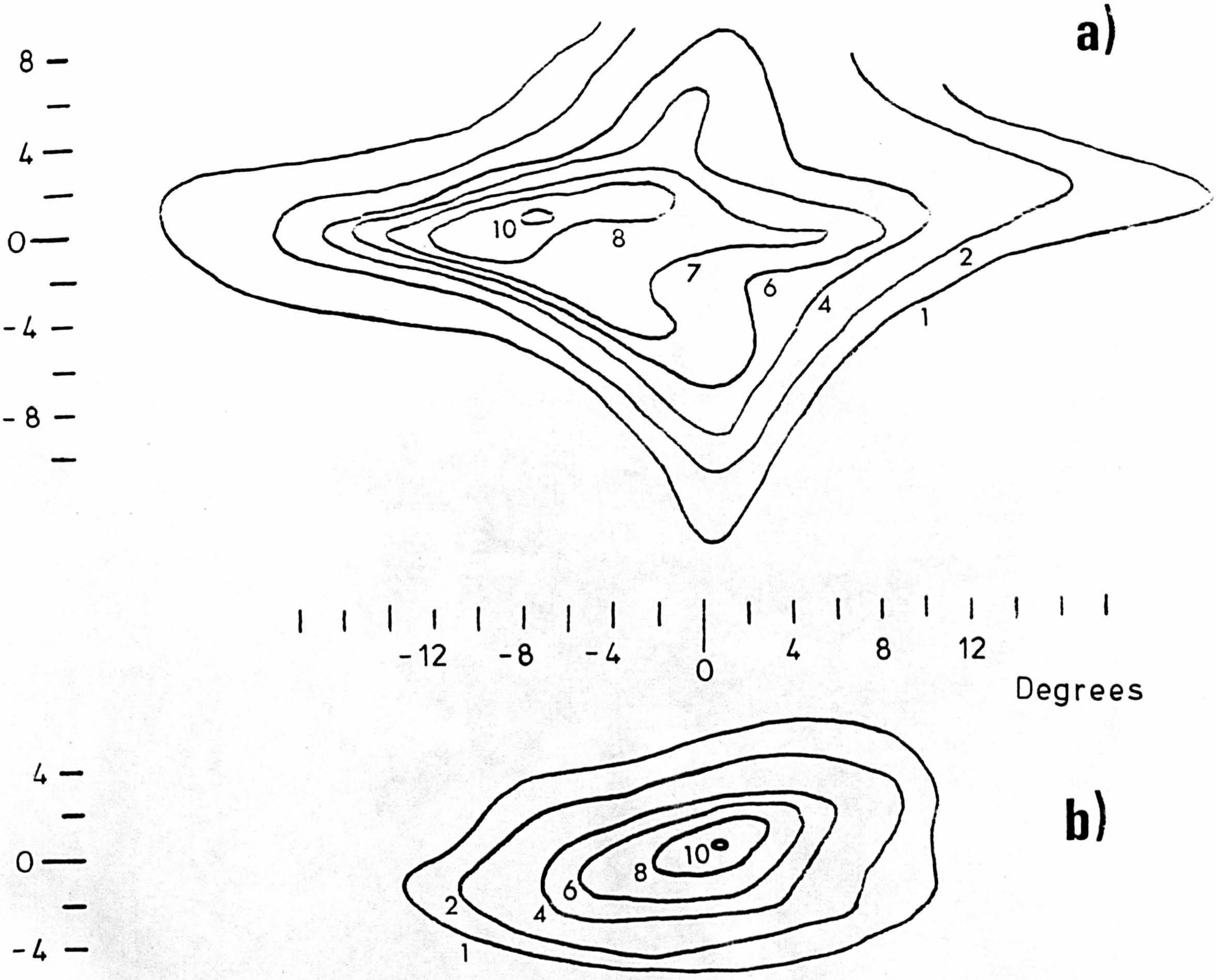

Figure 7. The profile of an N_2^+ (5 ev) beam from the quadrupole. The octopole exit plate was removed to measure these profiles. The octopole is floated at a) -2·4 V, and b) +3 V with respect to the quadrupole. Between -2·4 and +3 V the shape changes smoothly from a) to b). The quadrupole rods are at the extremities of the cross, the rods in the horizontal plane being negative. Both contour diagrams are separately normalised to a maximum of 10.

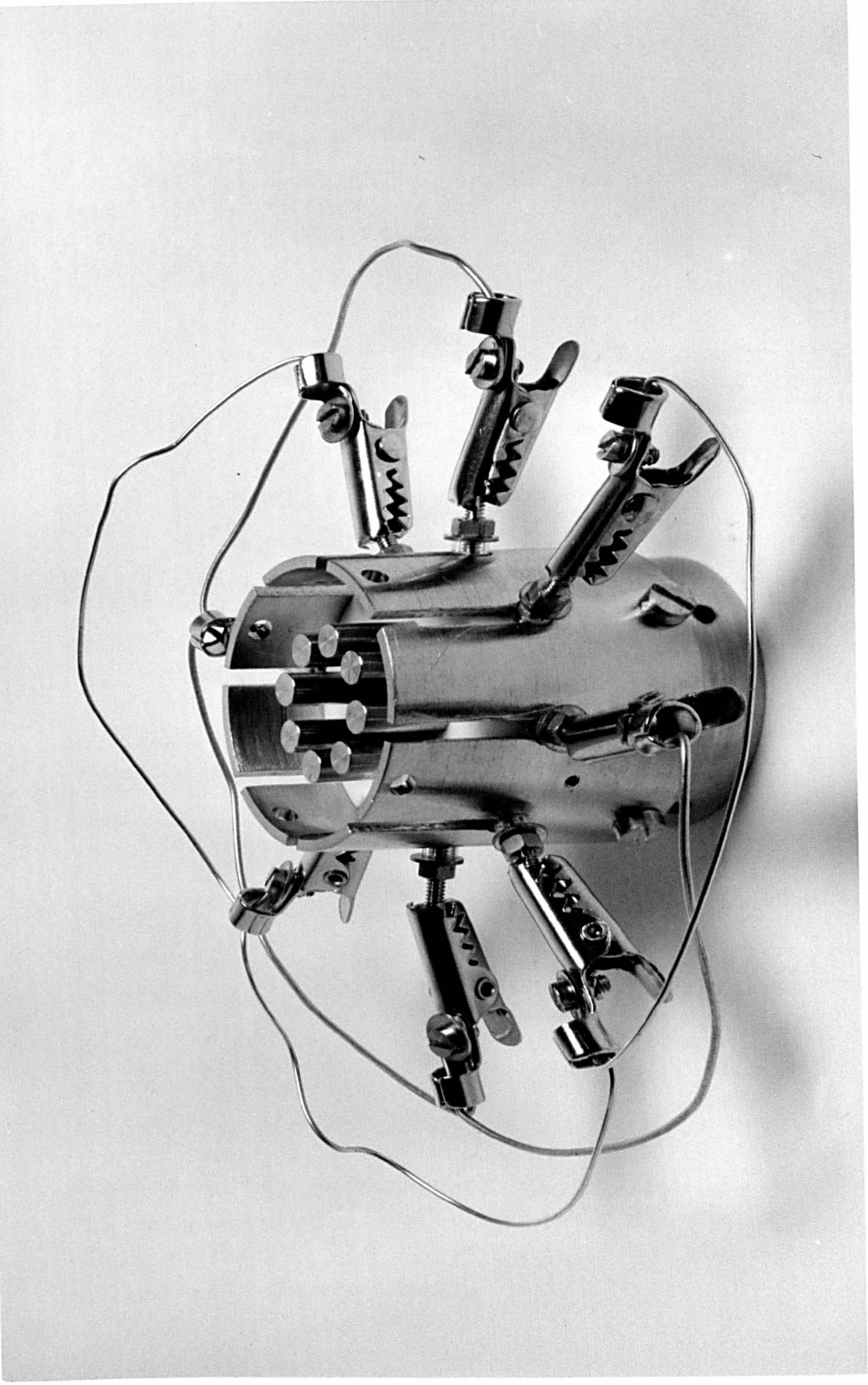

Figure 8. Photograph of octopole with exit plate removed.

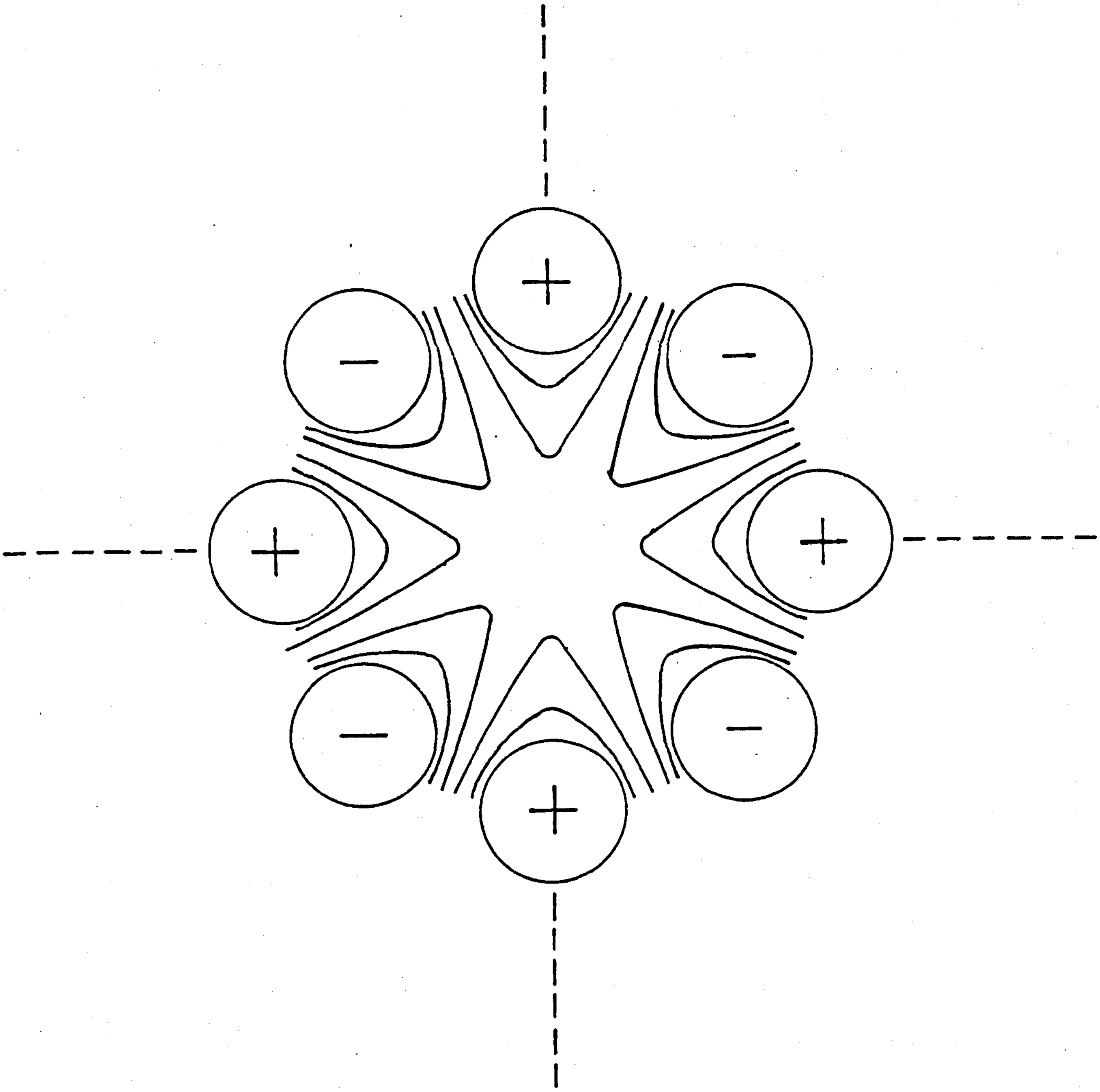

Figure 9. The octopole and its potential field. The rods marked + are interconnected, as are those marked − . The converging planes are marked with broken lines.

converging planes are those containing the axes of opposite pairs of positive rods and the two planes containing the axes of opposite pairs of negative rods are diverging. It would be expected that the effect of such a field on a cross shaped beam would be to make it more circular.

In general the quality of an ion beam is improved by: a) maximising the intensity; b) minimising the angular distribution; and c) minimising the energy distribution. A number of variations of the system shown in figure 5 were tried, in which the octopole was preceded by an entrance aperture and in which a series of three or four element lenses were placed after the octopole. Empirically it was found that the best overall performance could be obtained using just the octopole with an earthed exit plate containing an aperture of 2 mm diameter, and floating the octopole at a negative potential with respect to ground. The size and alignment of the exit aperture was found to be critical. As it is reduced in size the beam becomes better focussed, but the total intensity falls. The octopole axis potential was found to be more critical than the pole to pole potential, indicating that the radially symmetric components of the electric field arising at each end of the octopole from the axis potential play an important role in focussing the beam. These produce a weakly focussing field at the octopole entrance as the ions are accelerated out of the quadrupole, and a strongly focussing lens arises from the axis potential and the exit aperture.

Table 1 shows the characteristics of several typical

TABLE 1. The characteristics of some typical CO^+ beams derived from the ion beam source.

E/ev	ΔE(FWHM)/ev	$\Delta\Theta$(FWHM)/deg	I_{MEAS}/A	I_{SC}/A	I_{MEAS}/I_{SC}
0.62	0.22	3.5	1.3×10^{-10}	3.6×10^{-10}	0.36
3.38	0.24	2.7	5.8×10^{-10}	2.1×10^{-9}	0.28
5.26	0.29	2.1	9.5×10^{-10}	2.4×10^{-9}	0.39
9.39	0.59	1.8	1.3×10^{-9}	3.8×10^{-9}	0.34

ΔE(FWHM) and $\Delta\Theta$(FWHM) are the measured widths of the energy and angular distributions at FWHM. I_{MEAS} is the measured ion current (measured using an electrometer and an ion collector which can be rotated into the ion beam path). I_{SC} is the space charge limited ion current derived as discussed in the text.

CO^+ beams obtained using this ion beam source. High quality ion beams can be obtained at energies substantially below 1 ev.

Although it is possible to obtain intensities substantially in excess of those shown in the table it was found necessary to reduce the intensity to produce a suitably narrow ion beam. This broadening in the angular distribution arises from space charge effects. The maximum ion current that can be transmitted through a cylinder of diameter d and length l at energy E is given by [56]

$$I = 9.1 \times 10^{-7} E^{3/2} m^{-1/2} (d/l)^2$$

Comparison with this limiting value can be made by assuming the beam to be confined to a tube of diameter equal to the image of the beam (FWHM) on the energy analyser. Measured ion currents over a third of this limiting value can be obtained, as shown in table 1, although this equation strictly applies to a homogeneous homocentric beam brought to a virtual focus at l/2.

Figure 10 shows the measured angular distribution of a 3.4 ev CO^+ ion beam in which the full width at half maximum is 2.7° and the width of the baseline is approximately 7°. The angular resolution of the detector, which can be estimated from the detector geometry, is less than 1° in these measurements.

Energy distributions of the ion beam are measured using the retarding potential difference (RPD) method as described in section 3.6.1. Figure 11 shows the measured energy

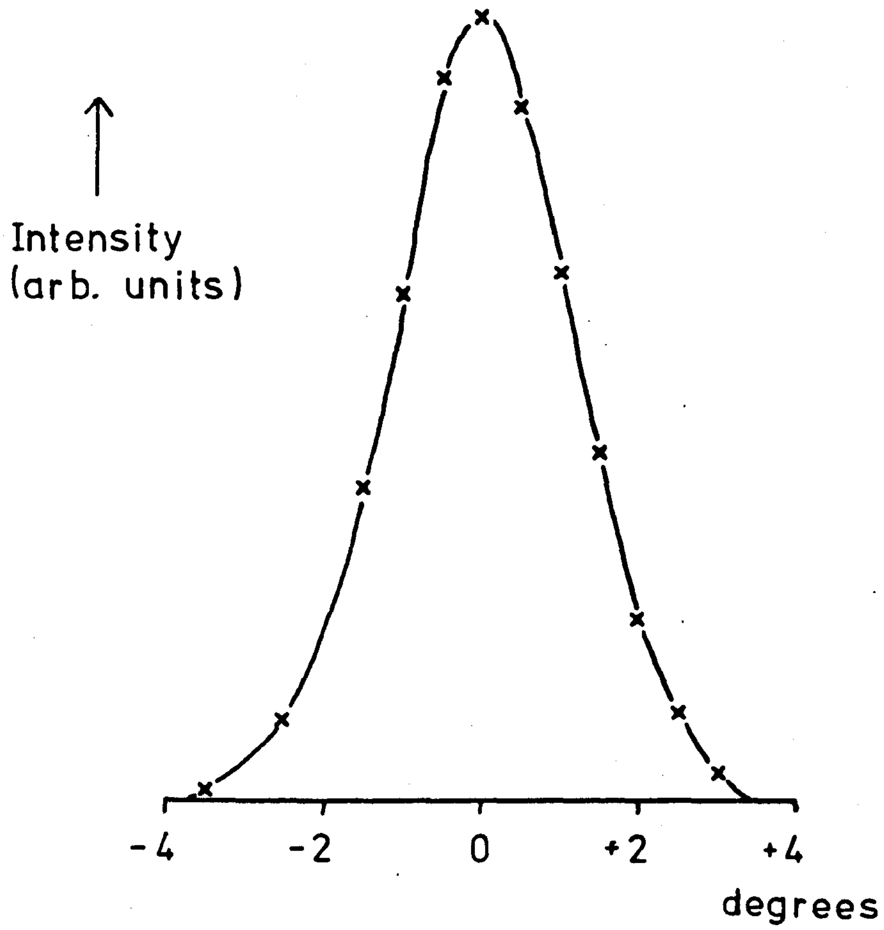

Figure 10. The measured angular distribution of a 3·4 ev CO^+ ion beam ($5{\cdot}8 \times 10^{-10}$ A).

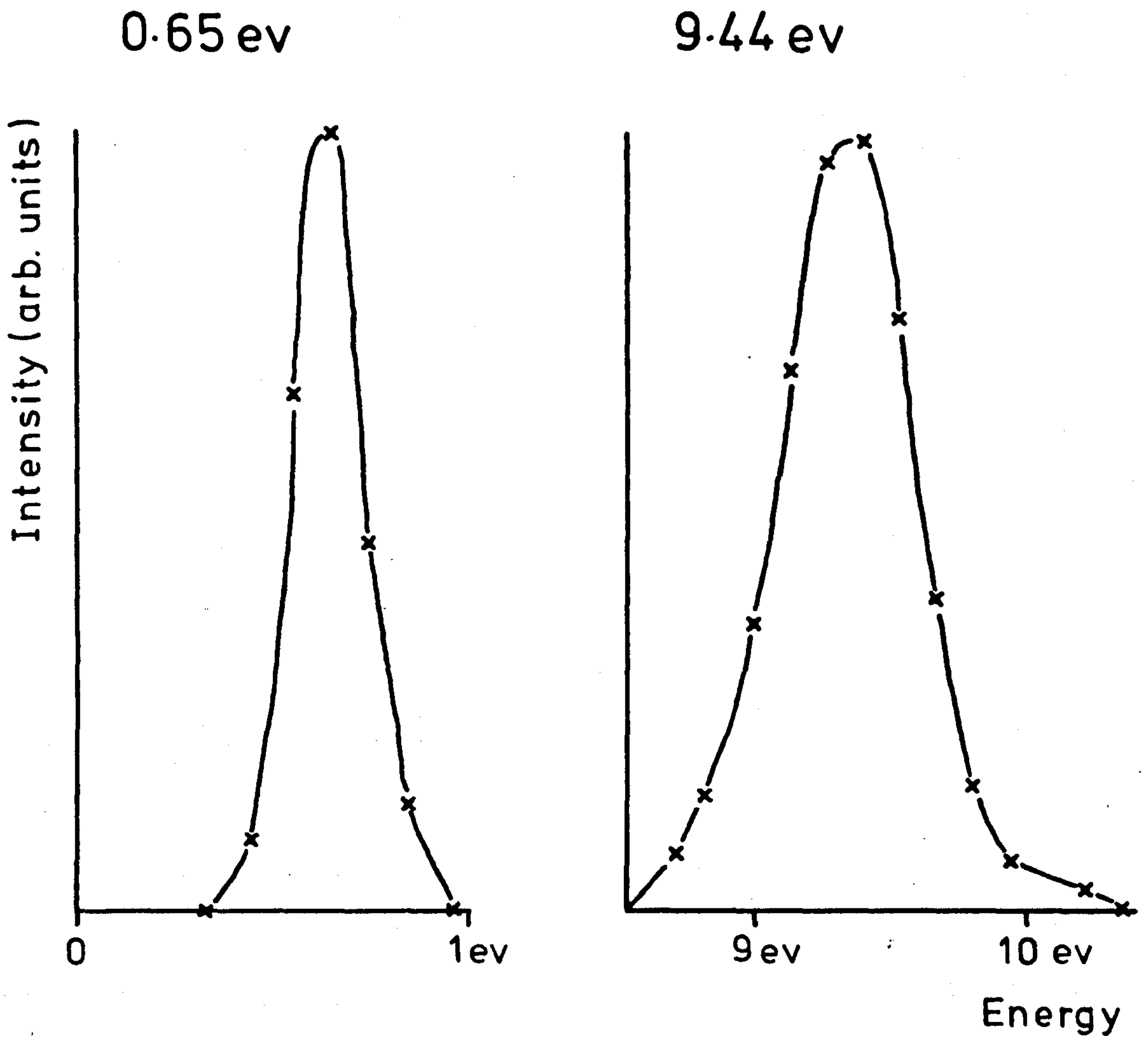

Figure 11. The measured energy distributions of a 0·65 and 9·44 ev CO^+ ion beam.

distribution of a CO^+ ion beam at 0.62 and 9.44 ev. In addition figure 12 shows a plot of ΔE(FWHM), the width of the energy distribution at half maximum, against E, the nominal ion energy, for all beams used to measure contour diagrams over a two month period. A straight line given by $\Delta E(\mathrm{FWHM}) = 0.16 + 0.042\ E$ ev (least squares analysis) can be drawn through the data. The contribution to ΔE proportional to E must be mainly due to energy analyser resolution, while the constant term reflects the actual energy spread of the ion beam (FWHM). This indicates that the total resolution is limited by detector resolution rather than primary ion beam energy distribution except at the lower energies, (less than 4 ev).

The intensities, angular distributions, and energy distributions obtained using this ion beam source are comparable to if not better than those obtained from magnetic sector instruments (cf. Vestal et al [46]). The simplicity of the focussing lens which requires only two focussing voltages, and consequent time saving in obtaining a good quality ion beam, makes this ion beam source particularly attractive for beam formation in the study of ion-molecule reactions.

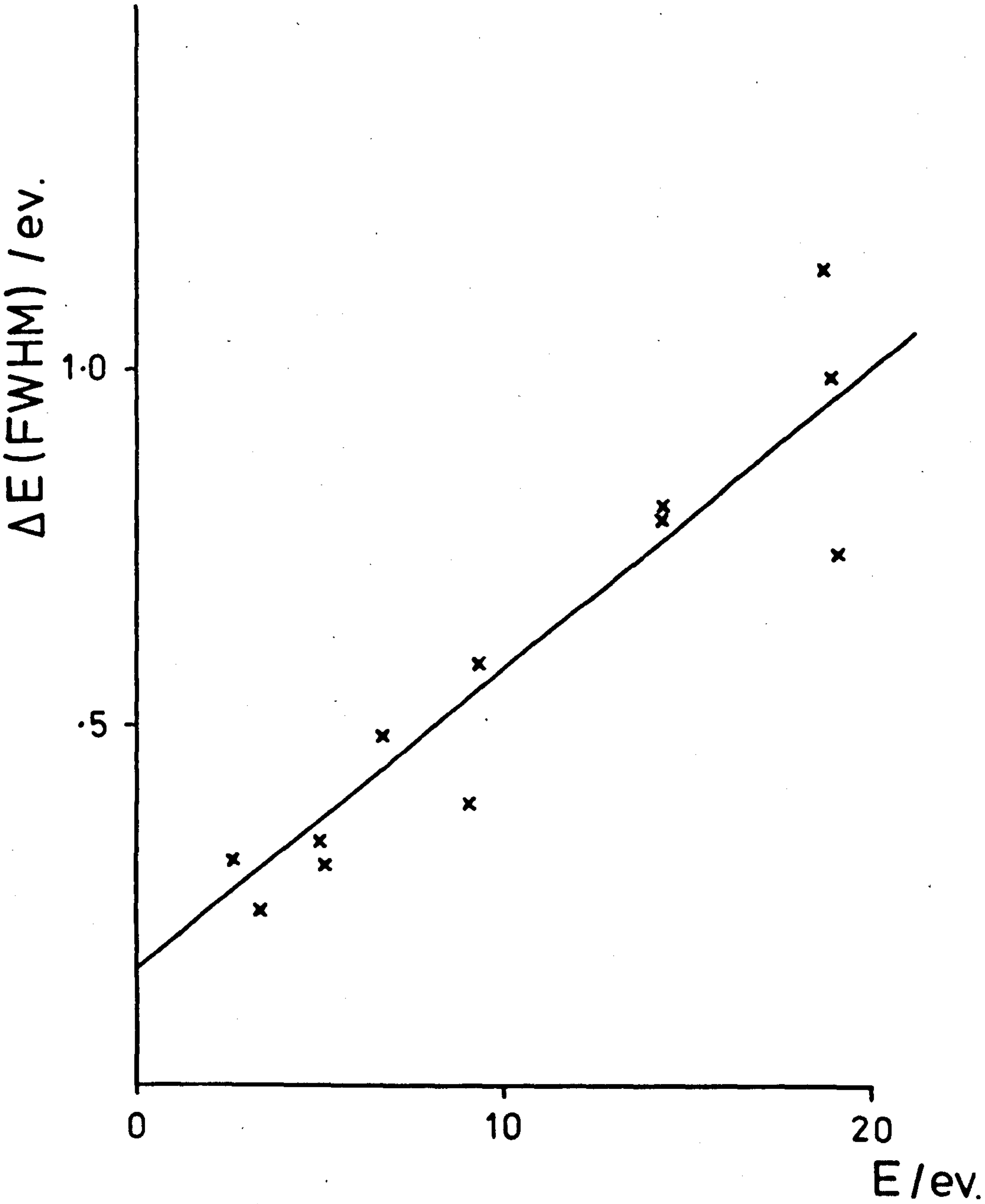

Figure 12. A plot of ΔE(FWHM) against the nominal ion energy, E.

3.4 Neutral beam source.

The neutral beam (figure 5) is derived from a differentially pumped capillary array. A capillary array constructed from 12 0.4 mm diameter stainless steel hypodermic needles packed into a a 1/8" OD stainless steel tube was used in the measurement of the experimental results described here. This has now been replaced by a commercial glass capillary array (Galileo Electro-Optics H25S05M05), which produces a more intense neutral beam, with a narrower angular distribution.

Although a supersonic nozzle source which utilises hydrodynamic flow can provide a more intense narrow beam, pumping requirements are much larger. Here, where the pumping speed is limited by the available space and a fairly broad neutral beam can be tolerated without significantly decreasing the total resolution, the simplicity of the effusive source makes it attractive.

The neutral beam is collimated by a slit (2 mm × 4 mm) in the crossing region shield, 9 mm from the source, so that the maximum angular divergence in the plane of the two beams can be estimated from geometric considerations to be 16°. The pressure in the neutral beam chamber is maintained below 5×10^{-4} torr during operation, to avoid significant attenuation and broadening of the beam.

The velocity distribution in the beam is the normal

Maxwell - Boltzmann distribution multiplied by the velocity. However since the time spent in the reaction zone is inversely proportional to the velocity, the distribution of the interacting particles is Maxwell - Boltzmann [57]. For a capillary array it has been suggested that there is a depletion in slow molecules in the beam [58], attributable to scattering in the channels. For plotting the contour diagrams the most probable velocity, given by $v_{mp} = \sqrt{\frac{2KT}{m}}$ has been used.

3.5 Detector.

The measurement of product ion energy and angular distributions is performed by a detector which consists of a retarding potential difference (RPD) energy analyser, and a quadrupole mass filter. Ions are detected at the end of the QMF using either a channeltron electron multiplier (Mullard B419BL), which is set off axis, and pulse counting , or a Faraday cup and electrometer (Keithley model 602). In the work described here the QMF consisted of an EAI analyser (0.25" diameter rods) and an EAI Quad 250 rf generator which has been modified so that the quadrupole axis potential can be floated with respect to ground. The quadrupole control unit has since been replaced by a Vacuum Generators Q8K rf head and control unit, which has been modified by the manufacturer to drive the large capacitive load of the detector QMF. The detector QMF resolution employed in this work has been the minimum necessary to effectively separate the components in the mass spectrum.

The detector can be rotated in both planes about the crossing region by means of gear trains operated from outside the vacuum system. The extent of the movement is +110° to -15° in the plane of the two beams and ±15° perpendicular to the plane. The angular setting is read outside the vacuum system by means of mechanical counters to an accuracy of 0.1°.

The ion flight path from the crossing region to the detector is shielded from stray magnetic and electric fields by means of a shield (see figures 4 and 5) constructed from non-magnetic stainless steel, 0.004" Telshield, and fine mesh grid.

3.5.1 Energy analyser.

There are several ways of approaching the critical problem of energy analysis. Electrostatic deflection analysers and retarding potential difference (RPD) analysers are the most widely used techniques. The use of time of flight analysis has generally been avoided because of the low duty factor (typically about 5%), although the cross correlation method of time of flight analysis [59] has a significantly higher duty factor (about 50%) and has been used in crossed neutral beam scattering experiments [60].

Deflection analysers have the advantage of yielding energy distributions directly, but are mechanically more difficult to construct, physically larger and have a low transmission efficiency.

The RPD analyser using high transparency grids is a relatively well known instrument. It has the advantage of simplicity and high transmission efficiency, and in addition the analyser can readily be "switched off" to facilitate measurement of angular distributions. However there are a number of inherent problems, in particular large uncertainties in the apparent intensities of low energy components occur in the presence of larger intensities of higher energy components.

Design efforts were thus directed towards producing a simple RPD analyser with a near ideal transmission function. Substantial effort was directed towards this goal, with particular attention being paid to the interface between the QMF and the energy analyser, since this region is most likely to cause discrimination effects, and hence a non-ideal transmission function. To increase the effective entrance aperture of the QMF and minimise energy discrimination effects the QMF is preceded by a Brubaker lens.

The RPD analyser effectively consists of two electrodes with apertures covered in fine mesh grid. The first electrode is at ground potential, and the second carries the retarding potential. The problem is thus to get all ions which are transmitted by the energy analyser at any particular retarding voltage into the quadrupole. Initially a unipotential lens was inserted between the analyser and the Brubaker lens to focus the ions into the QMF. However this was found to be ineffective due to chromatic aberation (since the ions emerge from the analyser with a large range of energies) and also because the angular acceptance of the quadrupole is limited. To overcome this problem the unipotential lens was replaced by a single electrode with an aperture covered with fine mesh grid, which was maintained at quadrupole axis potential (typically -8 to -10 volts). Thus after leaving the energy analyser the ions are accelerated and enter the QMF as a near parallel beam. In addition this electrode shields the energy analyser from the rf fields in the quadupole. Rf pick-up is capacitively filtered off the energy analyser electrodes, with the maximum remaining pick-up being less than 20 mv peak to peak.

Figure 13 shows a diagram of the energy analyser. The apertures in the first and second electrodes are 4 mm in diameter. All electrodes are coated in a single layer of colloidal graphite (Aquadag), to ensure a uniform surface potential and minimise build-up of surface charge which could deflect very low energy ions. The fine mesh grids are spot welded on to the electrodes, care being taken to ensure the grids are flat. The grid specifications are : 100 wires per inch (wpi), stainless steel, 81% transparent on the first and third electrodes; and 180 wpi, 73% transparent, tungsten on the second electrode. The electrodes are separated by precision cut glass spacers 1 mm thick.

The separation between the electrodes is critical because conflicting requirements are posed by the effects of field penetration and space charge. As will be discussed below field penetration through the grid on the second electrode limits the resolution of the energy analyser and a large separation between the electrodes is thus required for maximum resolution. However space charge effects - space charge expansion of the beam as it is retarded and virtual cathode formation, due to the build up of space charge in front of the second electrode if the current is in excess of the Child - Langmuir value [61,62], both require that the

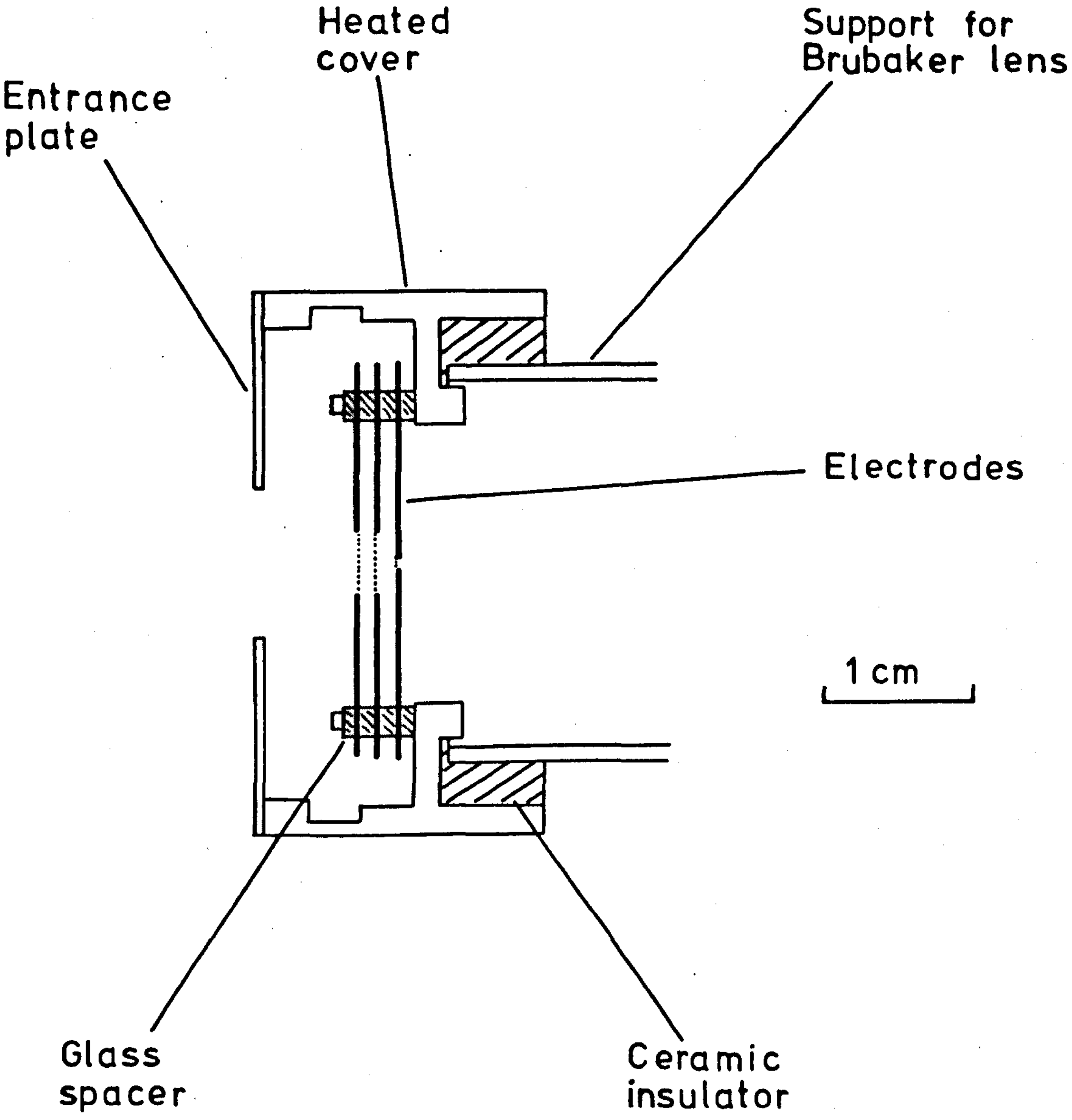

Figure 13. Diagram of the energy analyser

distance between the plates be small. A complete analysis of these effects is extremely complicated. Virtual cathode formation might be expected to be a source of error in the measurement of the primary ion beam energy, and indeed small experimental distortions have been experimentally detected, although this introduces negligible error as will be seen from the data to be presented an Ar^+ + Ar collisions in section 3.8.

The size of the aperture in the third electrode is critical, since this determines measured ion intensity, mass filter resolution, angular resolution, and in addition it was found that if the size of this aperture was substantially increased the quality of the measured energy distributions declined sharply. Presumably this is due to discrimination effects as ions enter the QMF substantially off axis. Empirically it was found that the optimum size for this aperature was 1mm diameter.

A surface charging problem was encountered when measurements were made in the primary ion beam but this was overcome by heating the energy analyser to approximately 150°C by means of Nichrome heating wire wrapped non-inductively around the energy analyser cover. The temperature of the energy analyser is monitored by means of a thermistor.

The distance from the crossing point to the third electrode is 69 mm, and the angular resolution (which is defined by the aperture in the third electrode) can be estimated from geometric considerations to be 3° assuming the volume of the crossing region is $3 \times 3 \times 3$ mm .

RPD analysers utilising high transparency grids are not amenable to a detailed theoretical treatment due to field irregularities near the grid wires. However a simplified treatment of the main factors which limit the energy resolution can be given:

1) Since only momentum normal to the equipotential lines is analysed this imposes a limit on the obtainable resolution given by $\Delta E/E = \sin \theta$ [63], where θ is the deviation of the most inclined trajectory. In a crossed beam apparatus employing angular resolution this problem is small ($\Delta E/E \simeq$ 0.3%).

2) Each aperture in the grid of the first electrode approximates to a divergent lens of focal length $1/f = V_2 - V_1/4\ E$ where V_1 and V_2 are the potentials on the electrodes, and E is the ion energy. This leads to a limiting resolution $\Delta E/E = r^2/16\ d^2$ [63], where r is the aperture radius and d is the separation between the electrodes. This has a minor effect on the total resolution ($\Delta E/E \simeq 0.01\%$).

3) Deviation of the potential between the grid wires from the imposed retarding potential results from field penetration. An estimate of the potential at the saddle point can be obtained from $\Delta E/E = r/2\ d$, which can be simply derived by considering the electric field arising when a circular aperture is inserted between two electrodes at the same potential [64]. This expression under-estimates the field penetration effects, since it neglects the small potential on the third electrode. Field penetration is the

most important factor in limiting the resolution ($\Delta E/E \simeq 3.8\%$). Previous attempts to calculate the deviation have employed Spangenberg's treatment of the plane triode [62,65] to provide an expression. The application of this expression has questionable validity in this situation, and also over-estimates the deviation since the theory applies to parallel wires rather than a grid.

Summing these contributions leads to a total energy resolution of approximately 0.041 E. Figure 12 shows a plot of ΔE(FWHM) against E for the primary ion beam, this is a straight line given by $\Delta E(\text{FWHM}) = 0.16 + 0.042\ E$ ev. Since the contribution to ΔE proportional to E must be mainly due to energy analyser resolution this seems a reasonable analysis, though the close agreement may be fortuitous.

3.6 Data aquisition.

Product ion intensity contour diagrams are derived from measurements of the angular distribution of the product ions in the plane of the two beams and their energy distributions at several strategic angles.

3.6.1 Measurement of the primary ion beam energy distribution.

This is accomplished using the data acquisition system shown in figure 14. The energy distributions are recorded in a multichannel analyser (Ernest Ireland MCA500), operated in the multiscaling mode, using 256 channel resolution. Ions are detected using a Faraday cup (biased at -10 volts), and electrometer. The analogue output from the electrometer is converted to digital form prior to entering the multichannel analyser by a high input impedance differential amplifier and voltage to frequency converter (designed and built in this laboratory, see appendix at the end of this section for circuit details). The retarding ramp is derived from the multichannel analyser dwell time pulses (produced internally), which are converted to a staircase ramp by a digital to analogue converter (see appendix), and amplified using an inverting buffer amplifier (Electrosystems). The starting voltage and range are preset. The upper and lower levels of the ramp are monitored by level detectors and can be measured to an accuracy of better than 1% by a digital voltmeter (Keithley model 178DMM).

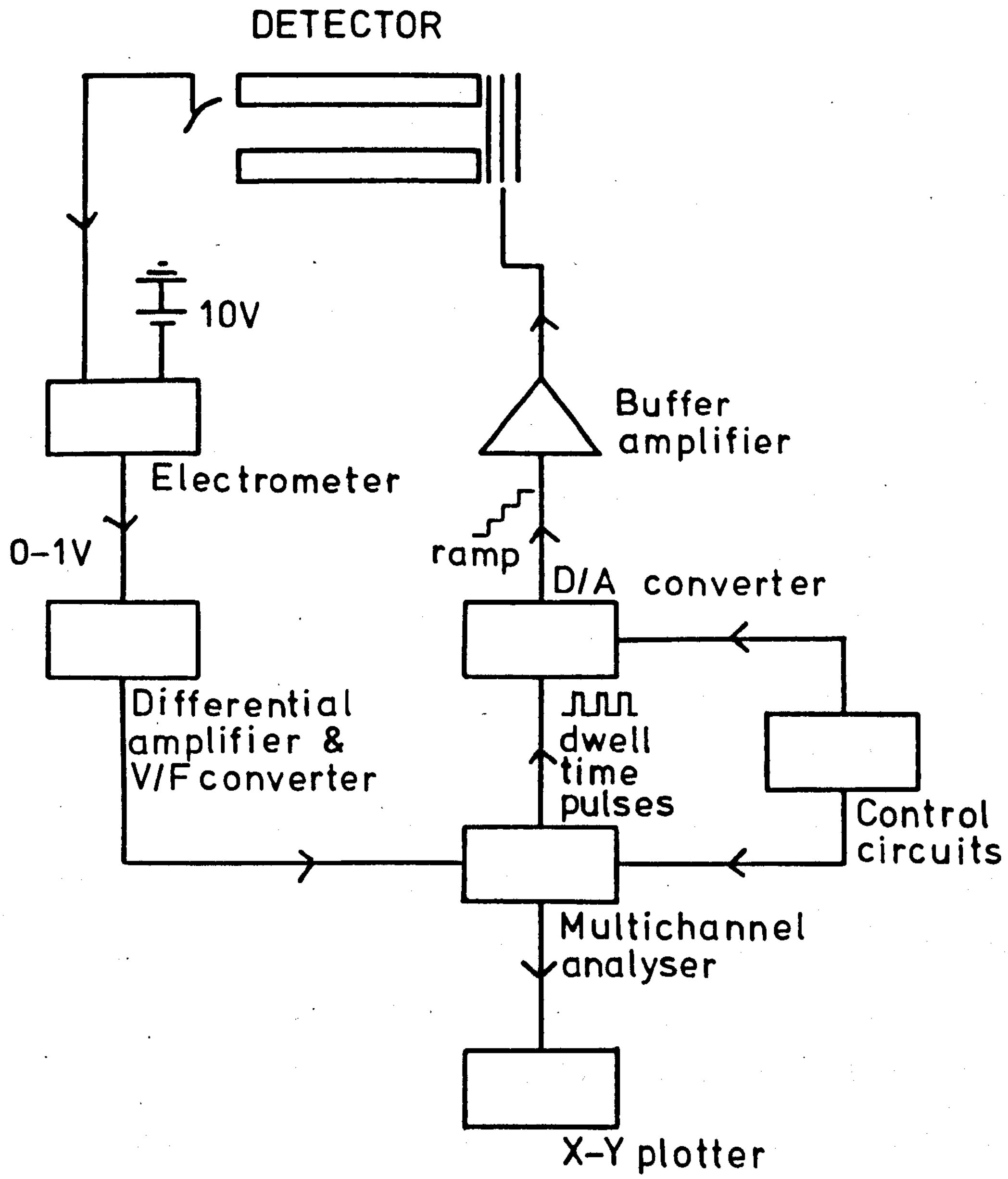

Figure 14. Diagram of data acquisition system used for measurement of primary ion beam energy distribution.

3.6.2 Measurement of product ion angular and energy distributions.

The digital data acquisition system, shown in figure 15, used for measurement of product ion angular and energy distributions accomplishes both signal averaging and automatic background subtraction.

Single ion pulses from the electron multiplier are amplified by a NIM (nuclear instrumentation module) charge sensitive preamplifier and NIM amplifier, and then fed into a NIM ratemeter and either the multichannel analyser, (which has been modified by the manufacturer for remote control of data add-subtract) for energy distribution measurements, or into the up-down counter, for angular distribution measurements. The NIMs initially used in this work were Nuclear Enterprises preamplifier NE4 607, amplifier NE4 603, and ratemeter NE4 607. These were subsequently replaced by Ortec preamplifier 142IH, amplifier 571, and ratemeter 449. Coincidence losses are negligible up to 10000 cps, although the multichannel analyser does in fact provide live-time correction.

The neutral beam is modulated at a frequency of 10-30 Hz by a segmented disk driven through two nylon gears by a synchronous motor (Impex Electrical, 9904 11106). The power supplies to the motor are derived from a power amplifier (Electrosystems) and variable frequency oscillator (see appendix). The motor was degreased and glass PTFE impregnated bearings installed, and it is totally enclosed

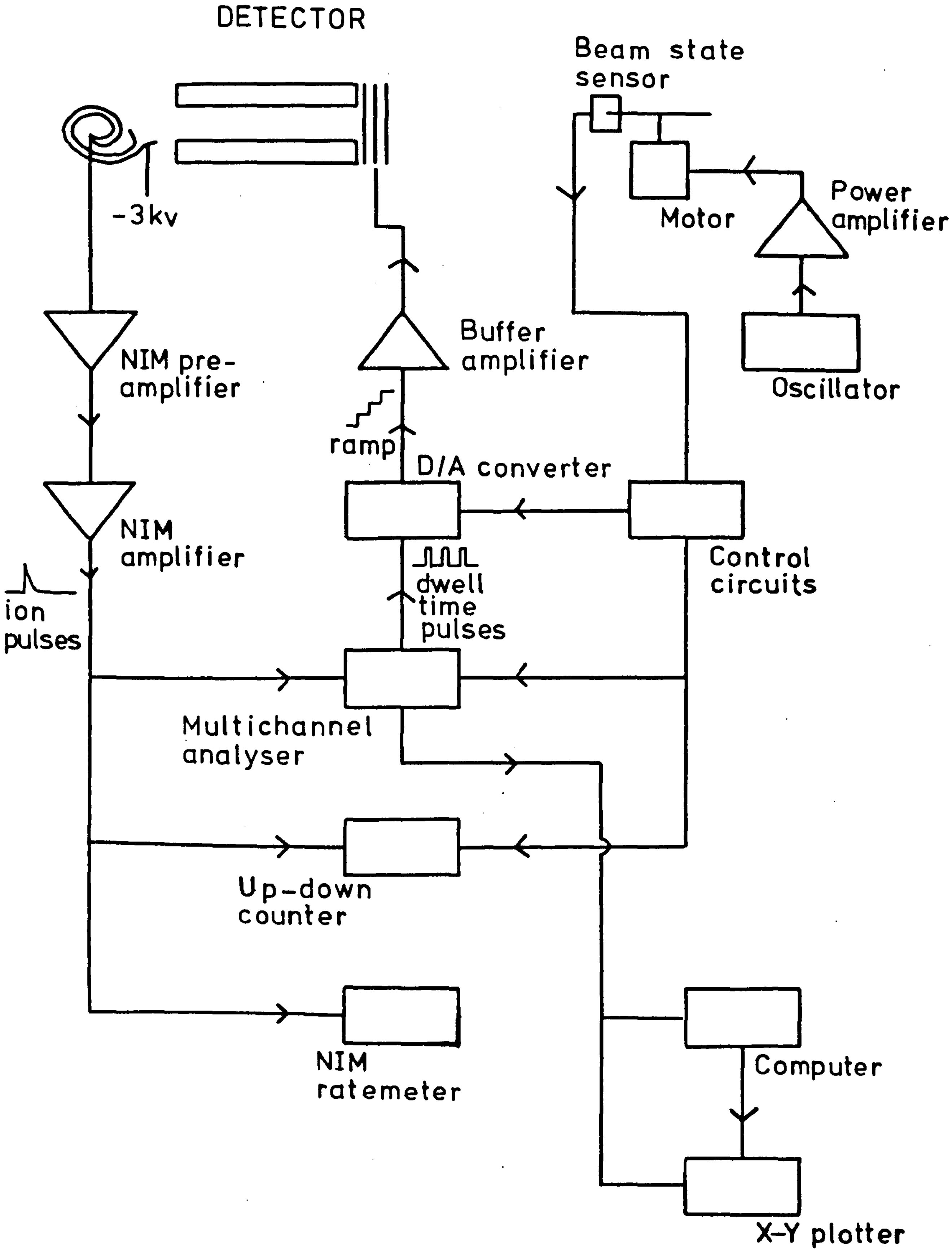

Figure 15. Diagram of digital data acquisition system for product ion measurements.

in a mumetal box to avoid stray magnetic fields. Experiments in which the neutral beam was modulated and the product ion arrival time distribution recorded in the multichannel analyser, with the energy analyser switched off, indicated that there is no detectable background modulation.

Changes in the neutral beam state are detected by a light emitting diode and photo-transistor assembly (Texas Instruments TIL138). The output from this unit is amplified and fed to 74 series TTL control circuits (see appendix), which synchronises pulse counting and retarding ramp with neutral beam modulation. Figures 16 and 17 show the time sequence of events in the measurement of energy and angular distributions.

In the measurement of energy distributions the retarding ramp is produced as described in section 3.6.1. Each time a change in the neutral beam state is sensed a measurement of the energy spectrum is initiated after a preset delay, by a trigger pulse to the multichannel analyser. When the multichannel analyser reaches address 256 it stops counting and waits for the next start command. Thus by suitable choice of delay and dwell times, measurement while the neutral beam is changing state is avoided. With this system a complete energy spectrum is recorded each half cycle of the beam chopper. When the neutral beam is on the spectrum is added into memory, when it is off it is subtracted. A display of the analyser memory on a VDU allows monitoring of the data accumulation until the desired statistics are obtained.

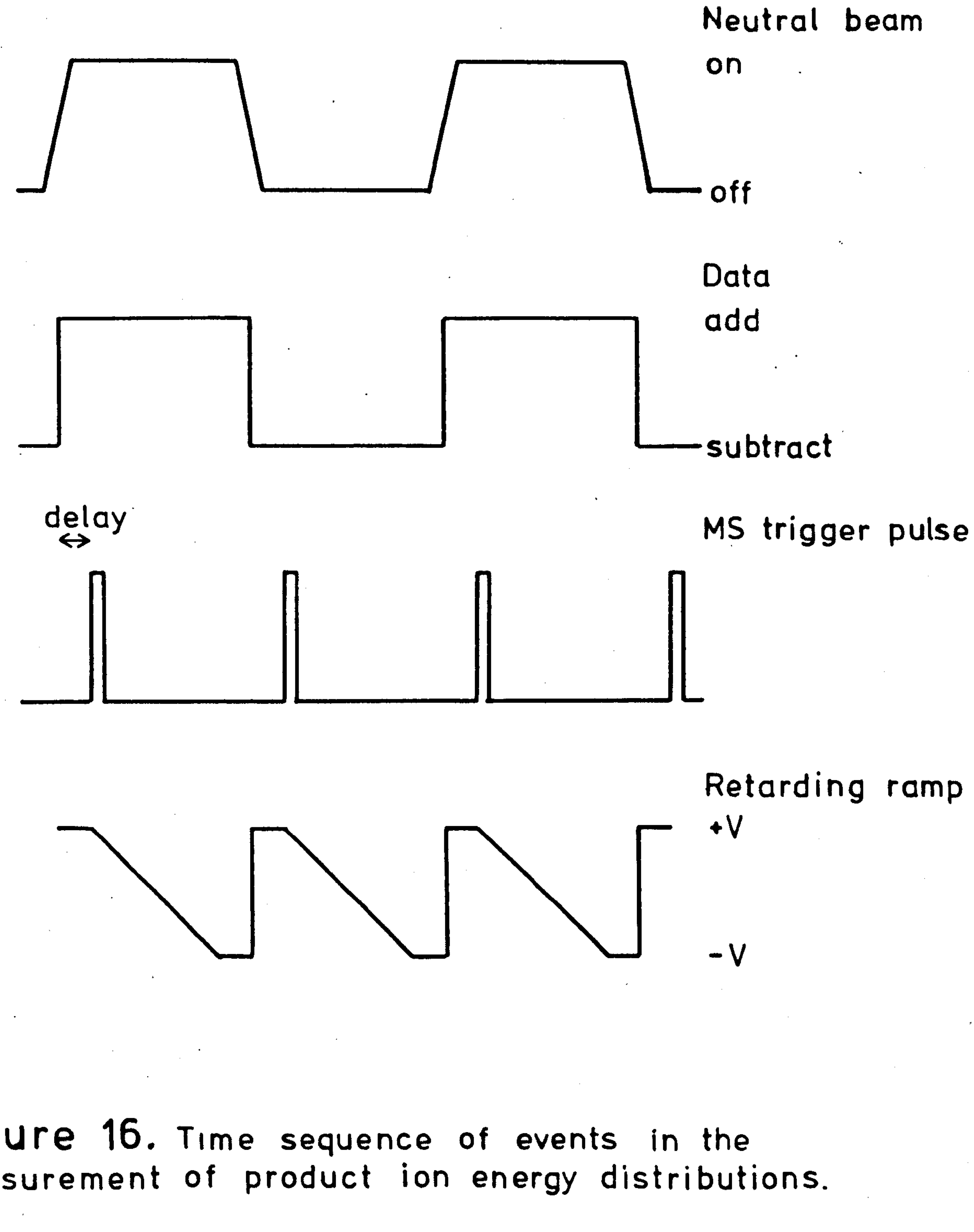

Figure 16. Time sequence of events in the measurement of product ion energy distributions.

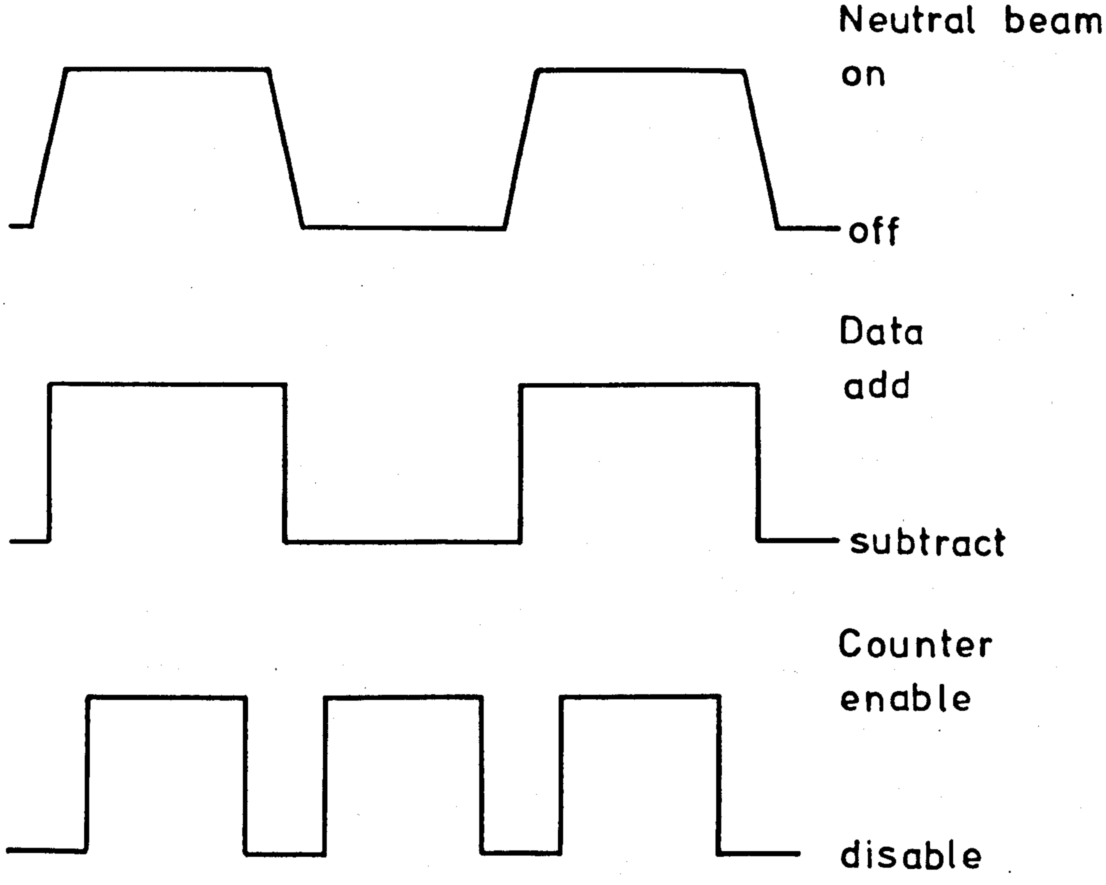

Figure 17. Time sequence of events in the measurement of product ion angular distributions

For measurement of the angular distributions the retarding potential is set to zero, and hence the intensity measured at any particular angle can be unambiguously related to the integral over the energy distribution at that angle. The angular distributions are measured using an up-down counter (see appendix) with counts being added when the neutral beam is on and subtracted when it is off. Figure 17 shows the time sequence of events in the measurement of the angular distributions. When a change in state of the neutral beam is sensed the up-down counter is enabled after a preset delay, and counts for a preset time. Thus by selecting suitable delay and enable times, measurement during changes in beam state can be avoided. After initiation counting continues for a preset time (1-3 min), and then the ion counts are displayed on an LED display.

Appendix to section 3.6.

Circuit diagrams for components of data acquisition system designed and built in this laboratory.

1) Ramp generator.

2) Up-down counter.

3) Data acquisition control ciruits.

4) Oscillator.

5) Voltage to frequency converter.

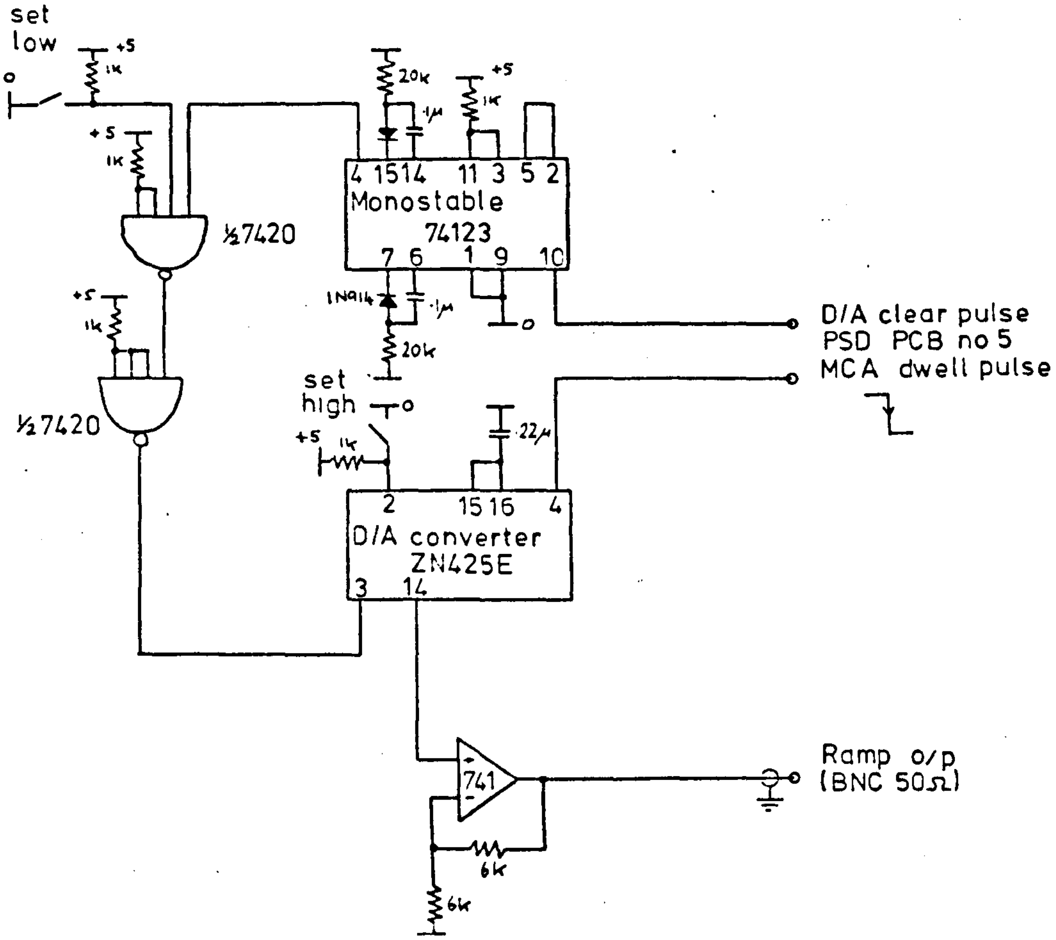

Figure 18. Circuit diagram of ramp generator.

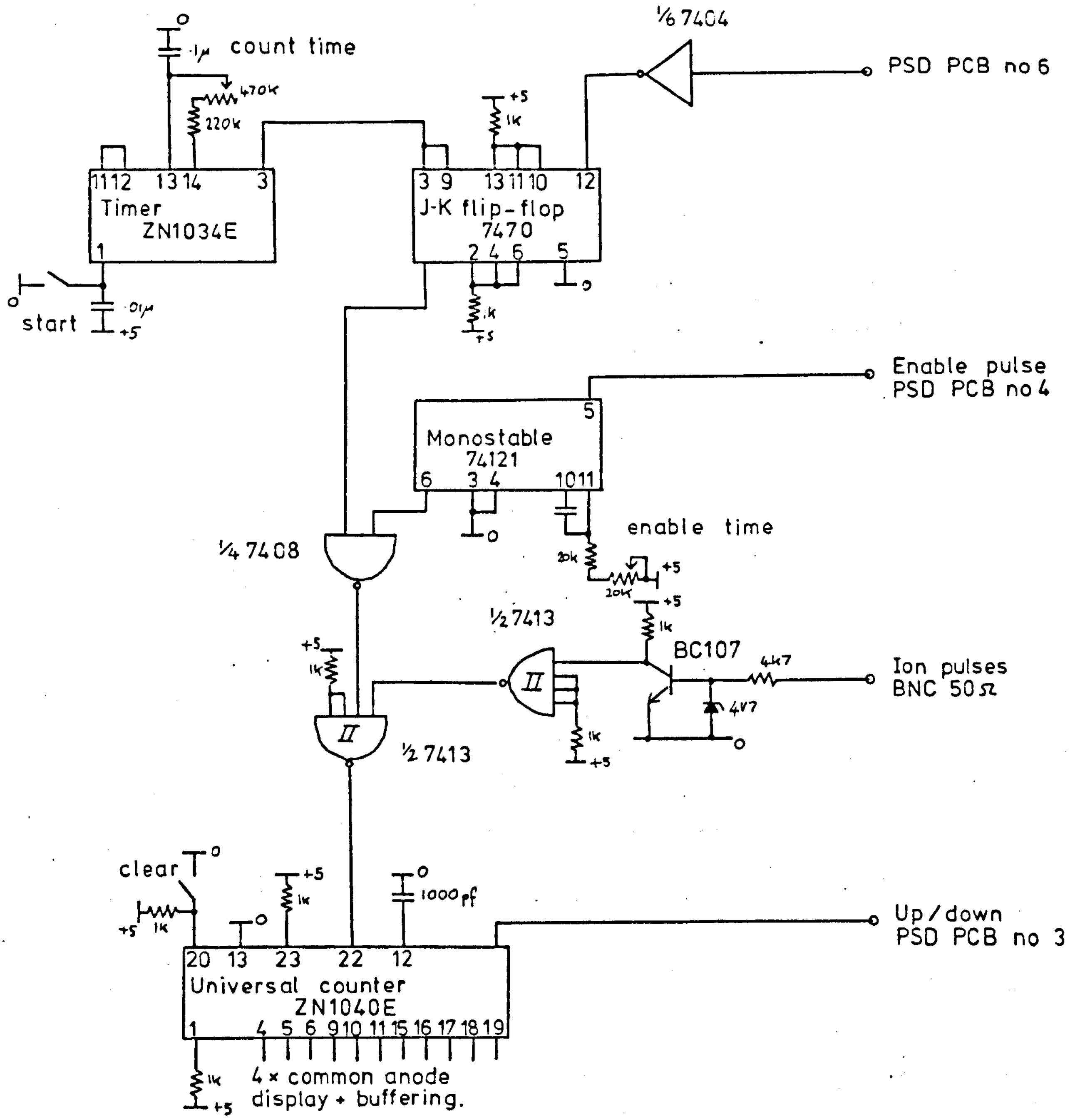

Figure 19. Circuit diagram of up-down counter.

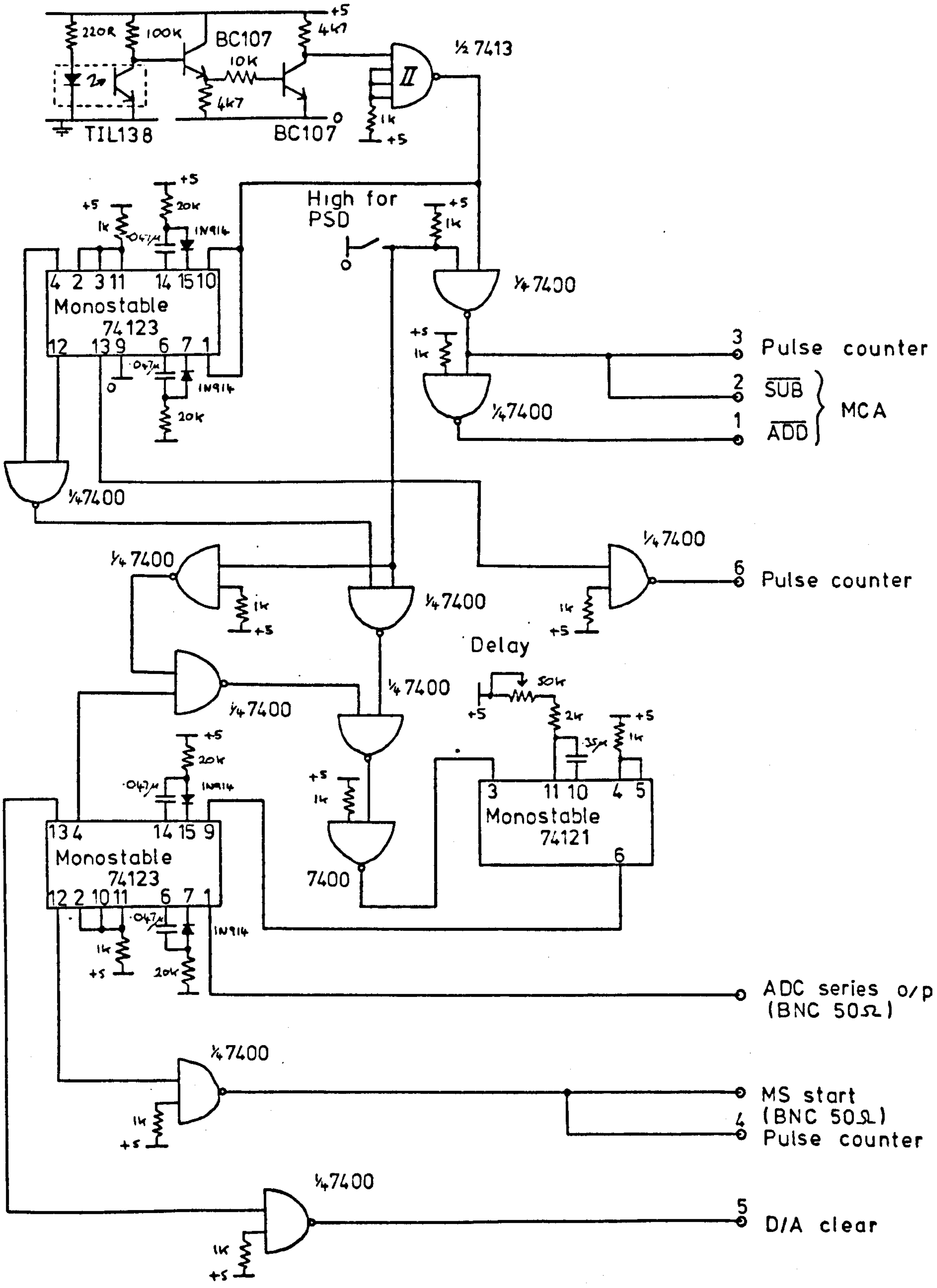

Figure 20. Circuit diagram of data acquisition control circuits.

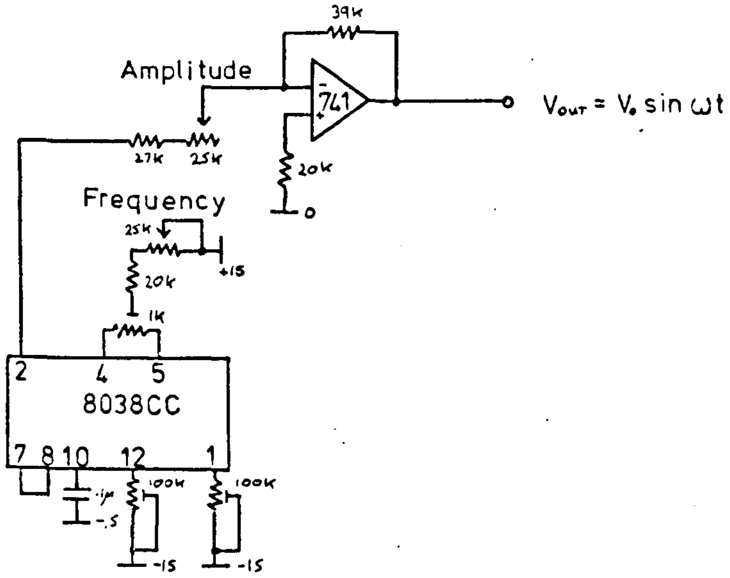

Figure 21. Circuit diagram of oscillator.

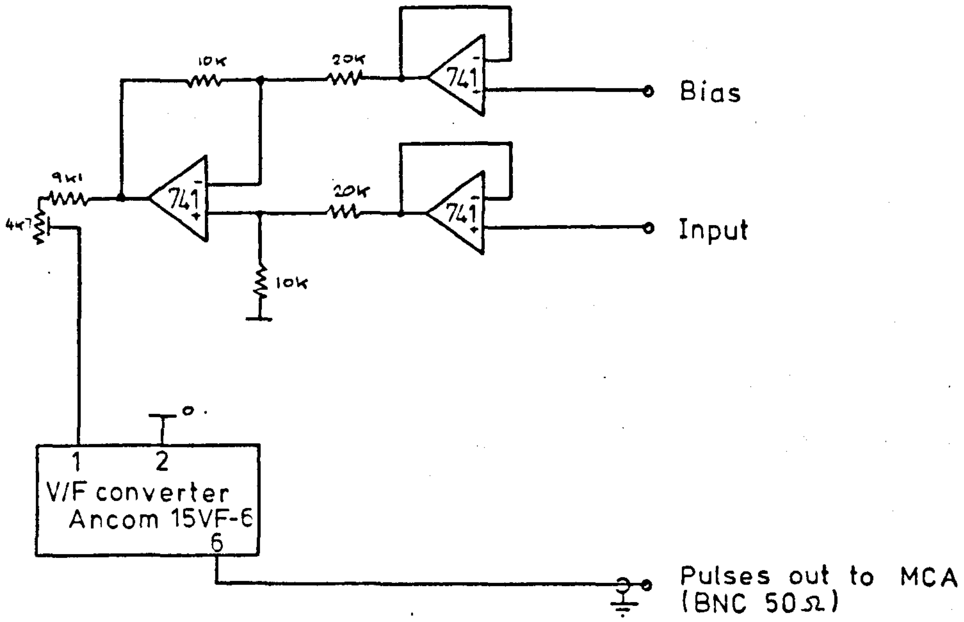

Figure 22. Circuit diagram of V/F converter.

3.7 Treatment of experimental data

Angular distribution measurements, which are repeated at least three times, are made at intervals of 5° or less if the distribution is changing rapidly. Average intensities at each angle are then obtained, normalised and plotted. Figure 23 shows an example of a measured angular distribution.

Accurate absolute normalisation requires knowledge of ion beam and neutral beam intensity and spatial distribution, and absolute detector efficiency and acceptance function. However it was thought that rather than arbitrarily normalising the data to a maximum of 100 some valuable information might be obtained by attempting an approximate relative normalisation. Detector transmision efficiency is assumed constant, ie a constant QMF resolution is used, and the detector acceptance function is assumed to be ideal. Since it is a non-trivial problem to measure neutral beam intensity and angular distribution, a "standard" neutral beam is used in these measurements, which is obtained by operating with a constant pressure in the neutral beam chamber. In addition ion beams with approximately the same angular spreads are used. Thus normalisation only requires knowledge of the ion beam intensity which can be readily measured. This procedure was found adequate for the work on $CO^+ + O_2$ where low detector QMF resolution was employed. For the work on CO^+ + NO higher detector QMF resolution was used, and it was found difficult to maintain a constant detector transmission efficiency. To

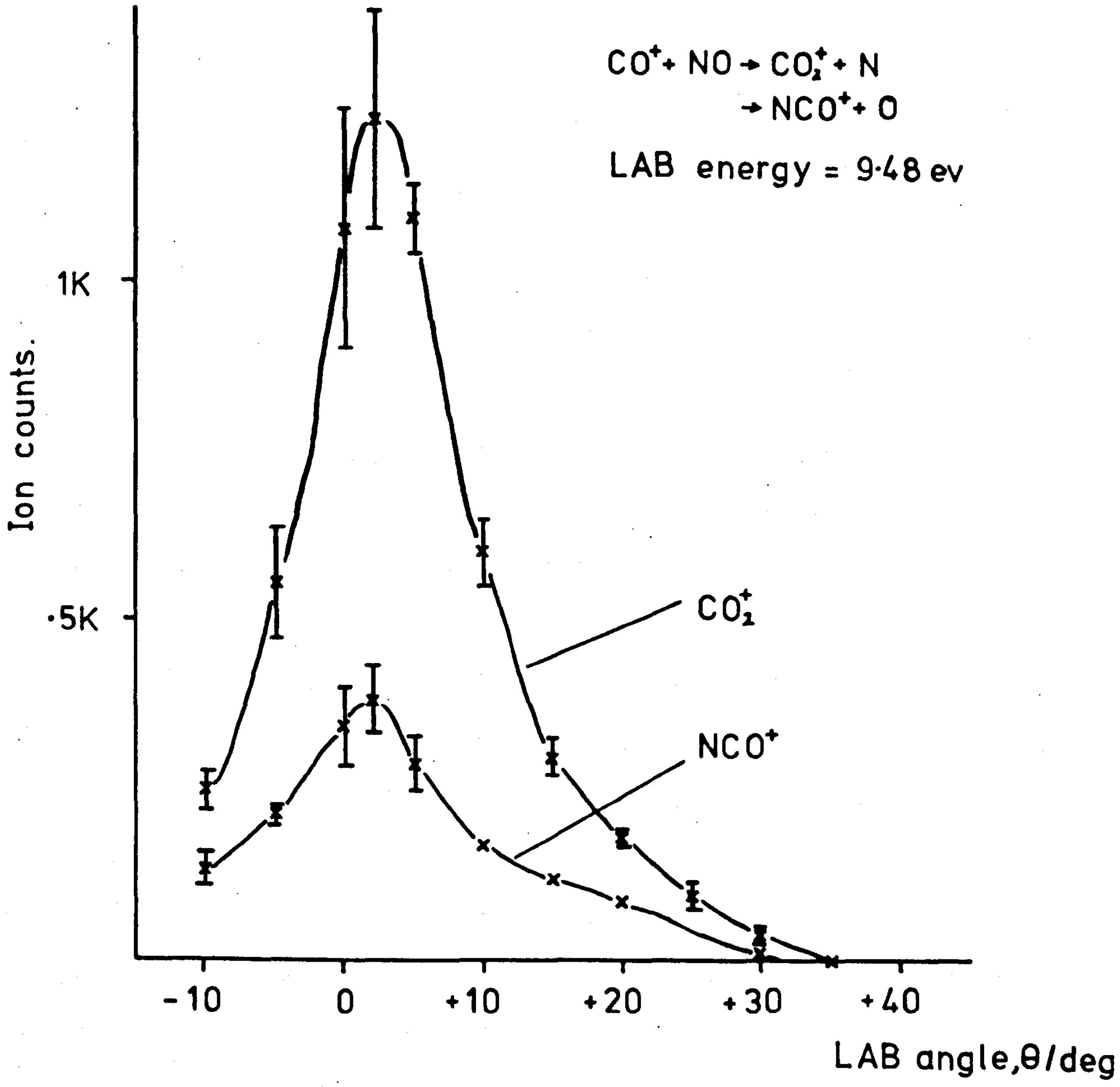

Figure 23. An example of a measured product ion angular distribution. Error bars represent 2 × standard deviation.

overcome this problem, angular distribution measurements were referenced to a standard distribution.

In the majority of the work described here energy distributions accumulated in the multichannel analyser were plotted out on an X-Y recorder (Bryans 29000), manually smoothed and numerically differentiated. Figure 24 shows an example of an integral energy spectrum taken directly from the x-y recorder output. Product energy distributions were then normalised to the angular distribution measurements and transformed to a cartesian velocity space, and plotted on the contour diagram as described in section 2.2

The availability of the new generation of microprocessor based minicomputers on the consumer market provides a new powerful computer for use in data acquisition and analysis in the laboratory at a very low cost. In the final stages of this work a minicomputer (Commodore "PET" 3032) was interfaced with the instrument. The Commodore "PET", which is built around the 8 bit MOS 6502 microprocessor [66], comes with a keyboard, cassette storage, VDU, upto 32K of RAM, and a resident BASIC interpreter. Interfacing is accomplished using the "PET" peripheral interface port (MOS VIA 6522 [67]) which provides 8 bit data and 2 control lines. The computer has been interfaced with the multichannel analyser and X-Y plotter. Figure 25 shows the circuit diagram of the X-Y plotter interface designed and built in this laboratory. To date programs have been written which input data from the multichannel analyser, smooth the energy distributions, and

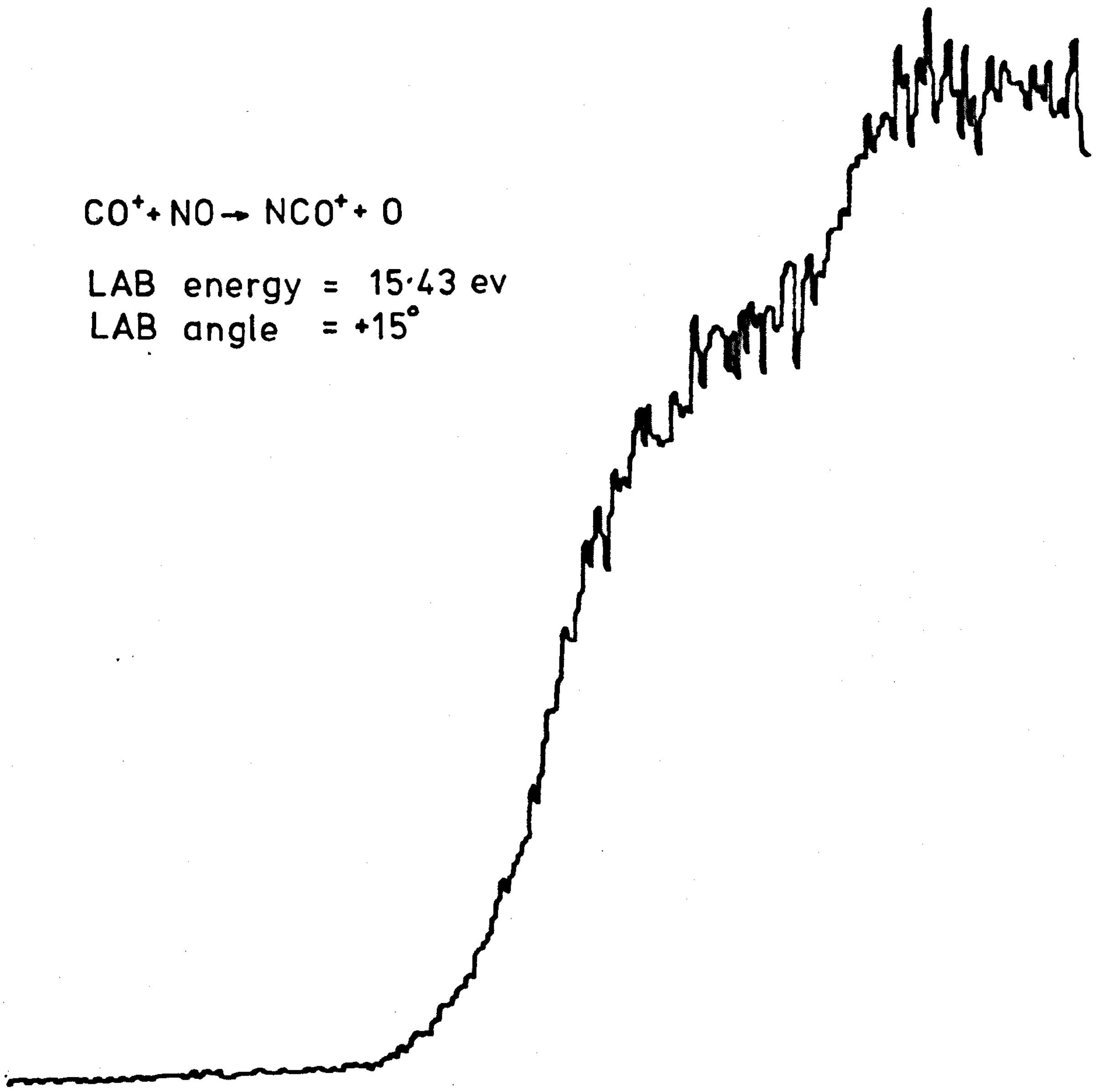

Figure 24. An example of an integral energy spectrum traced directly from the X-Y plotter output.

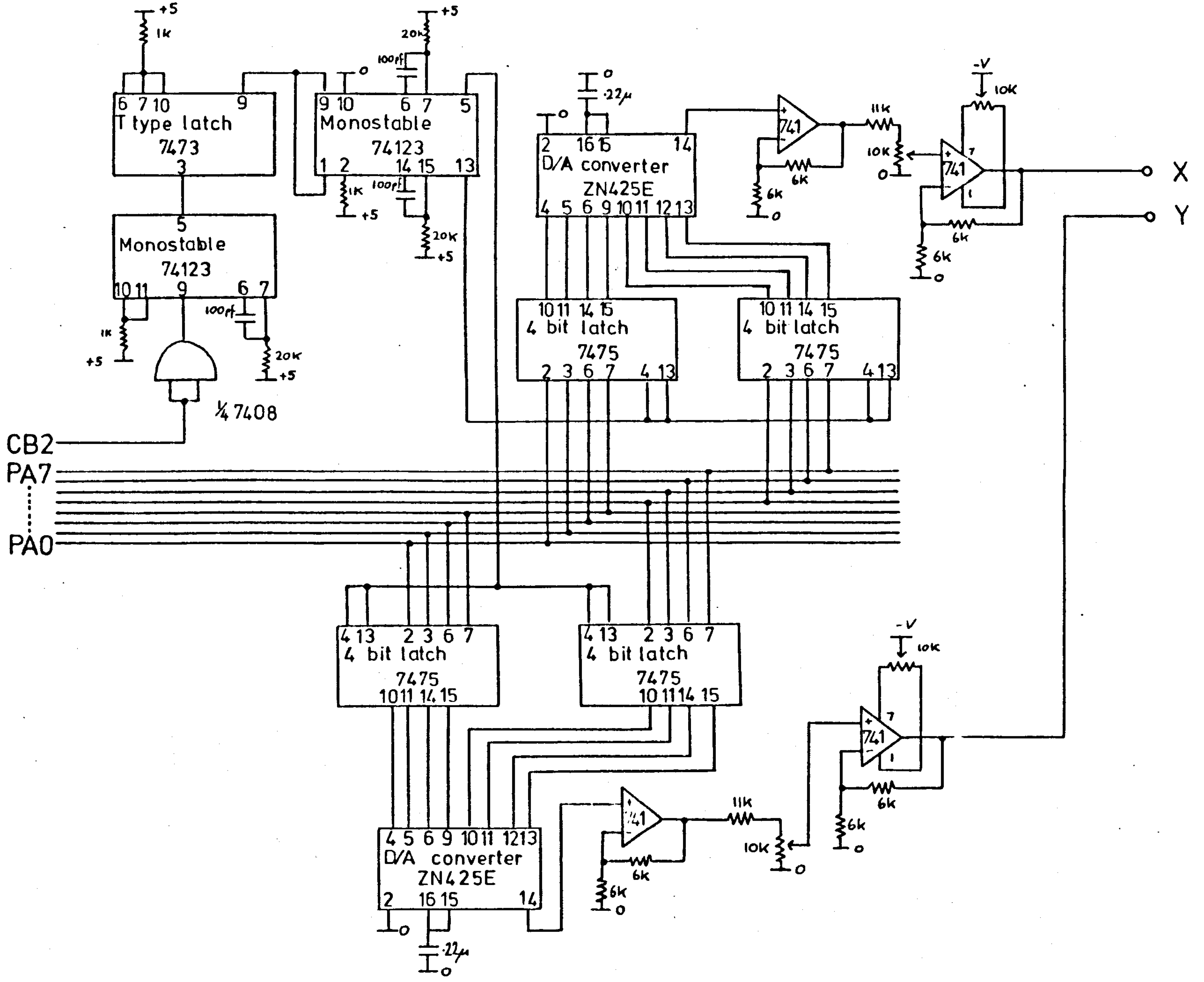

Figure 25. Circuit diagram of the X-Y plotter interface.

plot them on the X-Y plotter.

In the treatment of the experimental results the fact that the experimental velocity vectors are only determined to within an accuracy determined by experimental resolutions has been neglected. The uncertainties in the measured relative energies and centre of mass scattering angle due to primary beam uncertainties, and detector resolution vary in a complex manner. Vestal [39] has given this problem a standard propagation of errors treatment to give expressions which can be used to ascertain whether structure seen in experimental results can be reasonably considered as real features or if they must be ascribed to noise.

The experimental uncertainties must also be taken into account when transforming between coordinate systems. Most of the difficulty occurs near the origin of the coordinate space. Close to the laboratory origin, if the velocity is comparable to the precision with which it was measured, unacceptable distortion will be introduced into the data. For this reason data within 0.1 ev of the LAB origin has not been included in the contour diagrams.

3.8 Performance

The overall performance of the crossed beam apparatus has been assessed by measuring the angular and energy distributions for elastic scattering and charge exchange in Ar^+ + Ar collisions. This provides a very useful test, as the energy of the product ion varies in a predictable way with angle, enabling one to calibrate the energy scale, and assess the performance of the detector with low velocity ions.

The angular distributions have been transformed to CM coordinates by multiplying by the jacobian $g/4.v^2$ [68], where g is the relative collision velocity, and v is the velocity of the scattered ion in the laboratory. The relative differential cross section is shown in figure 26. Oscillations in the differential cross section are apparent, arising from a number of overlapping interference patterns. These interference patterns include the rainbow pattern due to an attractive ungerade potential, nuclear symmetry oscillations on both the gerade and ungerade potentials, and the oscillations due to gerade-ungerade (g-u) interference.

Good agreement was found with the measurements of Vestal et al [69] in both the position and size of the structure in the differential cross section except at wide angles where the collection efficiency of these near thermal velocity ions is low.

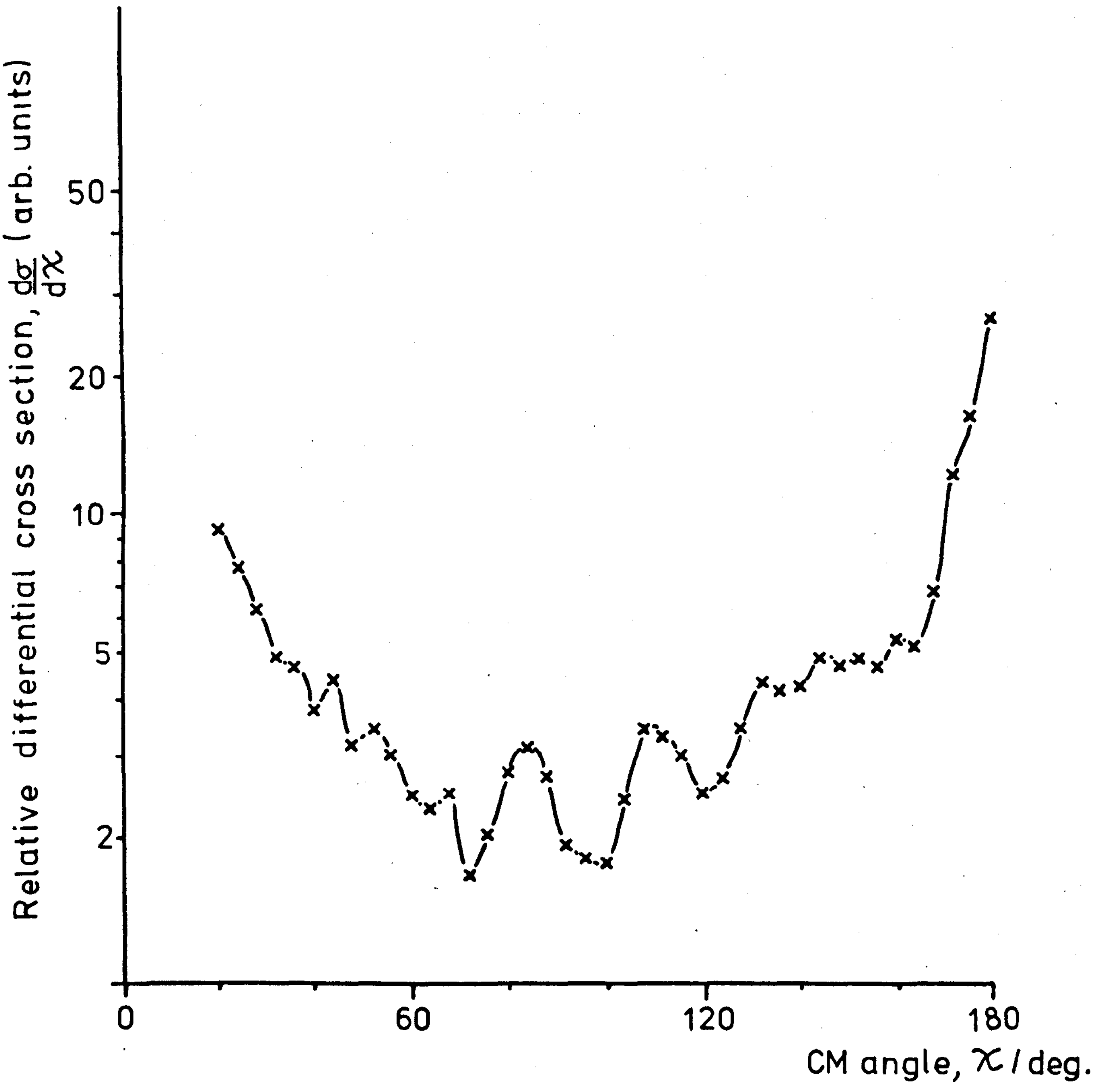

Figure 26. Relative differential cross section for elastic scattering and charge exchange in Ar⁺– Ar collisions for initial energy of 2·50 ev.

Figure 27 presents the results in the region of rainbow scattering using the reduced coordinates $\tau = E\chi$ and $\rho = 2\pi \chi \sin\chi \frac{d\sigma}{d\chi}$, in the elastic scattering and charge exchange regions. In these reduced coordinates, suggested by Smith et al [70], the rainbow maximum occurs at approximately the same τ value nearly independent of the collision energy. The rainbow maximum was found to be in agreement, within experimental error, with that measured by Vestal et al [69] in both the charge exchange and elastic regions.

The energy distributions have been converted to velocity distributions in cartesian coordinates and plotted on a contour diagram (figure 28). The velocity distribution follows the elastic circle indicating that no significant correction to the energy scale is needed for contact potentials.

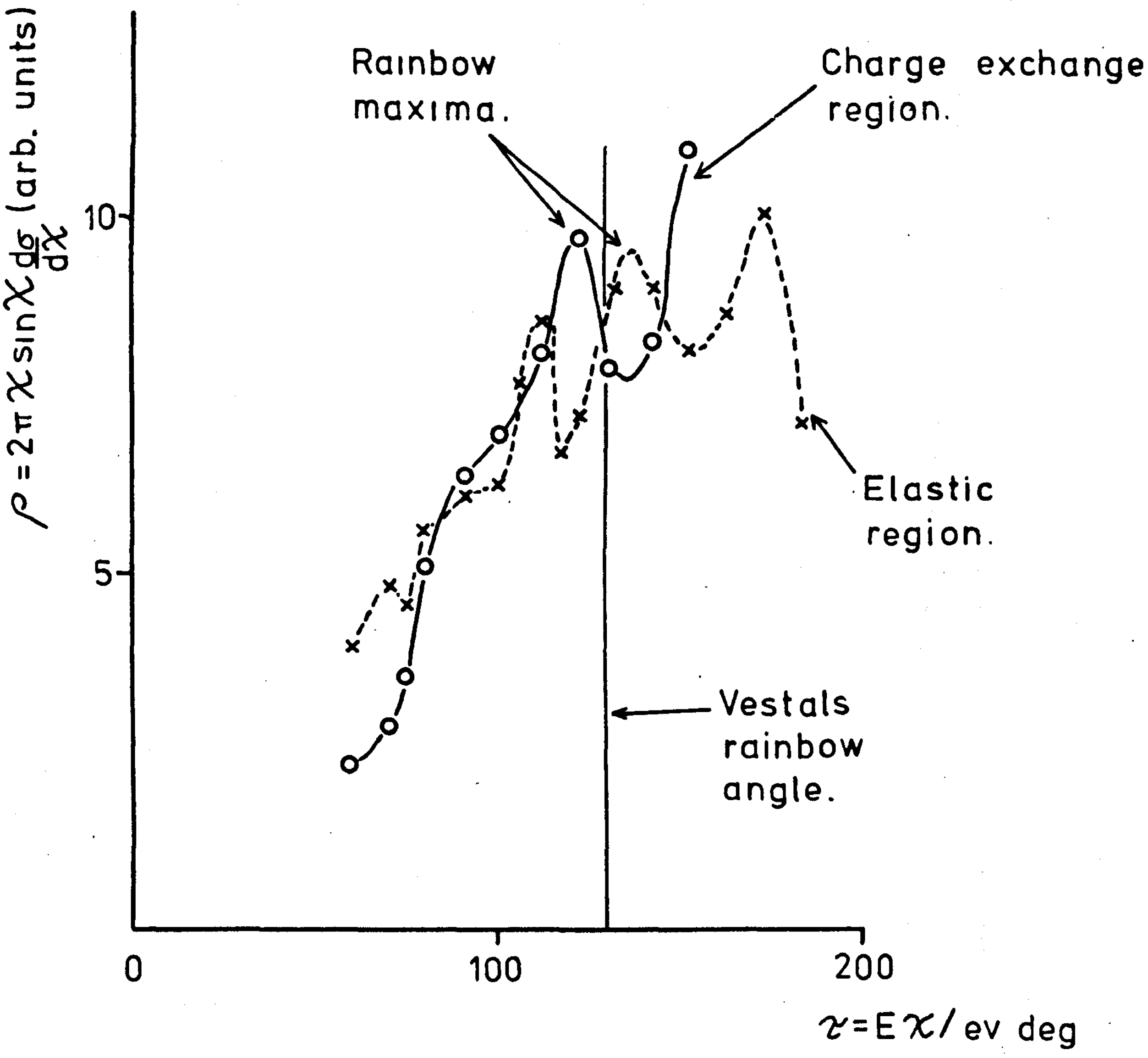

Figure 27. Ar⁺- Ar differential cross section plotted using the reduced coordinates $\tau = E\chi$ and $\rho = 2\pi\chi\sin\chi\frac{d\sigma}{d\chi}$.

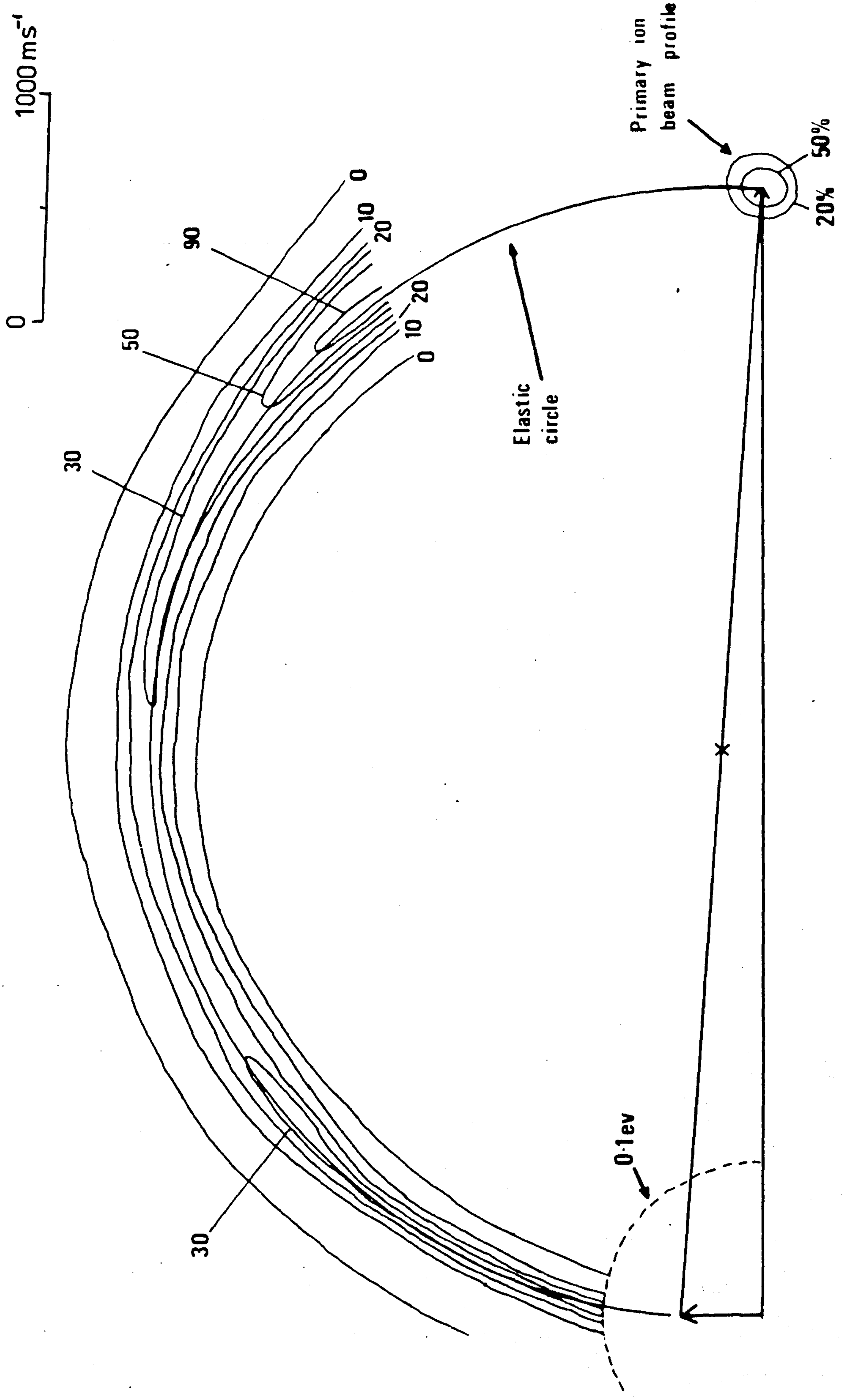

Figure 28. Contour diagram for Ar⁺- Ar charge exchange and elastic scattering for initial energy of 2·50 ev.

CHAPTER 4.

The reaction $CO^+ + O_2 = CO_2^+ + O$.

4.1 Introduction.

It is known from flowing afterglow [71] and SIFT [72] studies that at thermal energy the reaction between CO^+ and O_2 leads exclusively to O_2^+ in spite of the fact that for ground state reagents the reaction

$$CO^+(X^2\Sigma^+) + O_2(^3\Sigma_g^-) = CO_2^+(X^2\Pi_g) + O(^3P) \qquad 4.1$$

is exothermic by 0.58 ev [2] and is spin allowed. Energy dependent studies using the injected ion drift tube method [73] show that the cross section for charge exchange falls from about 20 Å^2 to 1 Å^2 (1Å = 0.1 nm) over the relative energy range of 0.04 to 3 ev, and no other reaction was observed. In contrast we find that reaction 4.1 occurs effectively over the energy range 1.8 to 10.1 ev.

Since CO_2^+ was not detected in thermal energy SIFT experiments reaction 4.1 apparently possesses a translational energy threshold, and thus appears to be an exception to the long established maxim that simple exothermic ion-molecule reactions proceed without an activation barrier. The microscopic molecular dynamics of reaction 4.1 are potentially fairly complicated since there exists the possibility that the freed oxygen atom could be derived from the CO^+ as well as the O_2 . Intensity contour diagrams of the product distribution will be presented below. In addition to CO_2^+, C^+, O^+, and O_2^+ have been detected from $CO^+ + O_2$ collisions, and the LAB angular distributions of these ions have been measured. As discussed below it is believed that the reactant CO^+ is almost all in the ground electronic state. The spectroscopy of CO_2^+ has been fairly extensively studied [74] and the ion is linear in both the $X^2\Pi_g$ ground state and in the low lying excited electronic states.

4.2 Results and discussion.

The CO^+ ions are produced by 35 ev electron impact on CO (BOC, research grade). The neutral beam was produced from O_2 (BOC, research grade, 99.98% pure). Electron impact on CO gives CO^+ predominantly in the $X^2\Sigma^+$, $A^2\Pi$, and $B^2\Sigma^+$ states. The CO^+ B state has a lifetime of the order of 5×10^{-8} s [75], and radiates rapidly to the ground state. The A state is longer lived, but it can be estimated from the radiative lifetime (of the order of $2\text{-}4 \times 10^{-6}$ s [76]), and the electron impact cross sections of the three states [77], that less than 1% CO ($A^2\Pi$) reaches the crossing region.

Several workers have investigated the reaction [78,79]

$$CO^+ + CO = C_2O^+ + O$$

and suggested that a long lived excited electronic state of CO^+, possibly $^4\Sigma$ (which has not been observed experimentally), is responsible. Ryan and Stock [79] have estimated that approximately 1% of the CO^+ produced by 35 ev electron impact is in the postulated $^4\Sigma$ state, although Moran et al [80] have suggested that there may be more than 1%. However, it seems unlikely that such small amounts of either the A state or a metastable quartet state should be responsible for the intensities of product observed under crossed beam conditions.

The $CO^+(X^2\Sigma^+)$ produced by direct electron impact can be estimated from Franck-Condon factors to be predominantly in the v=0 state. However transitions from the A and B states enhance the populations of higher vibrational levels. Moran et al [80] have calculated the vibrational state distributions for a range of impacting electron energies. Their calculations indicate that at 30 ev although the v=0 level is predominantly populated (approximately 70%), vibrational levels up to v=5 have populations greater than 1%. Since in general the various vibrational relaxation processes appear inefficient [81], particularly for the ground states, it seems unlikely that there will be any substantial vibrational relaxation of the CO^+. In addition there exists the possibility that there may be a degree of collisional excitation occurring as the ions travel through the quadrupole. As no attempt has been made to monitor the pressure along the length of the source analyser it is not possible to estimate any contribution this is likely to make.

Reaction 4.1 was studied at six energies over the relative energy range 1.8 - 10.1 ev. In addition to obtaining intensity contour diagrams for CO_2^+ the LAB angular distributions were measured for the ions C^+ , O^+ , and O_2^+ resulting from $CO^+ + O_2$ collisions. Although the LAB angular distributions cannot be directly related to the total cross sections, some qualitative conclusions can be drawn.

The intensity of O^+ is very low at low initial translational energies but rises between 3.6 and 5.0 ev, and increases further as the relative translational energy is raised. At 10 ev the O^+ intensity is significantly larger than the CO_2^+ intensity. Since the rise in O^+ intensity occurs in the range of initial relative energies where the formation of CO_2^+ with internal energy greater than the dissociation limit or dissociative charge transfer becomes energetically possible, the O^+ presumably arises from this rather than the exothermic reaction (ΔH = -0.73 ev, [2])

$$CO^+ + O_2 = O^+ + CO_2$$

The C^+ is present at very low intensity even at low initial translational energy, and the intensity increases slightly as the energy is raised. Since channels for C^+ formation are very endothermic it seems that a long lived excited state of CO^+ must be involved. The angular distribution of O_2^+ is broad.

Since no previous measurements of the total cross section for reaction 4.1 have been made, the relative cross sections have been obtained from the contour diagrams using the relationship

$$\sigma_R = 2\pi \int_0^{\pi}\int_0^{\infty} I_c(u,\chi) \sin\chi \, u^2 \, du \, d\chi$$

where $I(u,\chi)$ is the product intensity distribution in cartesian coordinates, and u and χ are the CM velocity and scattering angle respectively. A plot of the relative cross section (σ_R) versus initial translational energy (T) is shown in figure 29. Because of the difficulty in measuring total product and reactant fluxes in a crossed beam apparatus, absolute values have not been assigned to these measurements, and the relative values are probably only accurate within a factor of 2-3. Figure 29 shows that the cross section rises rapidly to a peak at initial relative energies around 5 ev (CM) and then decreases as the initial energy is further raised and it becomes increasingly

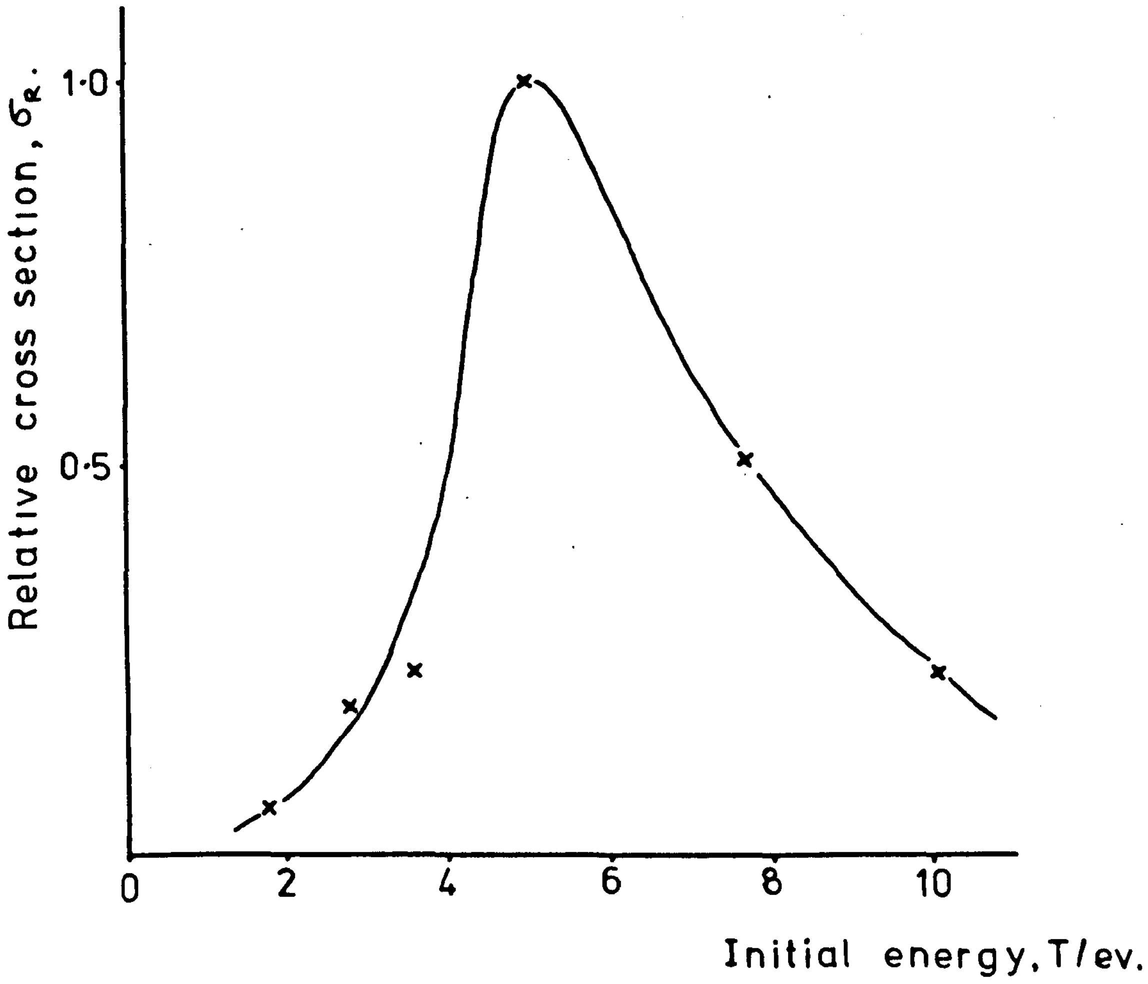

Figure 29. Plot of relative cross section, σ_R, (obtained from the contour diagrams) versus initial relative kinetic energy, T, for the reaction $CO^+ + O_2 = CO_2^+ + O$.

difficult to form ground state products with internal energy less than the dissociation limit. Since CO_2^+ is not observed from thermal CO^+ + O_2 collisions there must be a translational energy threshold to reaction. Excitation functions of this form are usually associated with endoergic ion-molecule reactions. A possible explanation for the variation of cross section with energy is to suggest the existence of an avoided surface crossing. Collisions at low energy lead to charge transfer but as the energy is increased crossings to a surface leading to CO_2^+ + O become more probable. However it seems unlikely that the fall in the charge transfer cross section can be attributed to competition with the atom transfer channel since the charge transfer cross section is much less than the Langevin collision cross section [73]. A more rigorous analysis awaits potential energy hypersurface (PEH) calculations.

Paulson [82] has subsequently measured the variation of cross section with energy for reaction 4.1 from threshold to 5 ev. His results show a threshold at approximately 0.5 ev and then virtually no variation with increasing energy, the cross section averaging around 0.5 $\mathring{A}^2$. The discrepancy between these results and those of Paulson could be due to the use of CO^+ derived from 98 ev electron impact on CO_2 in his measurements. This may contain substantial components in electronically and vibrationally excited states.

The translational exoergicity Q defined as $Q = T' - T$, where T and T' are the initial and final relative translational energies, has the limits $-\Delta E > Q > -(D + \Delta E)$, where $-\Delta E$ is the reaction exoergicity, and D is the dissociation energy of the product. Using the thermochemical dissociation energies [2] for D, and assuming that the reactants are in their ground electronic and vibrational states, and that the products are in ground electronic states, Q has the limits $+0.58 > Q > -4.72$ ev, for dissociation into the lowest energy fragments $O^+(^4S)$ + $CO(X\,^1\Sigma^+)$. For dissociation into the next lowest energy channel $CO^+(X\,^2\Sigma^+)$ + $O(^3P)$ the limits for Q would be $+0.58 > Q > -5.10$ ev. As will be discussed below the observed dissociation threshold is consistent with dissociation to $O^+(^4S)$ + $CO(X\,^1\Sigma^+)$. In all the contour diagrams measured no significant intensity lies outside the $Q = +0.58$ ev circle.

All the contour diagrams are asymmetric with respect to the ±90° axis indicating that the reaction proceeds by a direct mechanism over the whole energy range studied. This would be expected since CO_3^+ is unlikely to have a potential well of any significant depth. Seick and Gorden [83] have argued that as there is no evidence for the formation of CO_3^+ in a high pressure photoionisation study of $CO - CO_2 - O_2$ mixtures. The binding energy in CO_3^+ is less than in the cluster ion $(CO_2.O_2)^+$.

Integrations of the contour diagrams to obtain the 3D-CM angular distributions (or relative differential cross sections as a function of CM scattering angle) from

$$I(\chi) \simeq \sin\chi \int_0^\infty I_c(u,\chi)\, u^2\, du$$

show that the product CO_2^+ is mainly forward scattered at the lowest energy (figure 30). As the initial energy is raised

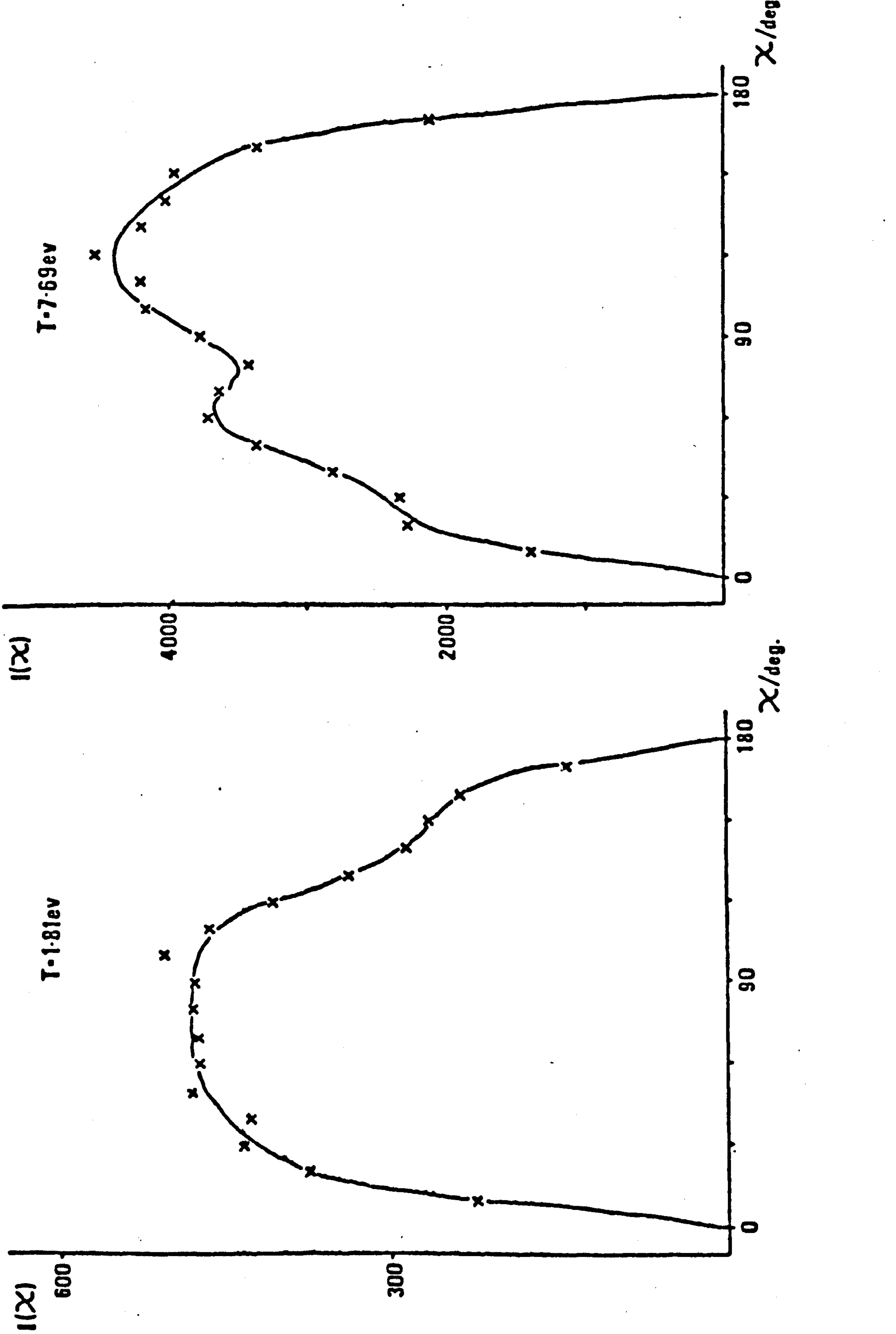

Figure 30. 3D-CM angular distribution of CO_2^+ from $CO^+ + O_2$ collisions for initial relative kinetic energies of 1·81 and 7·69 ev.

there is an increase in backward scattering and the product becomes mainly backward scattered (figure 30). As the energy is further raised there is an increase in wide angle scattering and the scattering again becomes mainly forward. Figure 31 shows the 3D-CM angular distribution at 10.12 ev. The shift from mainly backward to mainly forward scattering in the high energy regime is presumably due to product stability restrictions. (NB unless otherwise specified the terms forward and backward scattered will be taken to mean product with CM scattering angle $\chi < 90°$ and $\chi > 90°$ respectively, 0° being taken as the direction of the reactant ion velocity vector.)

Figures 32, 33, 34, 37, and 39 present the relative intensity contour diagrams measured at initial relative kinetic energies of 1.81, 2.78, 5.04, 7.69, and 10.12 ev. The contour diagram measured at the lowest initial energy $T = 1.81$ ev (figure 32), shows a broad forward peak with a low intensity tail extending past the CM, and a smaller backward peak with a narrower velocity distribution. There is a large uncertainty in the intensity (±50%) and position (±20%) of the backward peak. Large uncertainties in the apparent intensities of low energy components in the presence of substantial intensity of higher energy components is a well known problem with RPD energy analysers. The wide angular and velocity distribution of the forward peak suggests that at this energy the system passes through a region of the potential energy hypersurface in which all four atoms are strongly coupled.

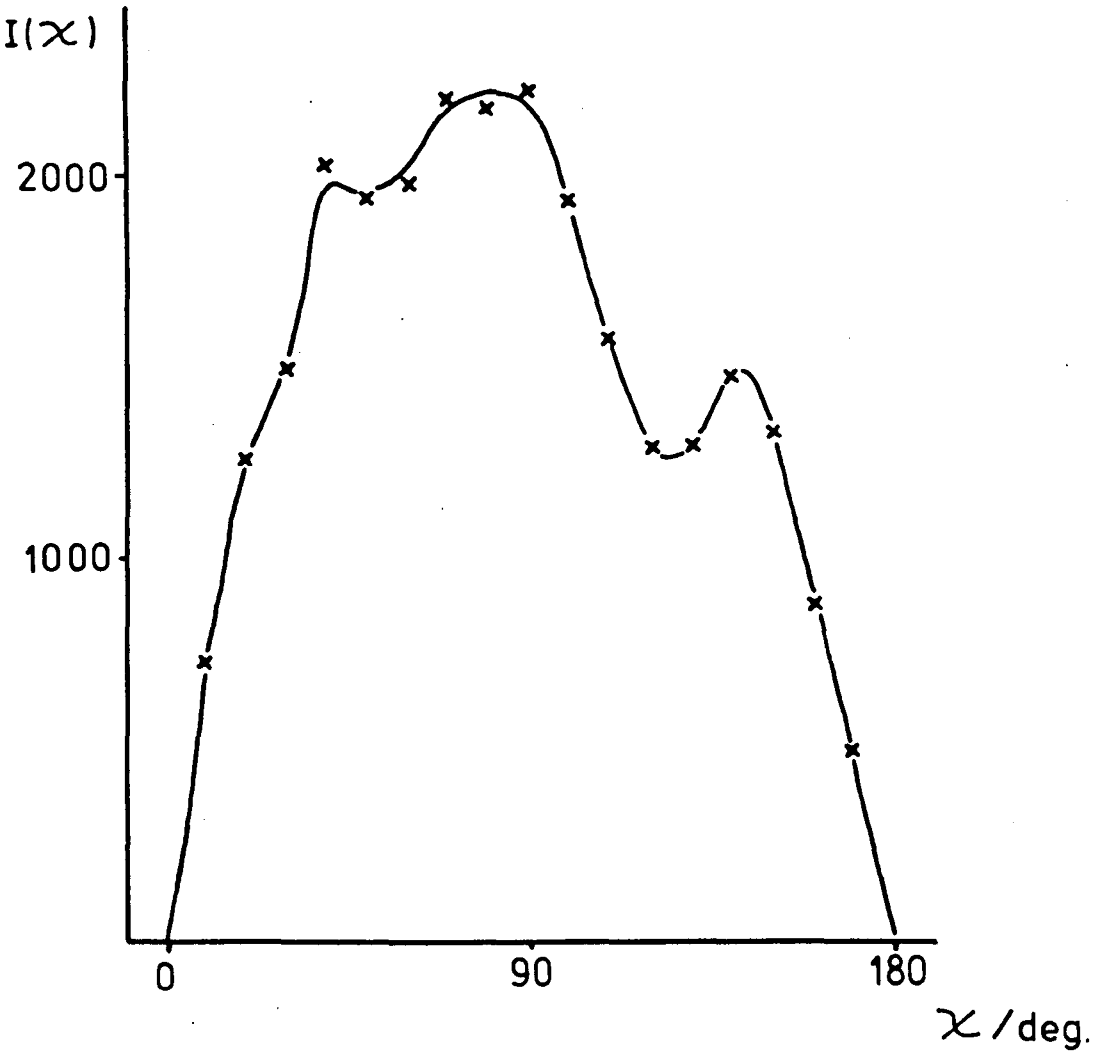

Figure 31. 3D-CM angular distribution of CO_2^+ from $CO^+ + O_2$ collisions for initial energy of 10·12 ev.

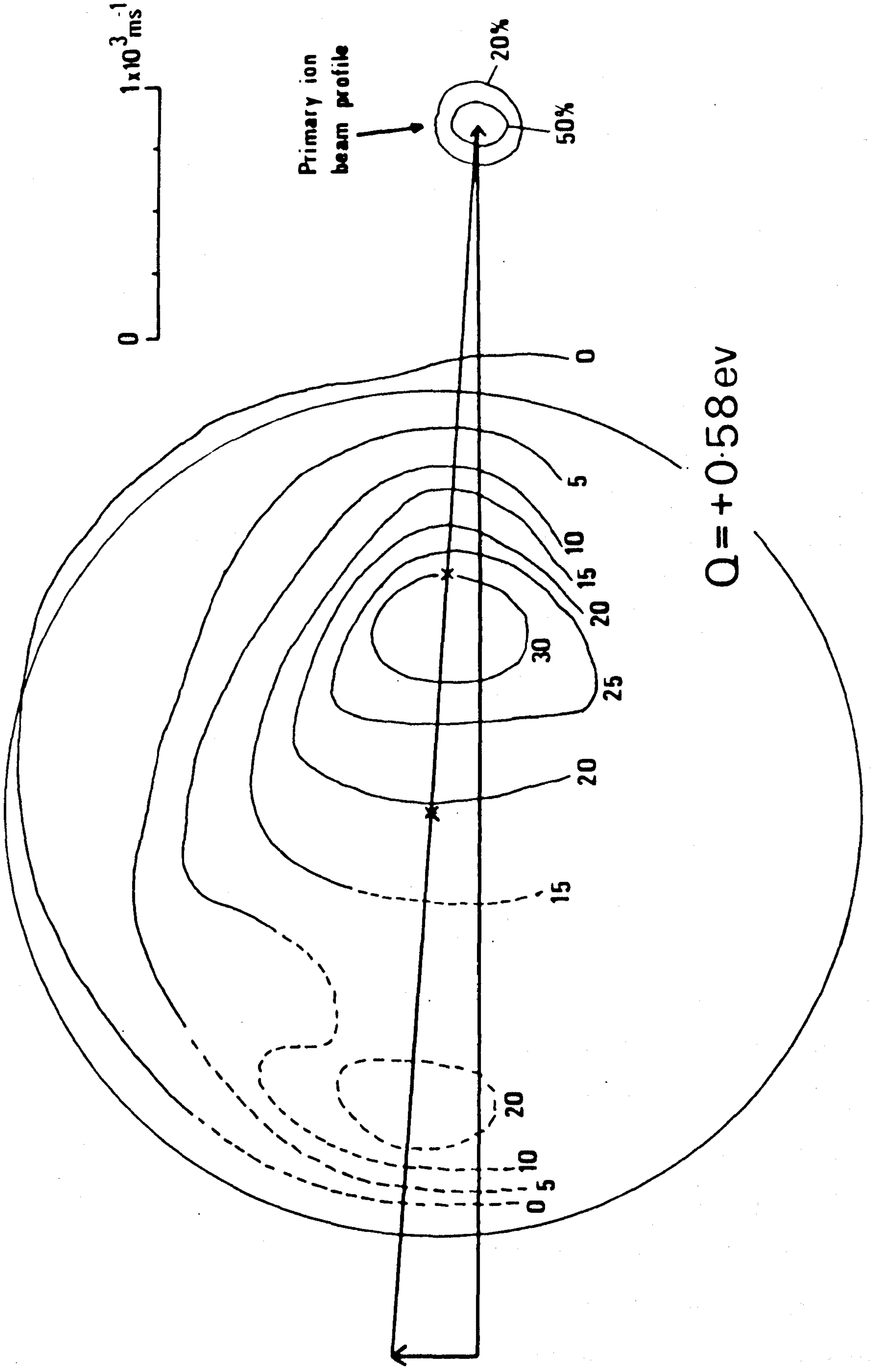

Figure 32. Contour map of intensity of CO_2^+ from $CO^+ + O_2$ collisions for initial relative kinetic energy of 1·81 ev. Crosses mark centre of mass and spectator stripping velocity.

These distributions clearly cannot be represented by dynamical models which assume delta function distributions, such as spectator stripping [27] or polarisation stripping [31] models, or models which lead to very narrow distributions such as spectator stripping with neutral internal motion [33] or the DIPR model [34]. Trajectory calculations for the reaction $Ar^+ + D_2$ [35] have shown that forward scattering can arise not only from grazing collisions but also from a migration mechanism which involves strong interaction between all atoms, and can lead to an appreciable range of momentum transfer. The extra degrees of freedom in a four centre collision might be expected to further broaden the angular and velocity distributions.

As the initial energy is raised to T = 2.78 ev (figure 33) the forward peak becomes narrower and clearly lies at a CM velocity lower than predicted by the spectator stripping model. As the initial energy is further raised to 5.04 ev (figure 34), the angular and velocity distributions of the forward peak have become even narrower as the mechanism becomes more impulsive. The backward peak increases relative to the forward peak as the energy is raised, and lies at a CM velocity greater than the forward peak and outside the elastic stripping circle. (The elastic spectator stripping model is an extension of the spectator model proposed by Herschbach [40] to include rebound reactions. The spectator instead of continuing with an unchanged velocity vector undergoes ordinary elastic scattering with the incipient product.) These results indicate that the backward scattered

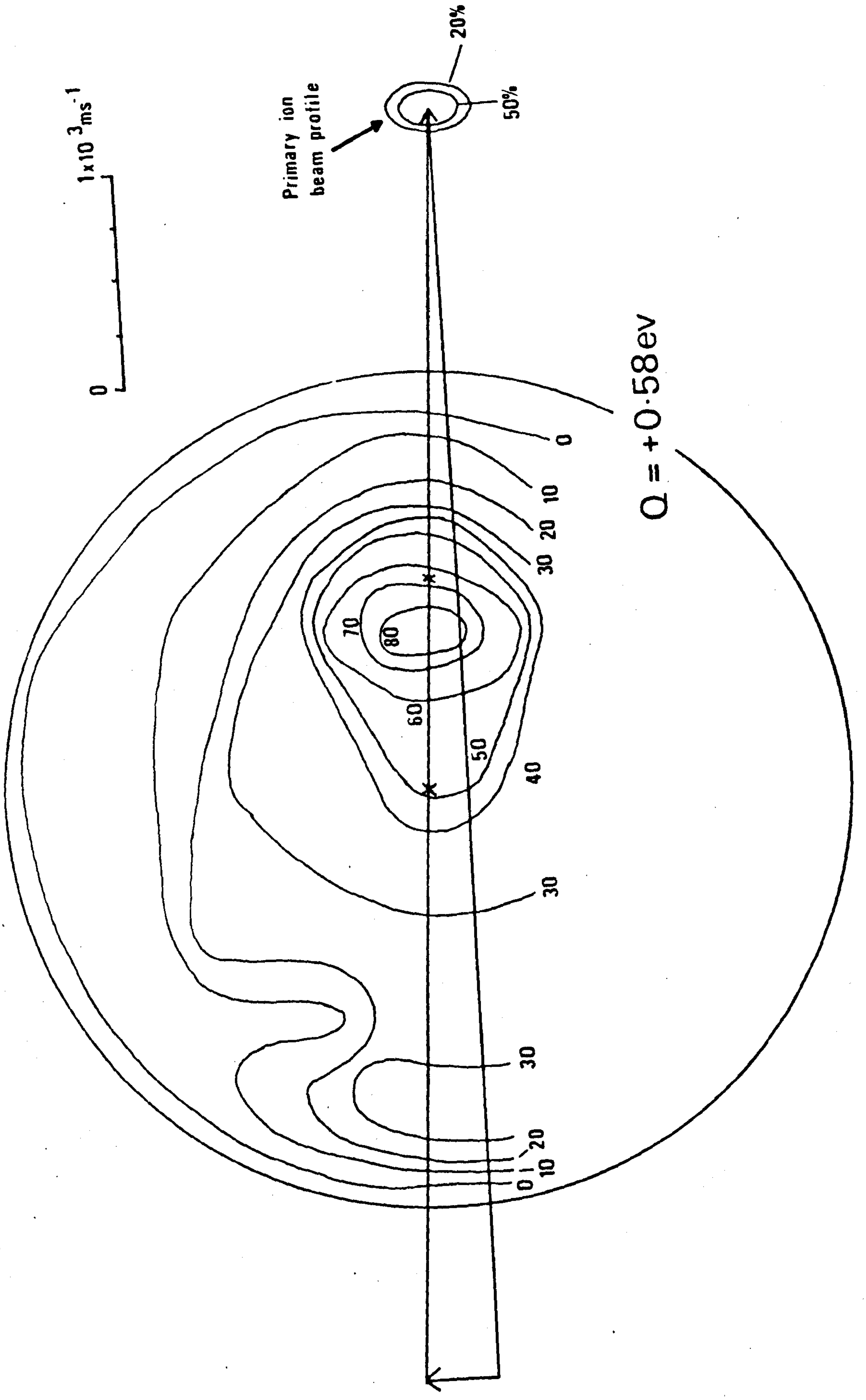

Figure 33. Contour map of intensity of CO_2^+ from $CO^+ + O_2$ collisions for initial energy of 2·78 ev.

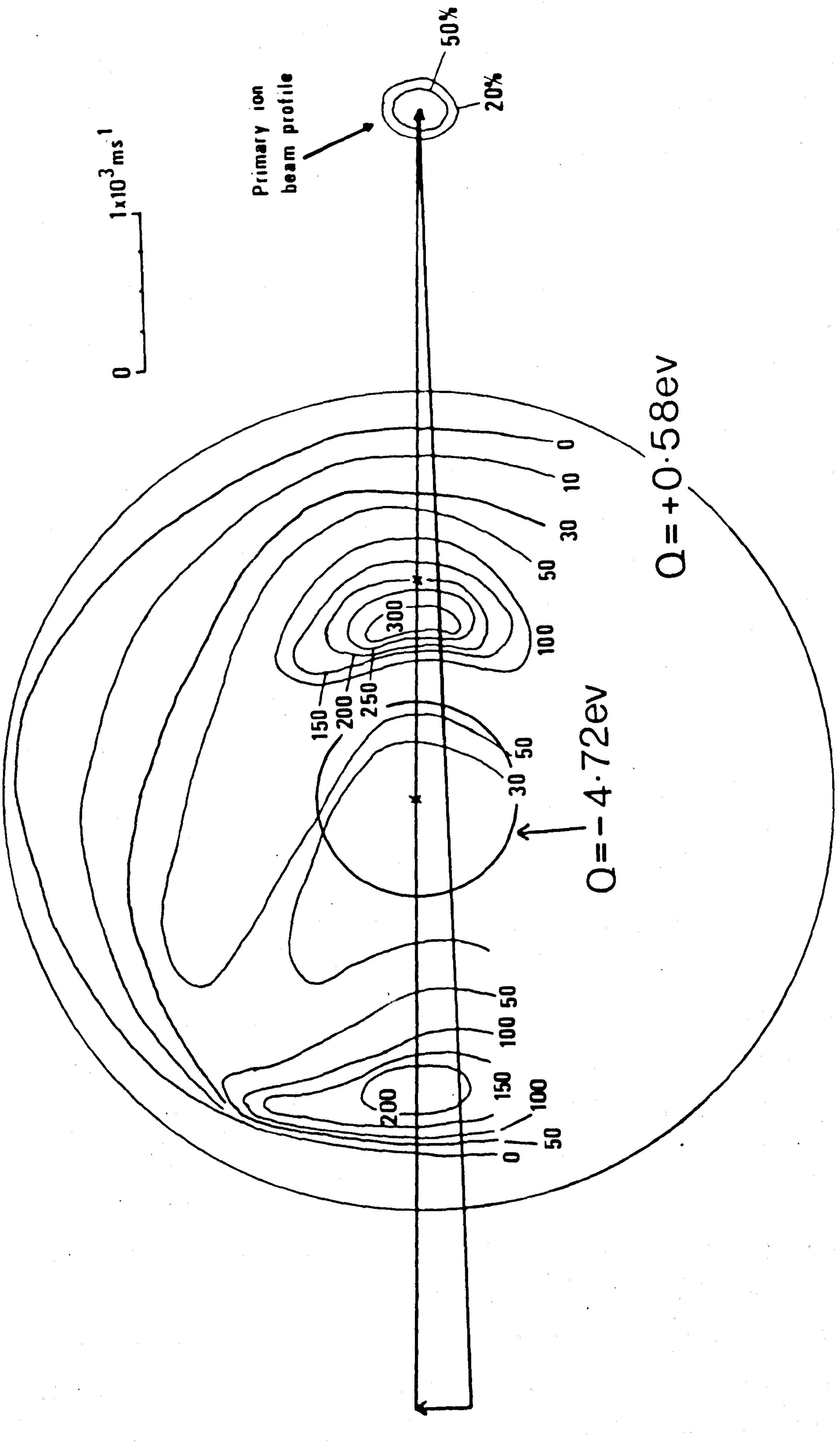

Figure 34. Contour map of intensity of CO_2^+ from $CO^+ + O_2$ collisions for initial energy of 5·04 ev.

intensity arises from a mechanism which allows product recoil and leads to lower internal excitation than the forward scattered intensity. This suggests that the backward scattering arises from low impact parameter collisions in which all atoms strongly interact. A simple model which can be used to rationalise the observed recoil is suggested in the following chapter.

A plot of the most probable translational exoergicity (Q_{MP}) against the initial relative translational energy (T) (figure 35), shows that the most probable internal excitation increases more rapidly than predicted by the spectator stripping model. This indicates the conversion of a constant fraction of the kinetic energy of the freed atom into internal energy of the product. These results cannot be rationalised in terms of any of the simple models used to discuss the dynamics of ion-molecule reactions. Since most of these models were derived from studies of reactions of the type $A^+ + H_2 = AH^+ + H$ these models are generally small perturbations of the stripping mechanism. These results indicate coupling of the motion of all atoms in reactive collisions and imply that when the O atom is transferred to CO^+ to form CO_2^+ it is still coupled to the other O atom, and some fraction of the relative energy of the product O atom is transfered to the internal energy of the CO_2^+. Alternatively this behaviour could indicate that a four centre collision is occurring, in which the freed O atom could be envisaged as interacting with one or both of the atoms in CO^+ as the O atom is transferred. It would seem possible that a collision of this type could lead to forward

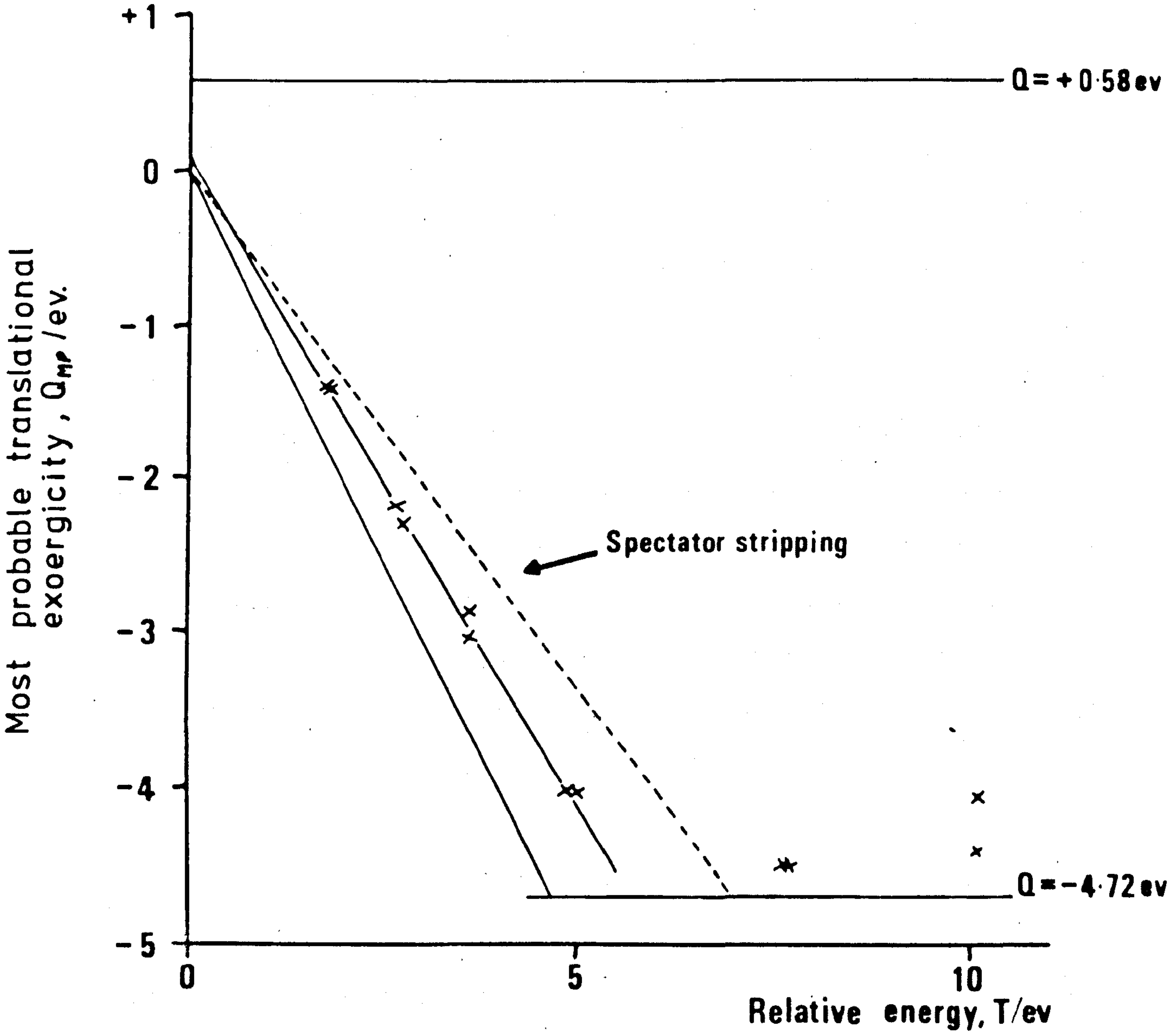

Figure 35. Plot of most probable translational exoergicity (Q_{mp}) versus initial relative kinetic energy (T) for the reaction $CO^+ + O_2 = CO_2^+ + O$

scattering because of the focussing effect of the ion-induced dipole potential as the products separate.

It should be noted that in the data presented here the most probable translational exoergicities have been derived from the maxima in the LAB energy distributions. It could be argued that the most probable product translational energy should be derived from the maximum in the $I_c(u,\chi).u$ distribution. This however introduces negligible error. In some cases the LAB energy distributions have been transformed to cartesian coordinates and the most probable product translational energy is derived from the maximum in the cartesian distribution. It should be noted that this introduces additional distortion into the data, since in cartesian coordinates the intensities are proportional to the probability of velocity vectors with components between v_x and $v_x + dv_x$, etc., rather than to intensity with translational energy of magnitude between T' and $T' + dT'$ into some solid angle dw.

The distribution of relative translational energy of the products $P(T')$ was obtained by 3D integration of the intensity on the contour diagrams using

$$P(T') = u \int_0^{\pi} I_c(u,\chi) \sin\chi \, d\chi$$

In the integration the relative weight of the forward peak is rather low in comparison with the total intensity, the distribution being to a large extent determined by sideways scattered intensity. Over the energy range 1.81 to 5.04 ev the maximum in the $P(T')$ distribution lies at a lower relative energy than predicted by the spectator stripping model with the deviation increasing as the energy is raised (Figure 36).

As the initial energy is raised above 5 ev the total cross section declines due to dynamic restrictions placed on product stability. The distribution of CO_2^+ from $CO^+ + O_2$ collisions at an initial energy of 7.69 ev is shown in figure 37. The trend towards increased backward scattering continues and figure 30 shows that the product is predominantly backward scattered at this initial energy. The maximum of the forward peak lies just outside the Q = -4.72 ev circle. The spectator stripping point lies just within the Q = -4.72 ev circle and it is clear from the contour diagram that product stability restrictions are beginning to dominate the dynamics. The increase in backward scattering shows that rebound collisions in which all atoms interact strongly are more effective in producing stable products than collisions which lead to forward scattering. As the initial relative translational energy is raised an increasing fraction of the product is observed to fall within the circle Q = -4.72 ev. There is however a dissociation threshold clearly evident around Q = -4.72 ev. In addition the plot of Q_{MP} versus T (figure 35) in this energy range shows that the most probable translational exoergicity is invariant with initial energy as the forward peak is "eaten away" by product stability restrictions. The deviation of the data from the Q = -4.72 ev line arises from the finite resolution of the instrument. An analysis of this indicates that it is unreasonable to suggest that the data is displaced from the Q = -5.10 ev threshold. This suggests

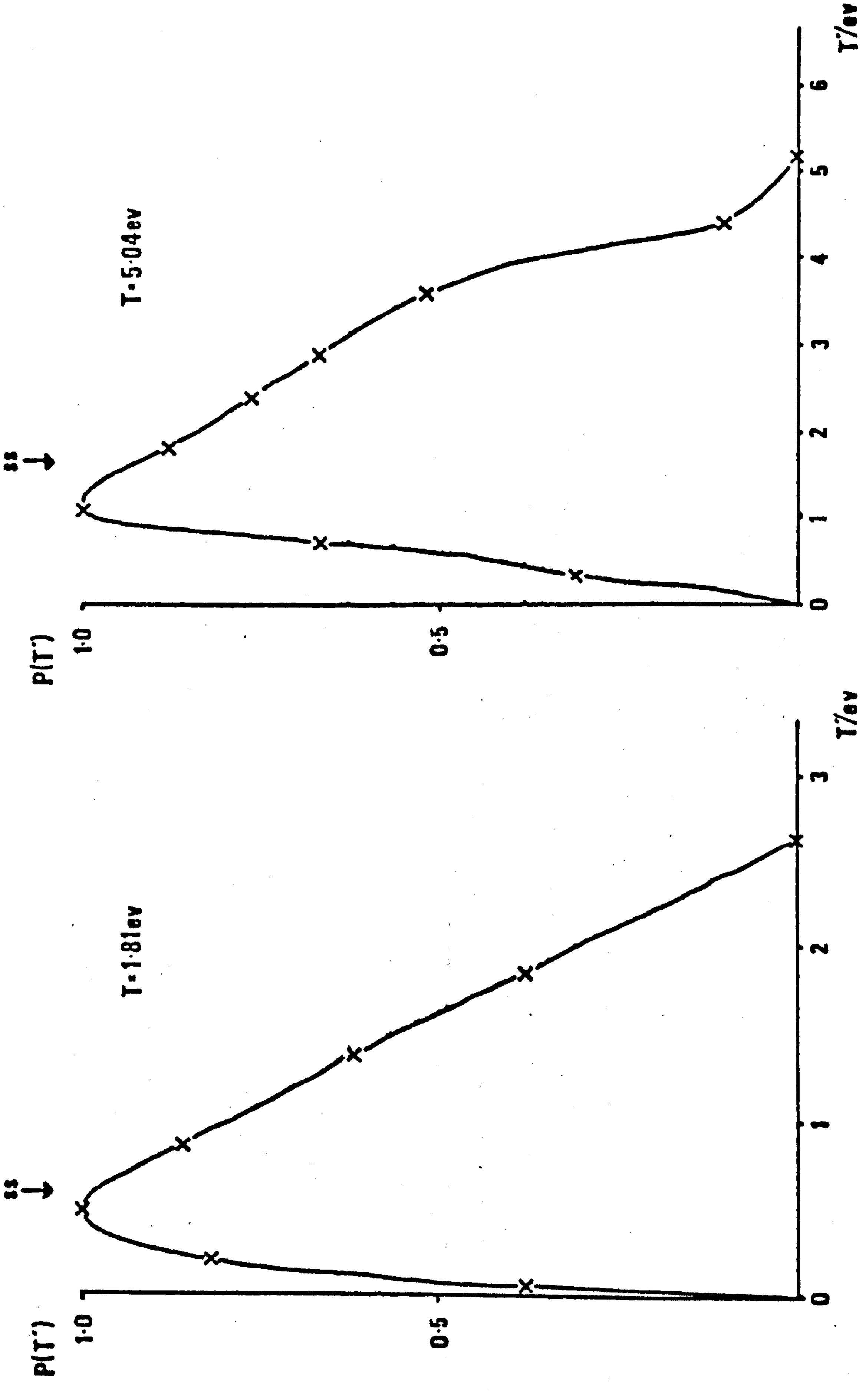

Figure 36. Product translational energy distribution, P(T′), of the reaction $CO^+ + O_2 = CO_2^+ + O$ for initial relative kinetic energies of 1·81 and 5·04 ev.

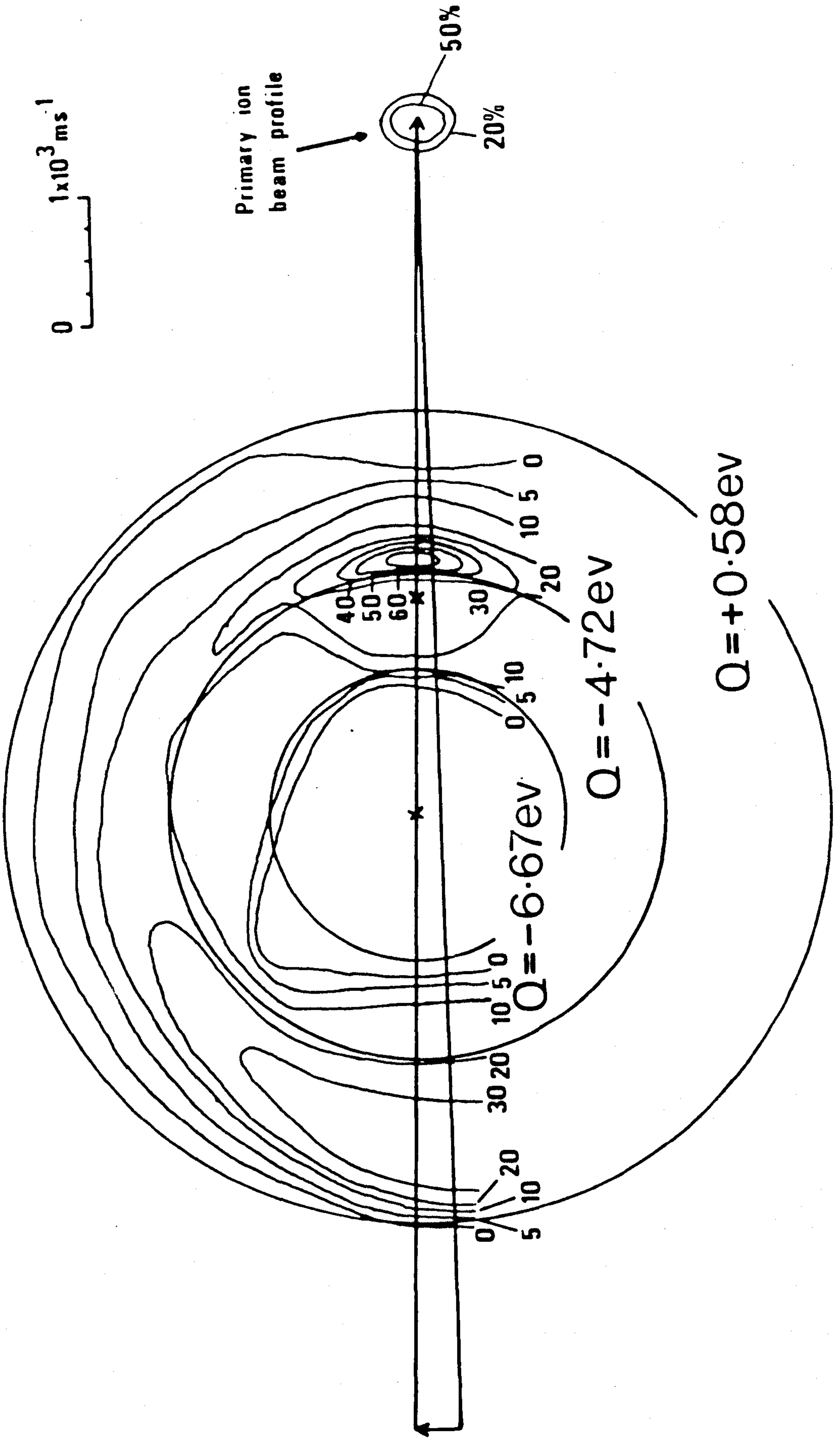

Figure 37. Contour map of intensity of CO_2^+ from $CO^+ + O_2$ collisions for initial energy of 7·69 ev.

(assuming ground state reactants) the possibility that most of the CO_2^+ formed in the higher vibrational levels of the $X^2\Pi_g$ state, which correlates adiabatically with $CO^+(X^2\Sigma^+)$ + $O(^3P)$, undergoes a spin forbidden predissociation before reaching the detector via a repulsive $^4\Sigma$ state which correlates with $O^+(^4S) + CO(X^1\Sigma^+)$. The C state of CO_2^+ is known to be completely predissociated [84]. This suggestion is consistent with the rise in O^+ intensity observed in the range of initial kinetic energies where it becomes energetically possible for CO_2^+ to predissociate. Such behaviour has not been suggested before presumably because, as Franck-Condon calculations [85] and photoelectron spectroscopy (PES) [86] indicate, the vibrational levels of the $CO_2^+(X^2\Pi_g)$ state are not directly populated near the dissociation limit. However, the appearence potential of O^+ is close to the thermochemical dissociation limit in both photoionisation [87] and PES [86] studies. McCulloh [87] has ascribed this to predissociation with spontaneous ionisation of two Rydberg series of CO_2 converging on the C state.

Since most of the intensity occurs at $Q > -4.72$ ev this implies that for the majority of the collisions the neutral product is $O(^3P)$ and that all the internal excitation resides in the ionic product. For the product within the $Q = -4.72$ ev circle either O or CO_2^+ must be electronically excited. Although it is not possible to say unambiguously from the beam data alone which of the products is excited, the data is consistent with the assumption that the major excited product is $O(^1D)$ and that the CO_2^+ is not formed in an electronically excited state to any extent. The limits on

Q are then $-1.37 > Q > -6.67$ ev for the formation of $CO_2^+(X^2\Pi_g) + O(^1D)$ assuming that the CO_2^+ dissociates into the lowest energy fragments $O^+(^4S) + CO(X^1\Sigma^+)$. Intensity within the circle $Q = -6.67$ ev presumably arises from the finite angular and energy resolution of the instrument. Figure 38 shows the $P(T')$ distributions at 7.69 and 10.12 ev. It is clear that as the initial energy is raised the proportion of the products formed in electronically excited states increases.

At the highest initial relative energy (10.12 ev) at which an experiment was performed the contour diagram (figure 39) shows a forward peak and a small maximum at CM scattering angle $\chi \simeq 40°$, just outside the $Q = -4.72$ ev circle. The CM angular distributions (figure 31) show that there is an increase in wide angle scattering and that at this energy more intensity is scattered forwards than backwards. Since the backward peak lies within the stability limits for formation of the electronically excited products $CO_2^+(X^2\Pi_g) + O(^1D)$, this presumably indicates that the backward scattered product is predominantly electronically excited and that the product recoil observed at lower energies is insufficient to produce stable ground state product at this energy. The increase in wide angle scattering indicates that at this energy the dynamics are dominated by repulsive forces and product stability restrictions.

The spectator stripping point lies just within the $Q = -6.67$ ev circle, though the forward peak is retained having

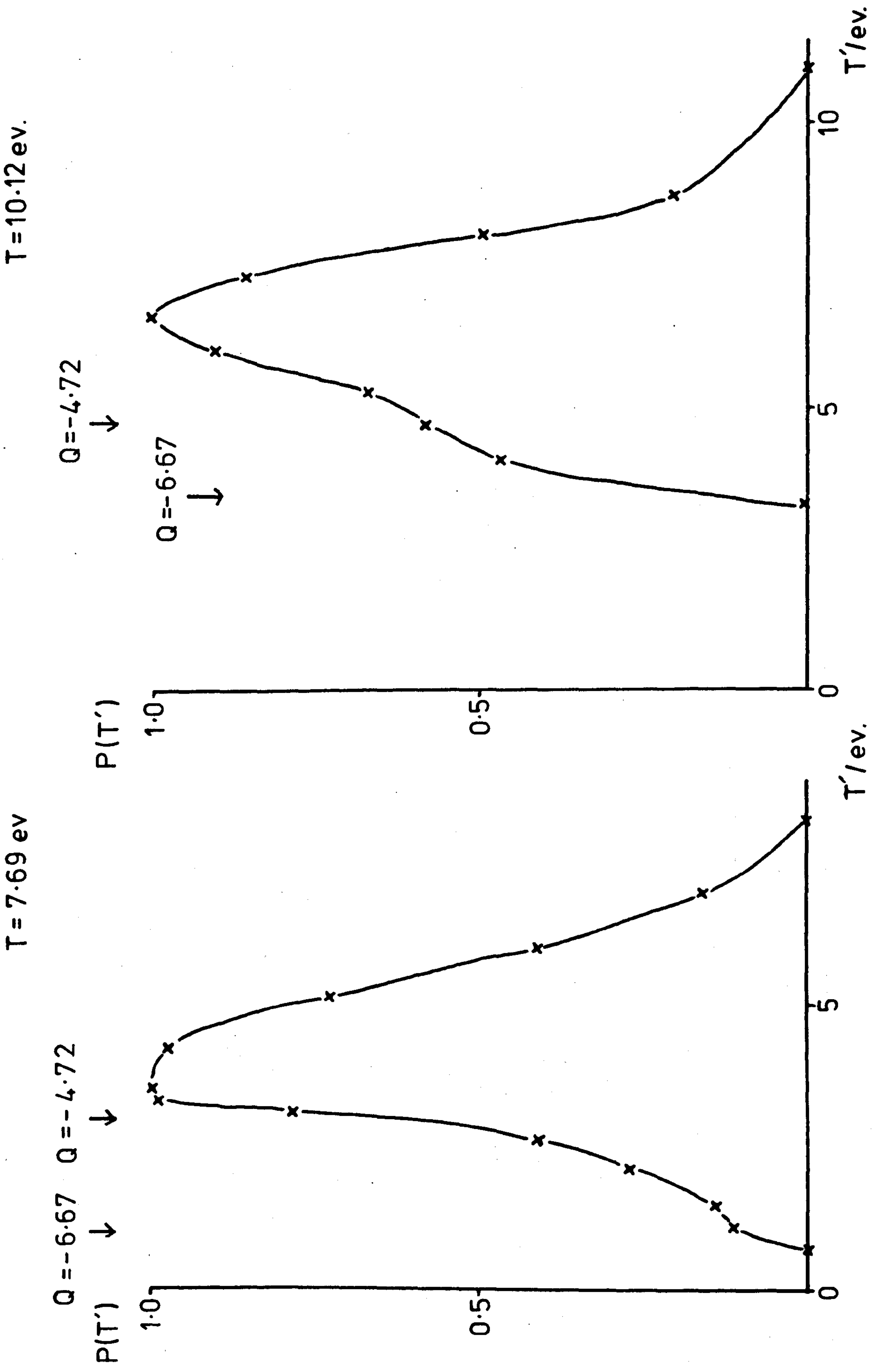

Figure 38. Product translational energy distribution, P(T′), of the reaction $CO^{+} + O_2 = CO_2^{+} + O$ for initial energies of 7·69 and 10·12 ev.

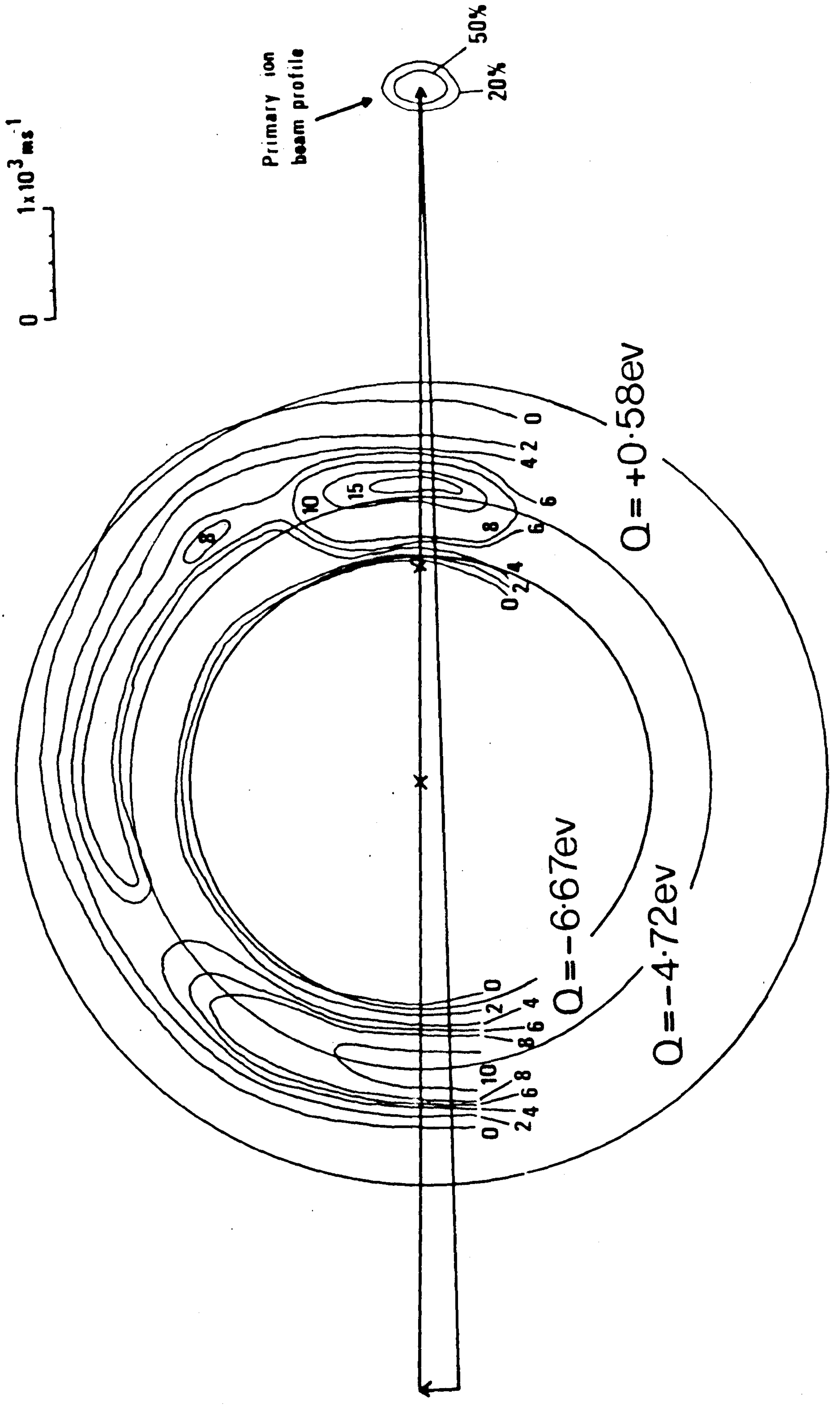

Figure 39. Contour map of intensity of CO_2^+ from $CO^+ + O_2$ collisions for initial energy of 10·12 ev.

been further "eaten away" by product stability restrictions and shifted to a higher velocity. In hydrogen atom transfer reactions it has been suggested [43] that forward scattered product arises from grazing collisions and that reaction exoergicity is usually related to the features of the potential hypersurface which allow forward recoil of product. However reaction 4.1 is not very exoergic and it appears that recoil substantially in excess of that due to the release of exoergicity as translational energy of the products is required to produce ground state forward scattered product. While the role of exoergicity may be important, it seems more likely that the forward scattered product at this energy arises from intimate collisions in which all atoms strongly interact (enabling substantial momentum transfer to occur between the incipient products) rather than grazing collisions. The focussing effect of the ion-induced dipole potential may be important in producing forward scattered product. The increase in wide angle scattering and the small maximum at $\chi \simeq 40°$ makes it attractive to speculate that sequential impulses are becoming an important mechanism for product stabilisation.

To investigate this it would be useful to compare the experimental results with the predictions of a simple hard sphere impulse limit model. Such a model can be derived by extending the sequential impulse model [42] to four centre collisions. However, since this model was found to have only limited success in interpreting the results it will only be briefly considered here. The assumptions of the model are a) collisions between atoms are elastic and impulsive, b) attractive forces are ignored except that they hold reactant molecules together before the collision, and may do the same for the product molecule after the collision, and c) reaction exoergicity is ignored. In addition only collisions in which the four atoms remain in a plane will be considered. The sequence of collisions in the reaction is collision between one of the atoms in CO^+ ion with one of the atoms in the O_2 molecule, followed by an independent elastic collisions in at least one of the diatomics, so that the velocity vector of one of the O atoms lies in the stability zone such that the internal energy of the product CO_2^+ is less than the dissociation limit. The second impulse transfers some of the CO^+ + O relative energy into translational energy of the freed atom, and thus may lead to stable product formation in cases where spectator stripping will not. The CO_2^+ product velocity vector is then determined from the definition of the CM system. The maximum CO_2^+ product CM velocity vectors are derived by the principles discussed by Mahan et al [42]. The derivation is reasonably straight forward but rather long and tedious and will not be discussed in detail here. The maximum product velocity vectors describe a cardioid with a cusp at the spectator stripping point. The allowed zone in velocity space is bounded from the inside by the stability circle and from the outside by the limiting cardioid. Stability zones for a number of series of sequential impulses are shown in figure 40. Sequential impulses in which the freed atom is derived from O_2 produce predominantly forward scattering, whereas if the freed atom is derived from CO^+ the scattering is predominently backward.

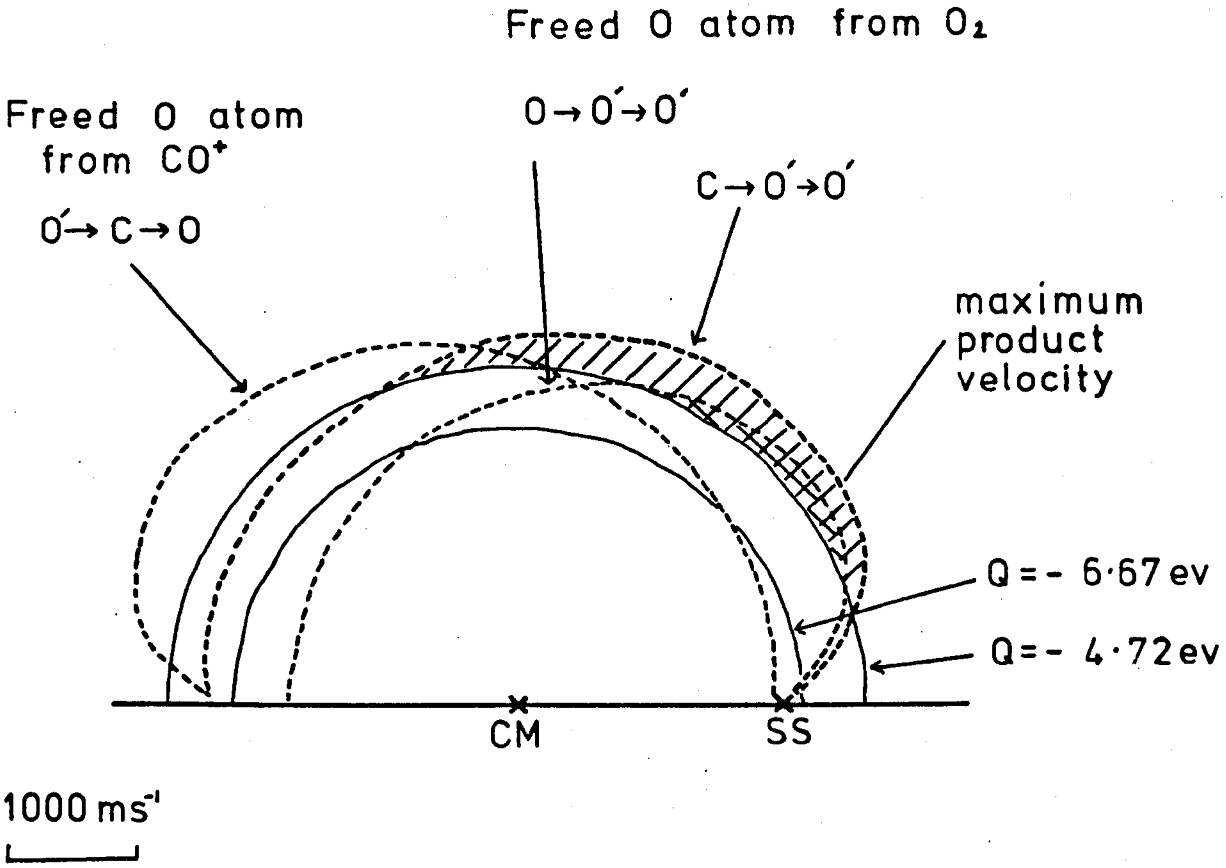

Figure 40. Some product stability zones of the four centre sequential impulse model for the reaction $CO^+ + O_2 = CO_2^+ + O$. Q stability circles are for an initial energy of 10·12 ev. (O′ represents an O atom derived from O_2)

The results at 10.12 ev can best be rationalised by considering only those collisions in which the freed atom is derived from the oxygen molecule. A reduction in backward scattering would be predicted, since stable ground state back scattered product cannot be formed by this mechanism. This is consistent with the observation that backward scattered product lies within the stability zone for electronically excited product. The extent of the wide angle scattering and the maximum at $\chi \simeq 40°$, where the product can be formed by two series of sequential impulses is also well predicted. There is however significant intensity outside the limiting cardioid which presumably results from coupling of the motion of the atoms in the collision. This model would also predict the loss of the peak at 0° which has been discussed above.

The model is not so successful at lower energies as the collision becomes less impulsive. At 7.69 ev the model would predict mainly forward scattering, however mainly backward scattering is observed. It would appear that the recoil observed in lower energy rebound collisions is still sufficient to produce ground state stable product at this energy. In conclusion it appears that this model only has limited success in interpreting the results, this is not surprising in view of the substantial coupling of the motions of the atoms observed at lower energy. Thus there seems little point in extending the model to out of plane collisions to obtain differential cross sections.

As noted above in addition to forming CO_2^+ by the "stripping" of an oxygen atom from O_2 by CO^+, there is the possibility of forming CO_2^+ by the "stripping" of C^+ by O_2. Although the four centre sequential impulse model suggests that this does not occur at the highest energy, this could be a consequence of the impulsive nature of the collision - the collision period being shorter than the natural frequency of nuclear motion; thus the O-O bond would have insufficient time to stretch for insertion of C^+. Presumably the potential well for COO^+ is insufficiently deep for it to be stable long enough to rearrange to CO_2^+.

At lower initial energy where the reactants are in close proximity for longer and there is substantial coupling between all atoms, "chattering collisions" may occur and the freed oxygen may well be derived from the CO^+ ion. An assessment of the feasibility of such processes would require high quality potential energy hypersurfaces and trajectory calculations. Such a process could explain the mainly backward scattered intensity observed in the intermediate energy range.

CHAPTER 5.

The reaction $CO^+ + NO = CO_2^+ + N$.

5.1 Introduction.

The reaction

$$CO^+ + NO = CO_2^+ + N \qquad 5.1$$

is 0.81 ev endothermic [2] for ground state reactants and products, and hence should provide interesting contrasts with the exothermic reaction 4.1 studied previously. The only reported reaction of CO^+ with NO is the charge exchange reaction

$$CO^+ + NO = NO^+ + CO$$

which is 4.75 ev exothermic [2]. The rate constant for charge exchange has been measured by the flowing afterglow method [88], and Kobayashi and Kaneko [73] have measured the charge exchange cross section as a function of initial translational energy by the injected ion drift tube method. However our work is believed to be the first reported observation of the ion-molecule reaction 5.1.

In addition to CO_2^+, another possible atom transfer product, $(NCO)^+$, was detected in the beam experiments. $(NCO)^+$ appears to be a minor product except at high energy where the total cross section for CO_2^+ formation is low. The dynamics of the reaction

$$CO^+ + NO = (NCO)^+ + O$$

will be discussed in detail in the following chapter.

5.2 Results and discussion.

Product intensity contour diagrams for CO_2^+ have been measured over the relative energy range 2.5 to 12 ev. A number of experiments were performed in which the energy distribution of the product CO_2^+ was measured only at the angle of maximum intensity in the angular distribution in order to determine the most probable translational exoergicity, Q_{MP}. The CO^+ ions were produced as described in chapter 4 and the neutral beam was produced from NO (BOC technical grade, 99.2% pure).

Since no previous measurements of the total cross section for reaction 5.1 have been made, the relative cross sections have been derived from the contour diagrams. Figure 41 shows a plot of the relative cross section versus the initial translational energy. Because of the difficulty in measuring total product and reactant fluxes in the crossed beam apparatus, absolute values have not been assigned to these measurements and the relative values are probably only accurate within a factor of 2-3. Figure 41 shows that the cross section rises to a peak at around 6 ev (CM) and then declines as it becomes increasingly difficult to form ground state products with internal energy less than the dissociation limit. Excitation functions of this form are usually associated with endoergic ion-molecule reactions.

The translational exoergicity Q, defined as $Q = T' - T$, where T and T' are the initial and final relative translational energies, has the limits $-\Delta E > Q > -(D + \Delta E)$,

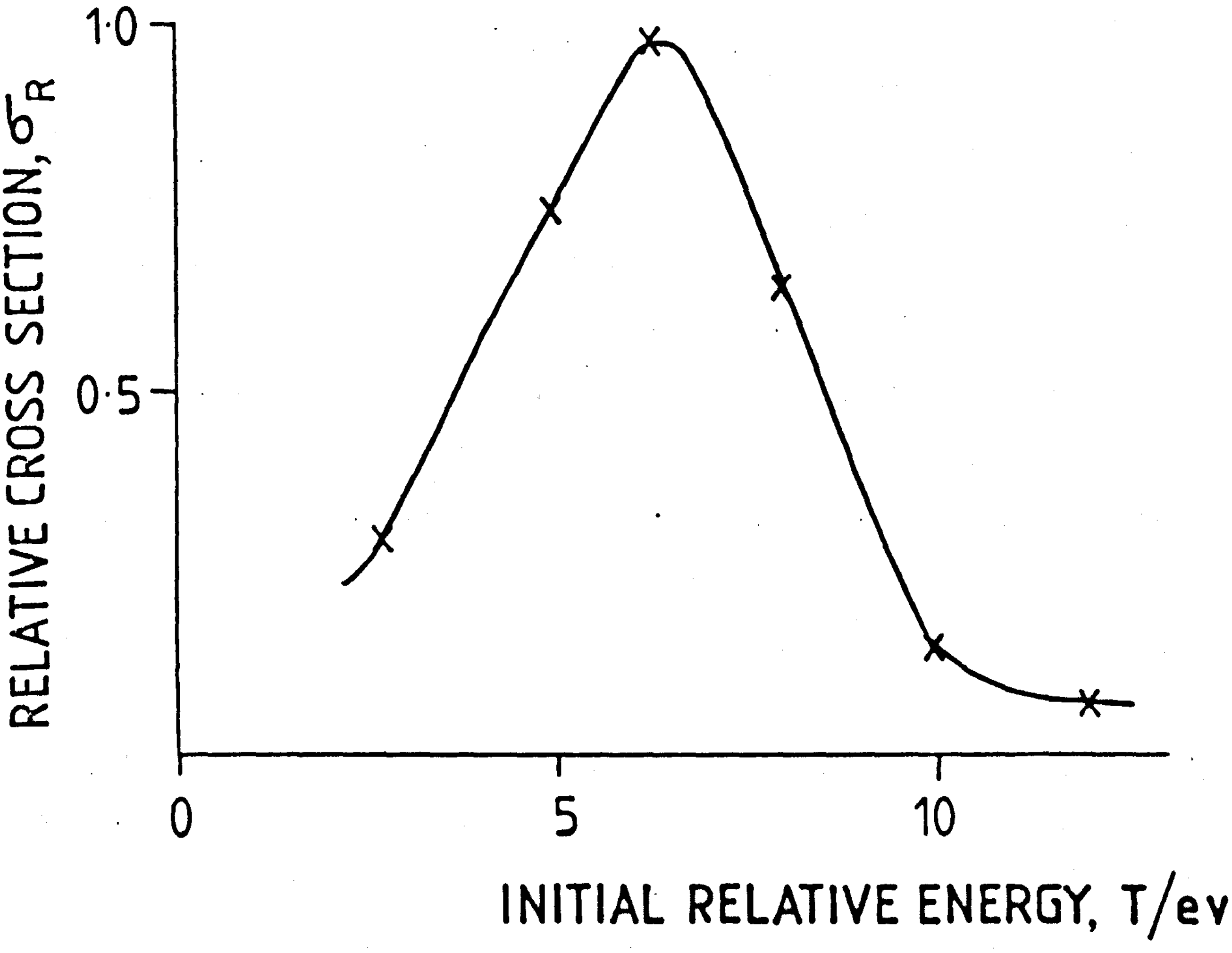

Figure 41. Plot of relative cross section, σ_R, (obtained from the contour diagrams) versus initial energy, T, for the reaction $CO^+ + NO = CO_2^+ + N$.

where ΔE is the reaction endoergicity and D is the dissociation energy of the product ion. For reaction 5.1 assuming that the reactants are in their ground electronic and vibrational states and that the products are in their ground electronic states, and using the thermodynamic dissociation energies [2] for D, Q has the limits $-0.81 > Q > -6.11$ ev for dissociation into the lowest energy fragments $O^+(^4S) + CO(X\,^1\Sigma^+)$. For dissociation into the next lowest energy channel $CO^+(X\,^2\Sigma^+) + O(^3P)$ the limits for Q would be $-0.81 > Q > -6.49$ ev. As will be discussed below the observed dissociation threshold is consistent with dissociation to $O^+(^4S) + CO(X\,^1\Sigma^+)$.

Figures 43, 45, 46, 48, 50, and 53 show the contour diagrams measured at relative energies 2.72, 4.92, 6.21, 7.91, 9.93, and 12.03 ev. These have been approximately normalised to unit beam strengths as described in section 3.7. The contour diagrams are all asymmetric with respect to the ± 90° axis, indicating that the reaction proceeds by a direct mechanism over the whole energy range studied. The 3D-CM angular distributions obtained by integration of the intensity on the contour diagrams show that the product is predominantly forward scattered over the whole energy range (figure 42). In contrast CO_2^+ product from $CO^+ + O_2$ collisions was found to be predominantly backward scattered in the intermediate energy range. As noted above, it is possible that this is due to product in which the freed O atom is derived from the CO^+. This cannot occur in reaction 5.1. No significant intensity lies outside the $Q = -0.81$ ev circle.

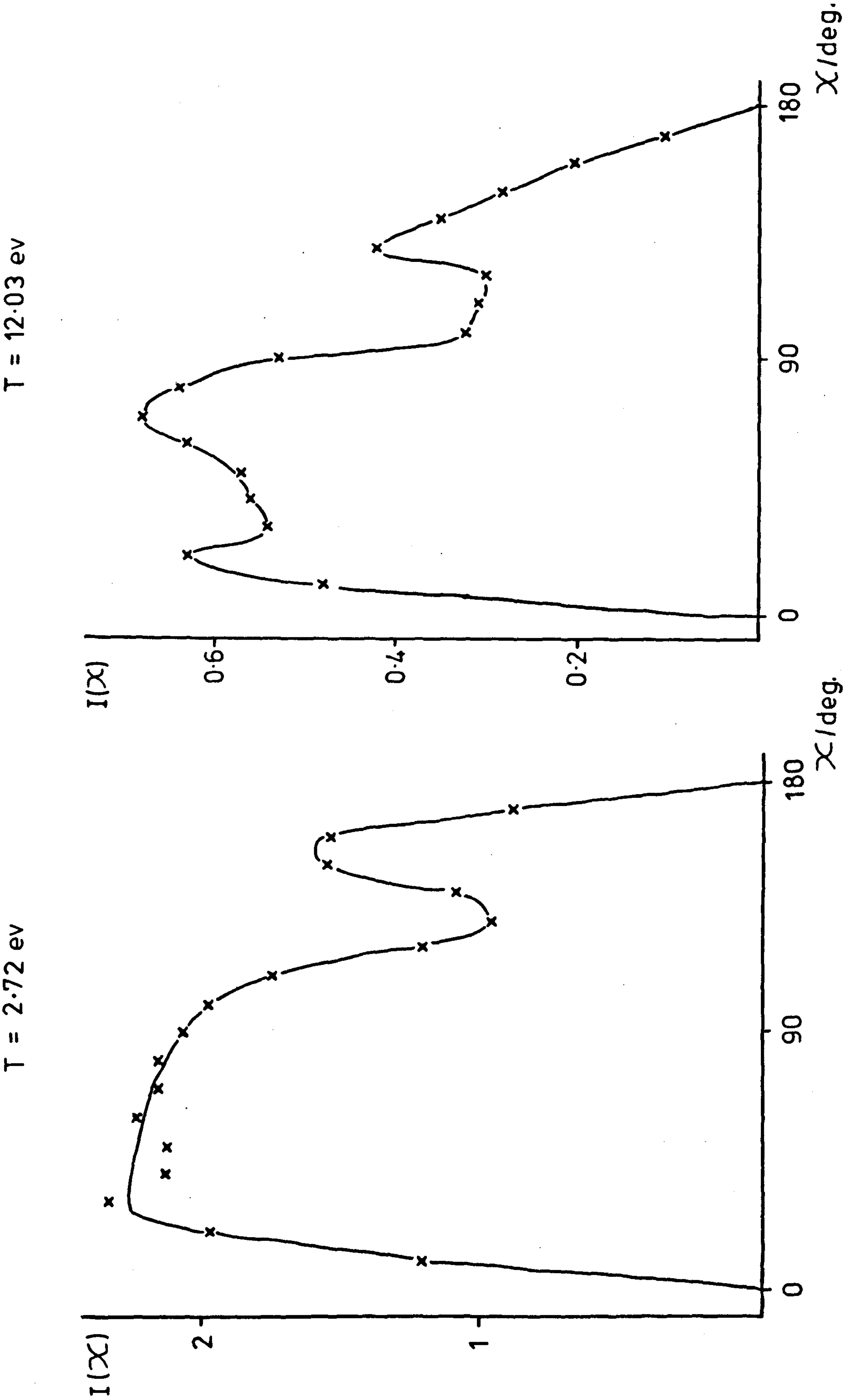

Figure 42. 3D-CM angular distribution of CO_2^+ from $CO^+ + NO$ collisions for initial energies of 2·72 and 12·03 ev.

The contour diagram measured at an initial energy T = 2.72 ev (figure 43) shows a broad forward peak with a maximum at lower CM velocities than predicted by the spectator stripping model and a backward peak which lies outside the elastic stripping circle. This indicates that the backward scattered intensity arises from a mechanism which allows product recoil and leads to a lower internal excitation than the collisions which produce the forward peak.

A plot of the most probable translational exoergicity (Q_{MP}) (derived from the maximum in the cartesian maps) versus initial translational energy (T) for the backward peak (figure 44) gives a straight line. The scatter in the data is due to the large uncertainties which arise in measuring low energy components in the presence of substantial high energy components when an RPD analyser is used. The line deviates from the elastic spectator predictions with the deviation increasing as the initial energy is raised. This indicates that a constant fraction of the relative energy between CO^+ and O , which would go into internal energy of the product CO_2^+ in the elastic spectator model, appears as relative translational energy of the products.

The following simple model for rebound reactive collisions can be used to rationalise these results. Consider the reaction A + BC = AB + C, in which A can be envisaged as approaching BC along the BC axis. As the reactants approach their relative kinetic energy will be

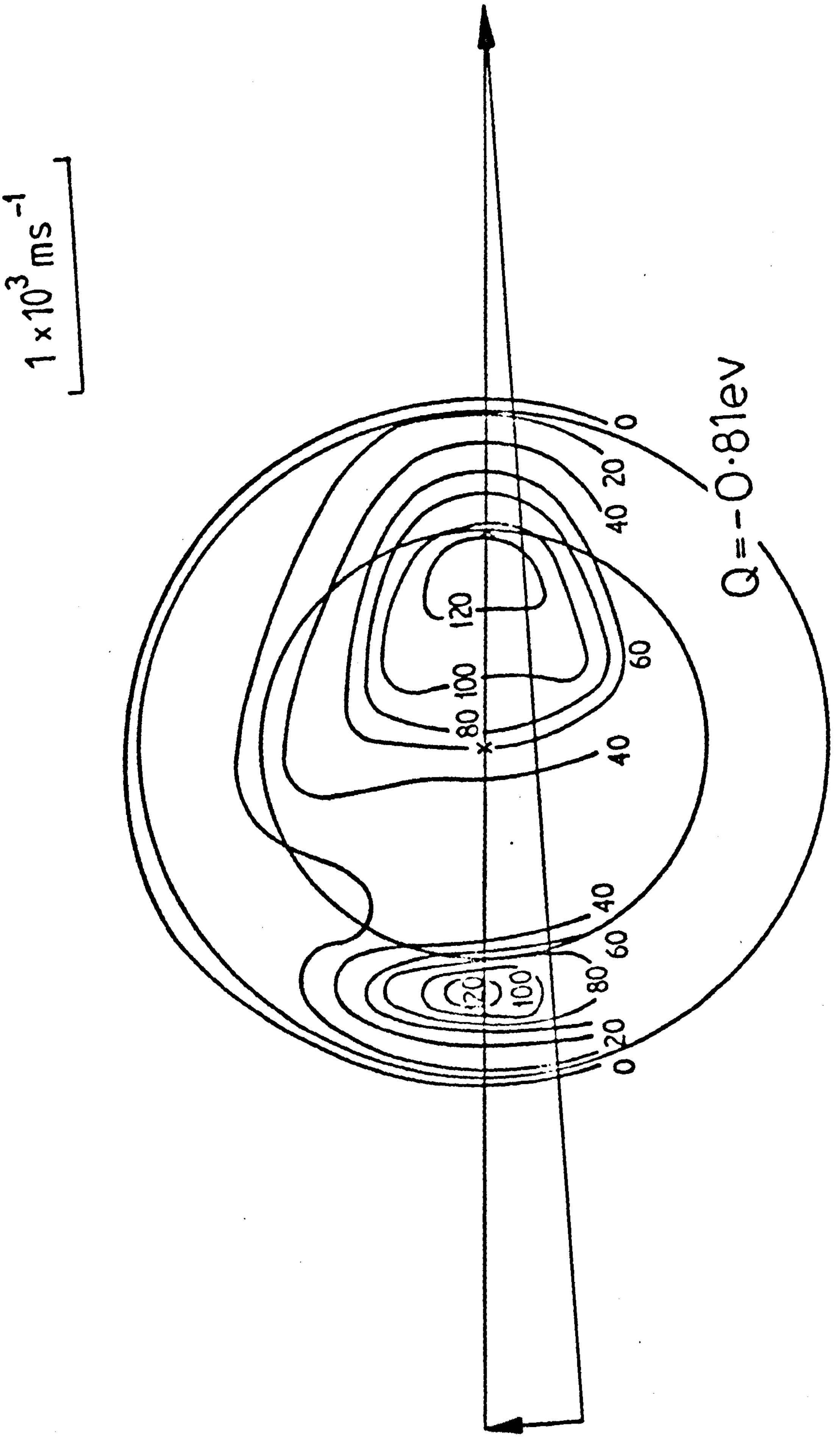

Figure 43. Contour map of intensity of CO_2^+ from $CO^+ + NO$ collisions for initial energy of 2·72 ev.

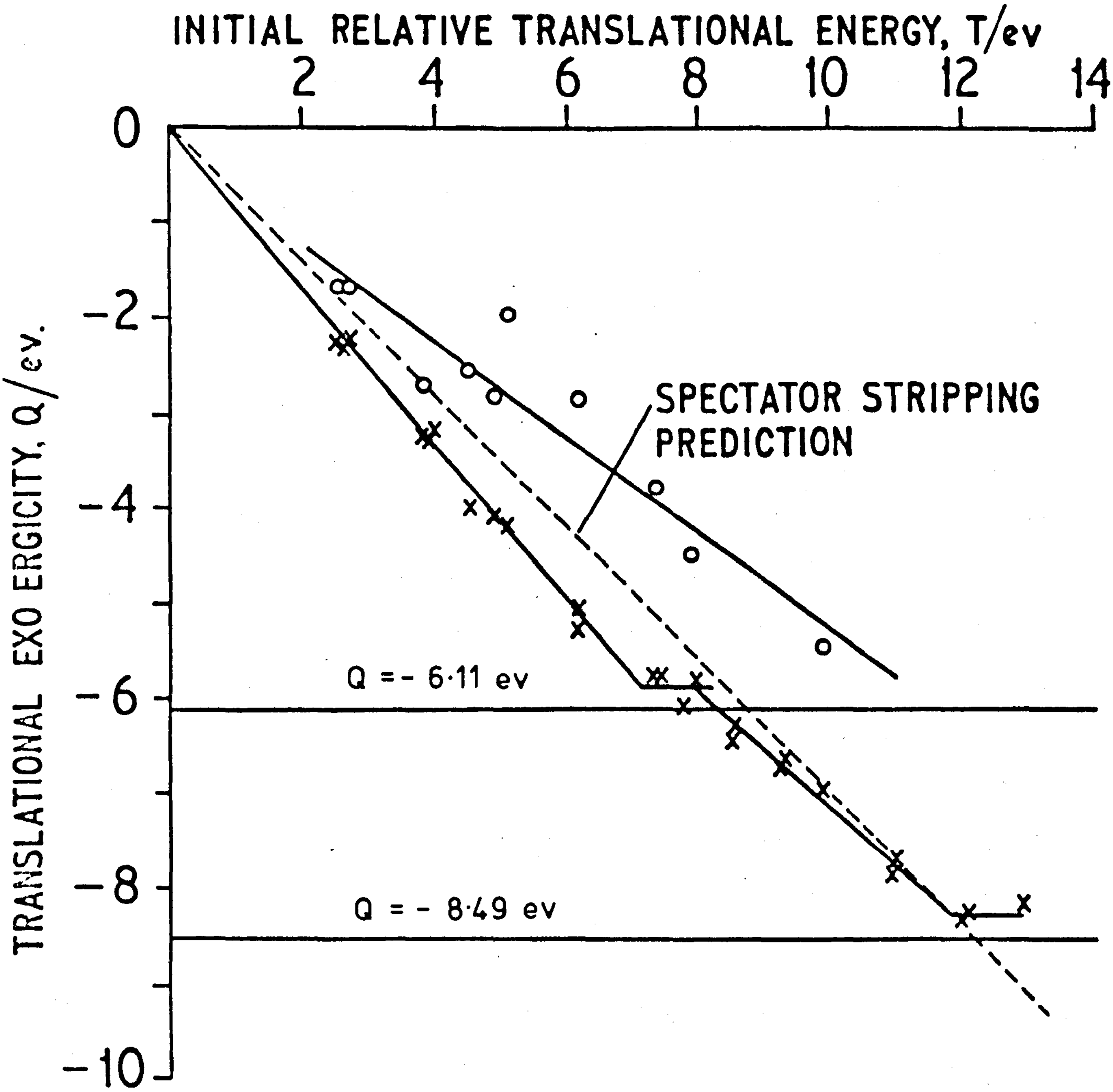

Figure 44. Plot of most probable translational exoergicity (Q_{MP}) versus initial energy (T) for the reaction $CO^+ + NO = CO_2^+ + N$. Crosses are the data for the forward peak and circles are the data for the backward peak.

converted into potential energy as the A-B-C is compressed. At the classical turning point B is considered to be transfered from C to A. The kinetic energy gained as the products recoil will depend on the compression of C against AB. Assuming the potential energy in the AB and BC compressions to be equal and given by 1/2 T, the products will have a final translational energy given by $T' = 1/2\ T$, and thus $Q_{MP}(T) = -0.5\ T$, which is in good agreement with a least squares fit to the data, which yields $Q_{MP}(T) = -0.05\ (\pm 0.34) - 0.538\ (\pm 0.053)\ T$ ev (+ estimated standard deviation). The constant term could be due to a small attractive potential between the products. The fact that close agreement with experimental results is found by neglecting the additional degrees of freedom in the CO^+ ion is significant. Clearly if energy was found to be equilibrated between all the available degrees of freedom this would be consistent with intermediate complex formation. (This could then be related to unimolecular reaction rate theory, where if we naively assume a classical density of states for the oscillators the average translational energy expected is E^* /N, where E^* is the excess energy and N the number of oscillators.) The fact that the additional degrees of freedom in CO^+ are not involved thus appears to be a consequence of the direct nature of the reaction. However it could be argued on simple kinematic grounds that in the collision, while the C - O - N axis must be near linear to produce the required backward scattering, the orientation of the $C\text{-}O^+$ axis with respect to the C - O - N axis can vary over a wide range, and what the measurements actually indicate is that on average there is no energy transfer between the O-C-O bonds in the collision. In fact if the orientation of the $C-O^+$ axis is considered equally likely in all directions in space the most probable collision configuration will be L shaped with the $C-O^+$ axis perpendicular to the C-O-N axis. It seems likely that this would disfavour coupling between the O-C-O bonds. It also seems likely that the vibrational phase of the $C-O^+$ bond will be important in determining the role played by this bond in energy transfer.

This model could also be used to explain the recoil observed in backward scattered CO_2^+ from $CO^+ + O_2$ collisions but unfortunately the scatter in the data is substantially larger for reaction 4.1 than in the data presented here so no accurate comparisons are possible.

Another type of collision process which could produce a backward peak is the ideal knockout process [23]. In this model the CO^+ ion collides impulsively with the nitrogen atom, ejecting it from the NO molecule, and then picks-up the oxygen atom. The model predicts product velocities substantially greater than the elastic spectator model and in excess of those observed in these experiments. This process might be expected to occur with greatest probability when the axis of the neutral species is perpendicular to the collision axis. In view of the highly impulsive nature of this model it seems more likely that in this energy regime trajectories of this type would lead to forward scattering.

The scattering in figure 43 is predominantly forward and the broad forward peak indicates that there is substantial interaction between all atoms in the collisions which lead to forward scattered product.

As the initial energy is raised the forward peak becomes a more dominant feature. Figure 45 shows the contour diagram measured at an initial energy of T = 4.92 ev. The forward peak is now substantially larger than the backward peak and the angular and velocity distributions of the forward peak have become narrower as the initial energy is raised.

These trends may simply be due to the mechanism becoming more impulsive as the initial energy is raised. However they could also be ascribed to the potential energy requirements for an endoergic process, which requires a small impact parameter for translational energy to be effective in overcoming the potential barrier to reaction. As the initial translational energy is increased larger impact parameter collisions can become effective in overcoming the barrier. Since presumably collisions with larger impact parameters occur with less interaction between all four atoms the forward peak would be expected to become both larger and narrower as the initial energy is raised.

These trends continue as the initial energy is raised. However the contour diagram measured at an initial energy T = 6.21 ev (figure 46) shows that product stability restrictions have started to operate and narrow the velocity distribution of the forward peak by "eating away" intensity.

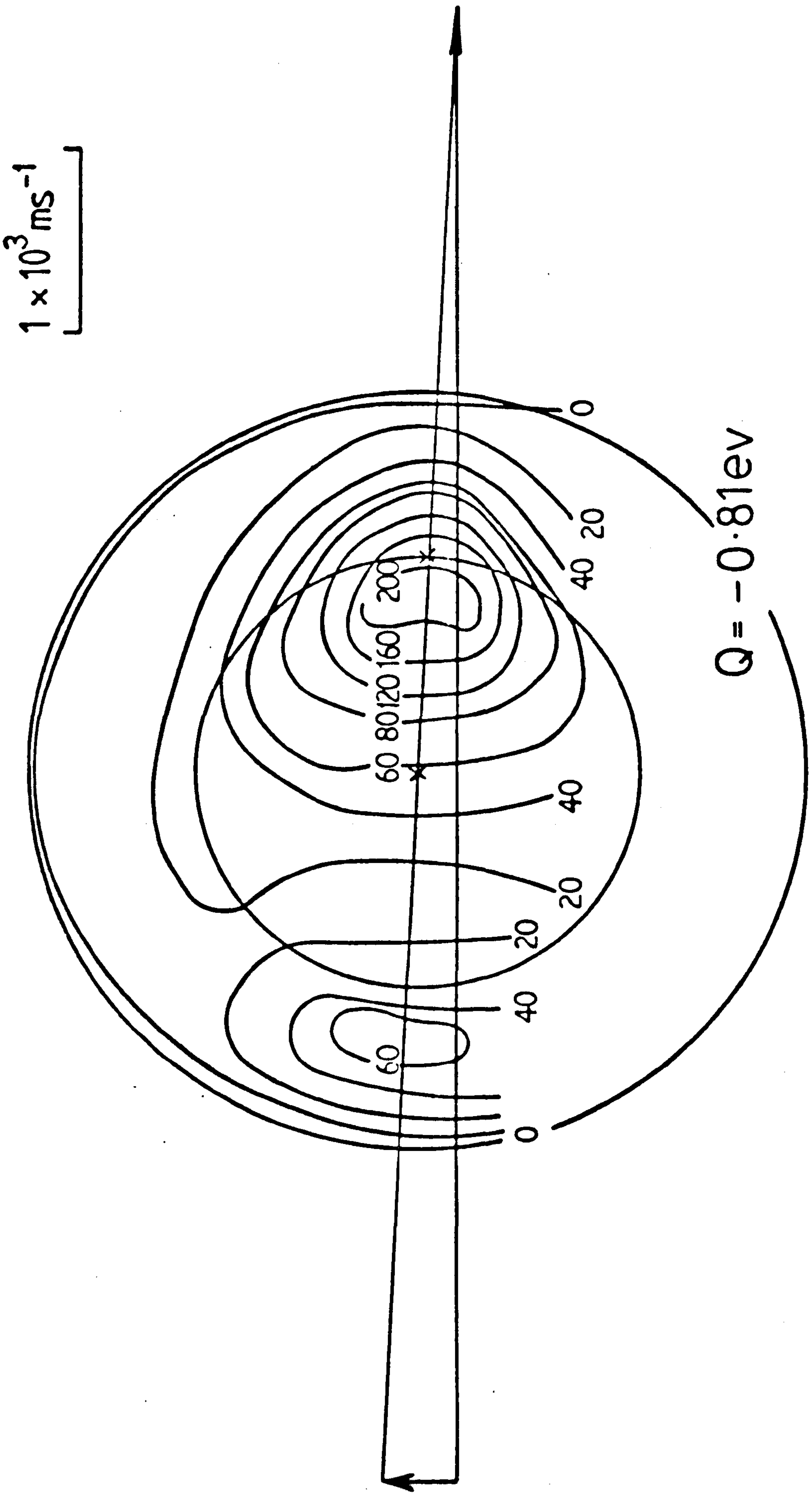

Figure 45. Contour map of intensity of CO_2^+ from CO^+ + NO collisions for initial energy of 4·92 ev.

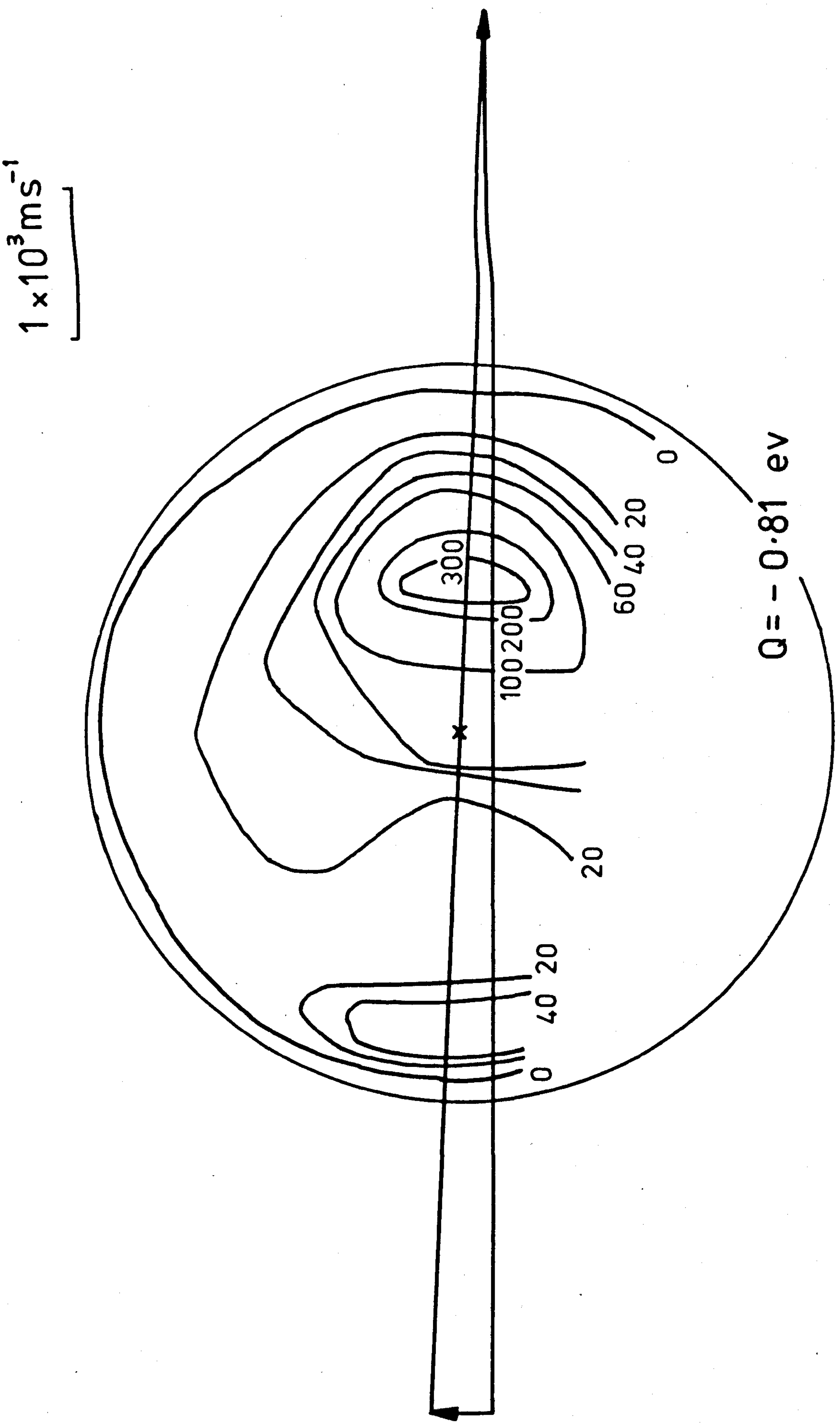

Figure 46. Contour map of intensity of CO_2^+ from $CO^+ + NO$ collisions for initial energy of 6·21 ev.

The contour diagram measured at an initial energy T = 7.91 ev (figure 48) also clearly shows this effect. The total cross section (figure 41) declines in this energy regime.

In the lower energy range where the reaction dynamics are not strongly influenced by product stability restrictions a plot of the most probable translational exoergicity (Q_{MP}) against the initial relative energy (T) (figure 44) is a straight line. The internal excitation increases more rapidly than predicted by the spectator stripping model, indicating the conversion of a constant fraction of the kinetic energy of the spectator into internal energy of the product. Similar behaviour was found in the data for reaction 4.1, although significantly larger deviations from spectator stripping predictions are found in the data presented here. There appears to be no simple kinematic rationale for these results. The origins of these trends presumably lies in the details of the potential hypersurfaces. However some qualitative conclusions can be drawn. These results indicate close coupling of the motion of the atoms in the collision and possible mechanisms by which this could be envisaged as occuring were suggested in the previous chapter. Since the deviation from spectator stripping predictions is smaller in the data presented here it seems likely that reaction 5.1 occurs on a potential surface on which the atoms are less closely coupled than for reaction 4.1.

It should be noted, that as discussed previously, in the data presented here the most probable translational exoergicities are simply derived from the maxima in the LAB energy distributions.

Figure 47 shows the product translational energy distributions, $P(T')$, at $T = 2.72$ and 6.21 ev, derived by integration of the intensity on the contour diagrams. The most probable product translational energy occurs at substantially lower translational energies than predicted by the simple spectator stripping model.

In the higher energy regime the reaction dynamics are strongly influenced by product stability restrictions and the total cross section declines sharply. The contour diagram measured at an initial energy $T = 7.91$ ev (figure 48) shows a forward peak just inside the $Q = -6.11$ ev stability limit. In addition there is a low intensity backward peak from low impact parameter collisions. There is a clear dissociation threshold at the $Q = -6.11$ ev stability limit. In addition there is an inflection in the Q_{MP} vs T plot (figure 44) at this initial energy. The deviation of the data from the $Q = -6.11$ ev line in the plot arises from the finite resolution of the experiment. An analysis of this indicates that it is unreasonable to suggest that the data is displaced from the $Q = -6.49$ ev threshold. This suggests (assuming ground state reactants) the possibility that most of the CO_2^+ formed in the higher vibrational levels of the $X\,^2\Pi_g$ state which correlates adiabatically with $CO^+(X\,^2\Sigma^+)$ + $O(^3P)$ undergoes a spin forbidden predissociation, before reaching the detector, via a repulsive $^4\Sigma$ state, which correlates with $O^+(^4S)$ + $CO(X\,^1\Sigma^+)$. Similar results were

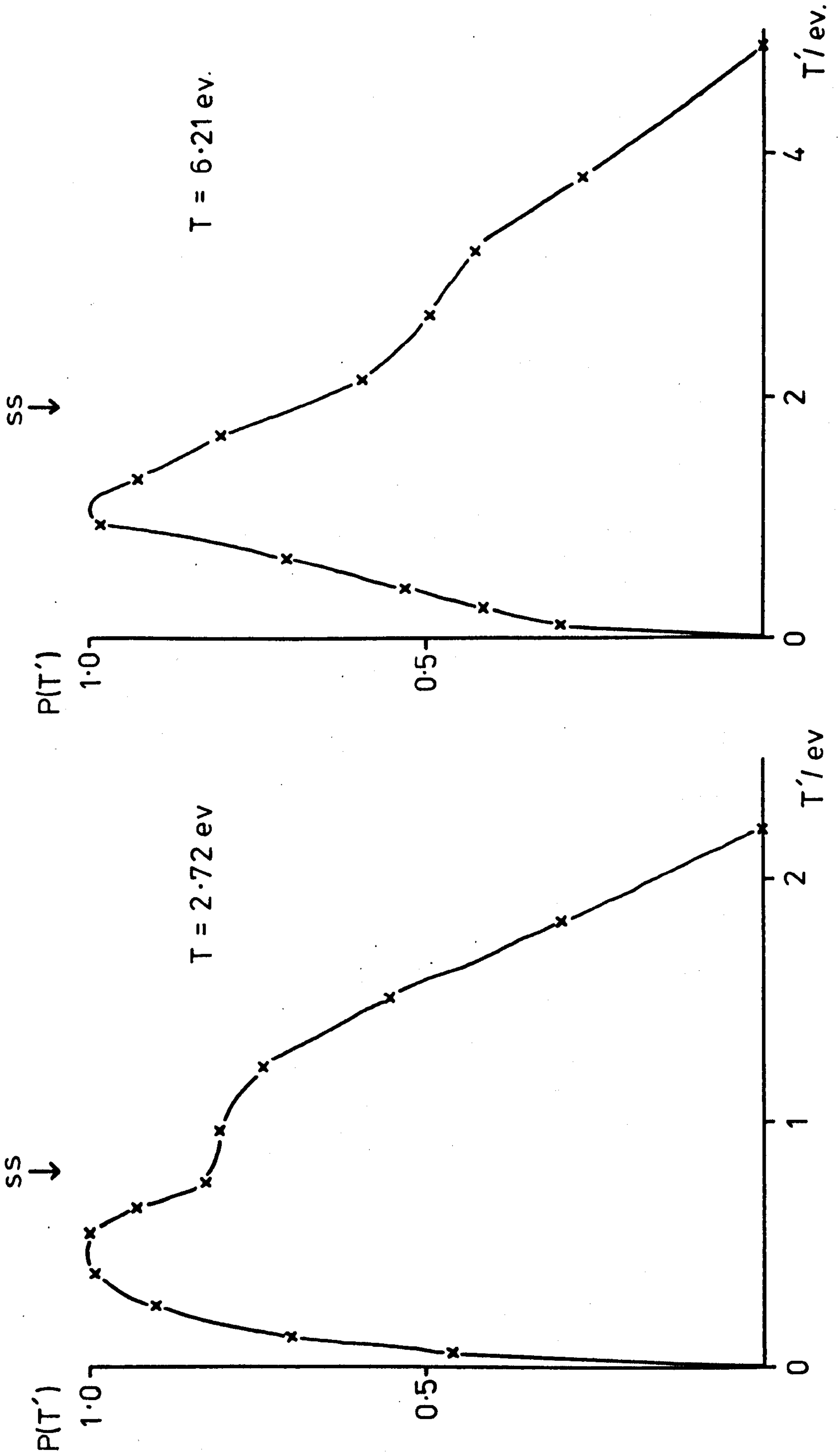

Figure 47. Product translational energy distribution, P(T′), of the reaction $CO^+ + NO = CO_2^+ + N$ for initial energies of 2·72 and 6·21 ev.

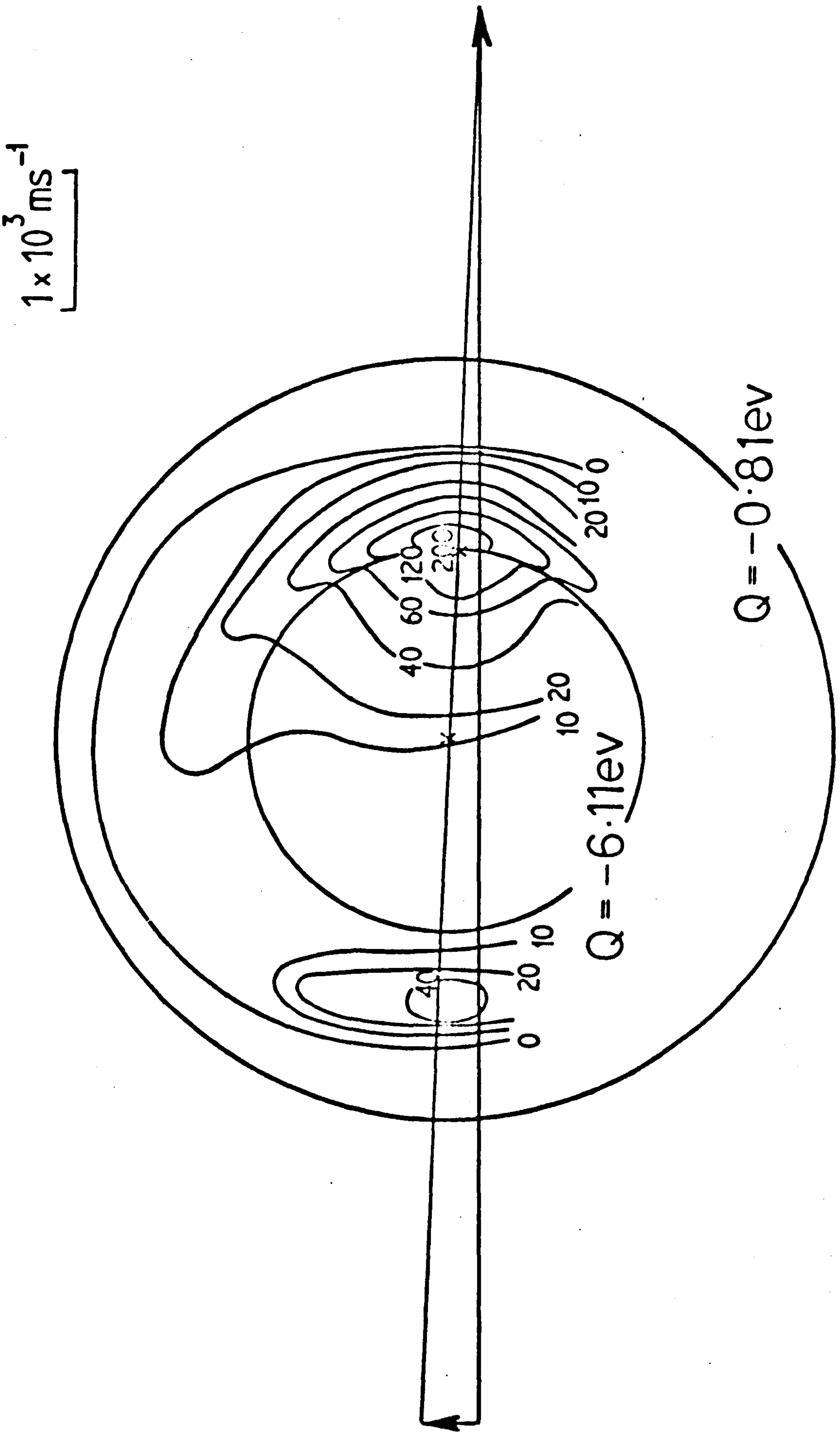

Figure 48. Contour map of intensity of CO_2^+ from CO^+ + NO collisions for initial energy of 7·91 ev.

found in chapter 4. Figure 49 shows a portion of tha cartesian velocity spectrum derived from the LAB measurement at 2.5° at this initial energy. This shows a feature which is not clear in the full contour diagram. There is a shoulder at lower velocities than the peak approximately corresponding to $Q = -6.49$ ev. This presumably arises from product that has not predissociated before reaching the detector. The smaller shoulder at lower velocities arises from electronically excited product.

The substantial intensity inside the $Q = -6.11$ ev circle indicates that either the CO_2^+ or N (or both) are formed in an electronically excited state. Although it is not possible to say unambiguously from the beam data alone which of the products is excited, the data is consistent with the assumption that the major excited product is $N(^2D)$ and that CO_2^+ is not formed in an electronically excited state to any extent. The limits for Q are then $-3.19 > Q > -8.49$ ev for the formation of $CO_2^+(X^2\Pi_g) + N(^2D)$, assuming the CO_2^+ dissociates into the lowest energy fragments $O^+(^4S) + CO(X^1\Sigma^+)$. The observation that the excited state dissociation threshold for $CO_2^+ + O$ and $CO_2^+ + N$ are consistent with the formation of excited neutral with different excitation energies provides additional circumstantial evidence that a single excited state of CO_2^+ is not involved.

The contour diagram measured at an inital energy $T = 9.86$ ev (figure 50) shows that the intensity has contracted so that virtually none lies outside the $Q = -3.19$ ev

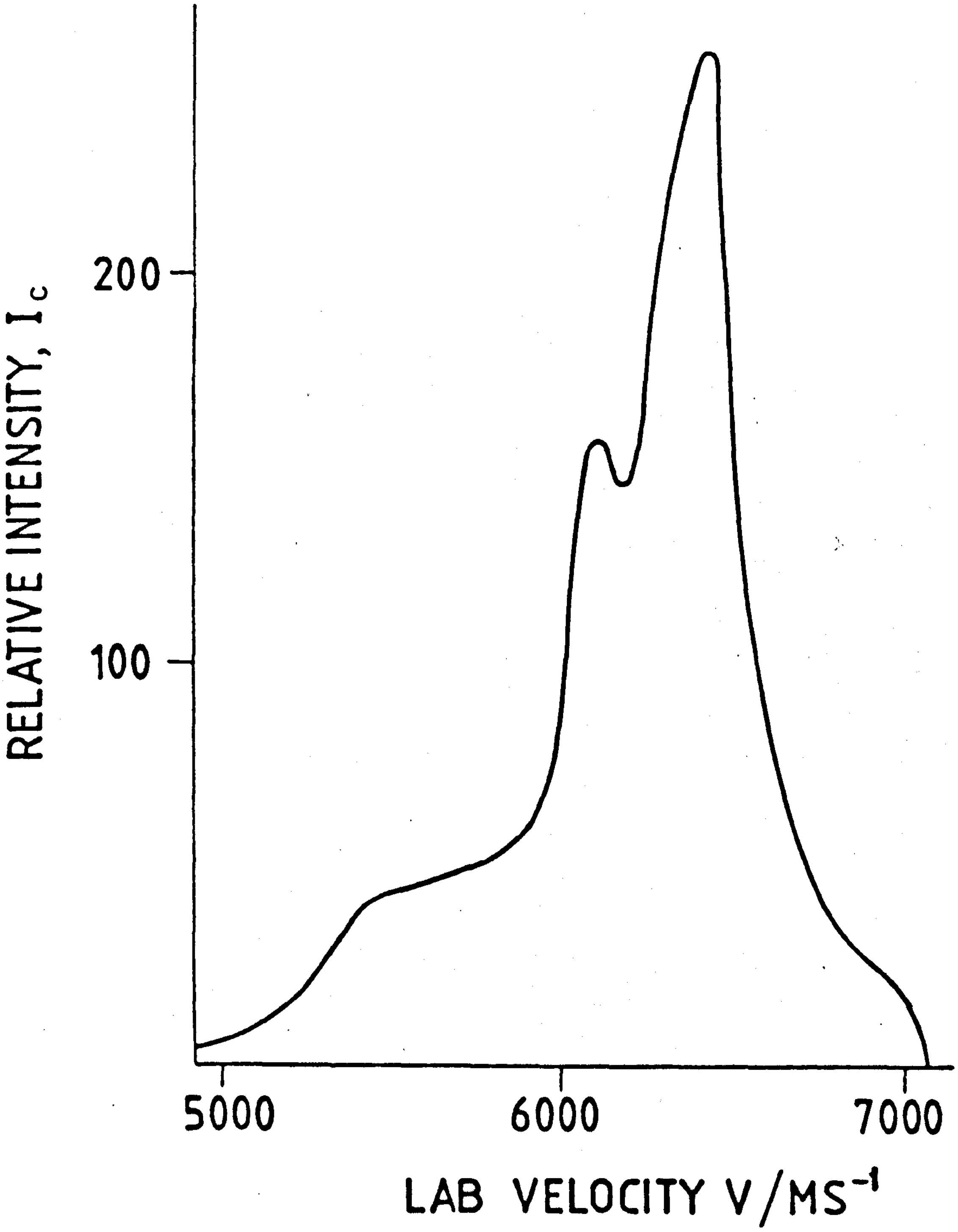

Figure 49. A portion of the cartesian velocity spectrum measured at 2·5°(LAB) for initial energy of 7·91 ev.

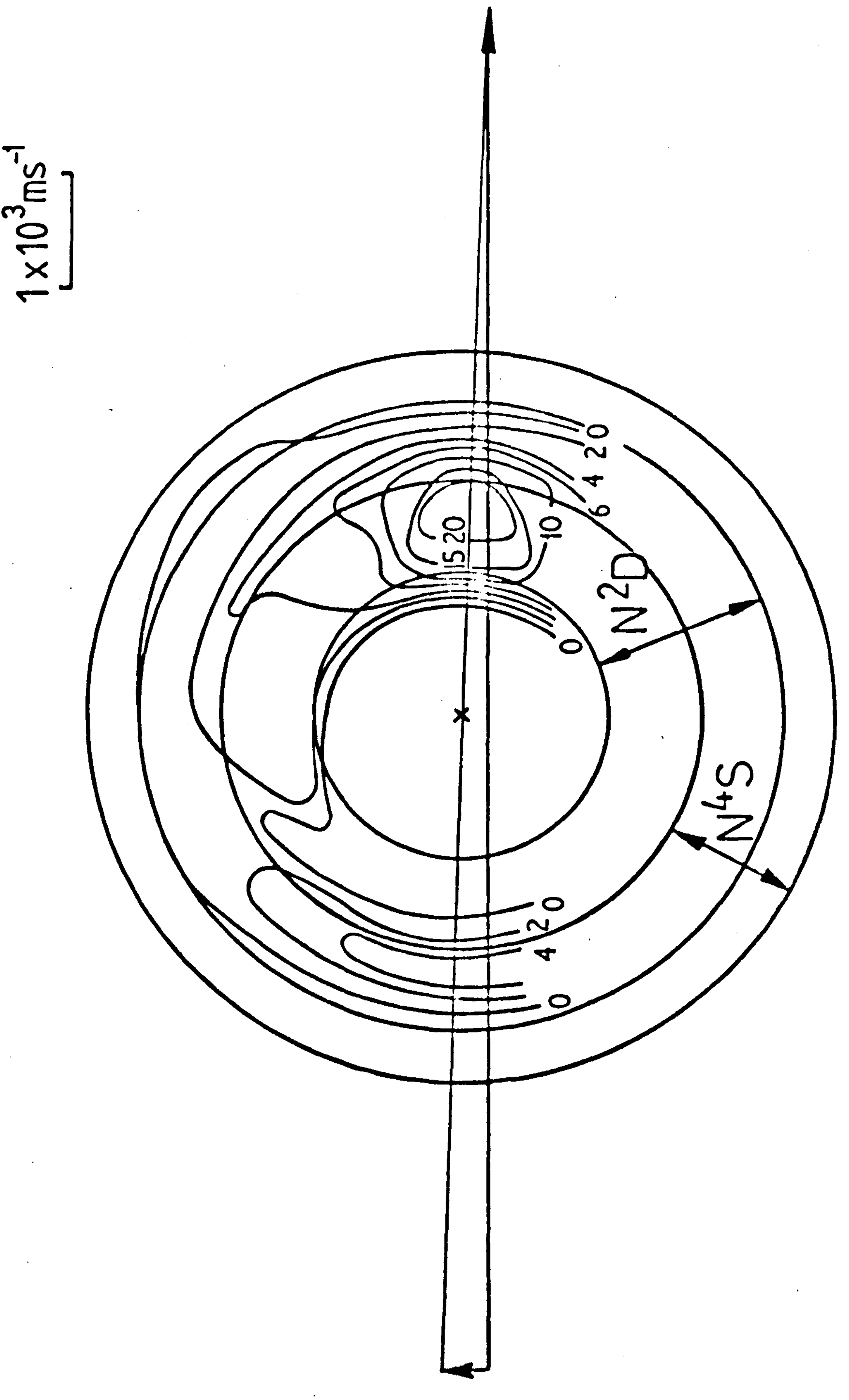

Figure 50. Contour map of intensity of CO_2^+ from $CO^+ + NO$ collisions for initial energy of 9·86 ev.

stability limit. The forward peak now lies outside the stability zone for ground state product formation. The loss of the ground state forward peak due to product stability restrictions indicates that the ground state potential hypersurface has no features which permit forward recoil of products. In contrast the forward peak was retained in the exothermic reaction 4.1, having shifted to higher velocities. This is consistent with the view that the features of the potential hypersurface connected with forward product recoil are related to reaction exoergicity.

The backward peak lies inside the stability zone for ground state product. In view of the product recoil observed in rebound scattered product at lower energies it seems reasonable to conclude that this peak represents ground state product stabilised by the recoil mechanism discussed previously. However, in view of the backward scattered intensities observed at lower energies it is somewhat surprising that there is not substantially more backward scattered intensity at this energy. Three dimensional integrations of the contour diagrams to obtain σ_F (χ = 0-140°) and σ_B (χ= 140-180°), the partial cross sections for forward and backward scattering (figure 51) show that there is a reduction is backward scattering as the initial energy is raised above 6 ev, although the ratio of backward to forward scattering declines as the energy is raised from 2.72 to 6.21 ev and then remains approximately constant as the energy is further raised. In view of the close coupling of the motion of the atoms in the proposed rebound mechanism the loss of backward scattered intensity would be predicted

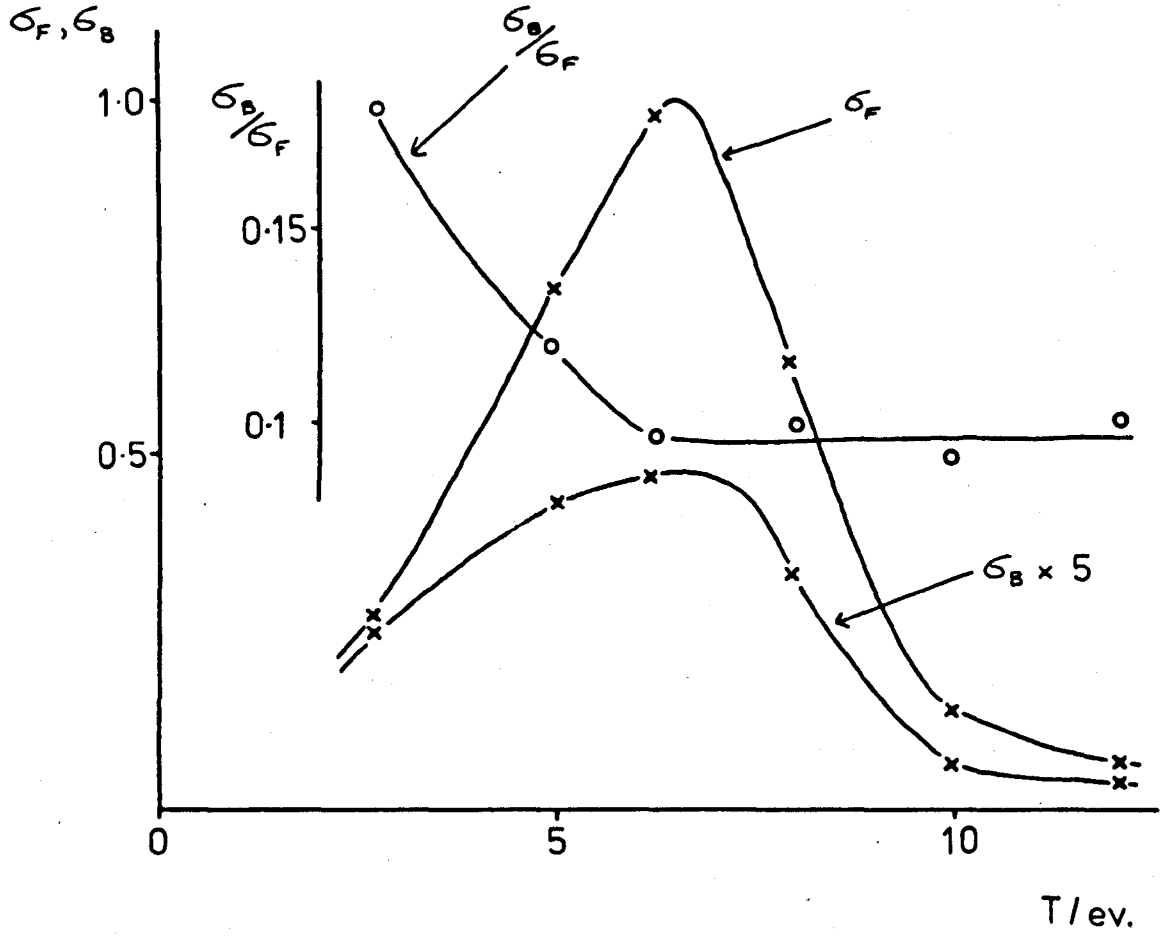

Figure 51. Plot of partial relative cross sections, σ_F ($\chi = 0 - 140^\circ$) and σ_B ($\chi = 140 - 180^\circ$), for forward and backward scattering versus initial energy, T, for the reaction $CO^+ + NO = CO_2^+ + N$

at high initial energies as the collision becomes more impulsive.

There is a small intensity ridge just inside the ground state stability zone in figure 50 at centre of mass scattering angle $\chi \simeq$ 20-50° which is presumably due to ground state product from collisions in which all atoms strongly interact. A dissociation threshold is evident around Q = -8.49 ev. As discussed previously this is tentatively assigned to the spin forbidden predissociation of CO_2^+ formed in the reaction

$$CO^+(X\,^2\Sigma^+) + NO(^2\Pi) = CO_2^+(X\,^2\Pi_g) + N(^2D) \qquad 5.2$$

Intensity inside the circle Q = -8.49 ev could arise from the finite resolution of the instrument.

A plot of Q_{MP} vs T (figure 44) in this energy range indicates that the most probable translational exoergicity tends towards spectator stripping predictions in this high energy regime. Although no particular significance can be attached to this concerning the operation of a stripping mechanism, since a number of conceptually different mechanisms have been shown to predict product velocities close to the spectator stripping predictions, it is unlikely that the ideal stripping mechanism is operative in this case since the product velocity distributions are broad. It is interesting that at lower energies there is substantial evidence for the coupling of the motion of all four atoms in the collision, whereas at higher energies as interaction times fall the spectator stripping predictions are approached. Reaction 5.2 is 3.19 ev endoergic and it is somewhat surprising that the marked endoergicity of the reaction does not have a more marked effect on the reaction dynamics. The effects of a barrier to reaction due to reaction endoergicity on the dynamics are discussed in detail in the following chapter.

The product translational energy distributions in this energy range (figure 52), derived by integration of the intensity on the contour diagrams, show that as the initial energy is raised an increasing proportion of the product is electronically excited. The most probable product translational energy over this higher energy range occurs at $Q > -6.11$ ev, showing that substantial components of the product are still formed in the ground electronic state even at $T = 12.03$ ev, although at this energy the $P(T')$ distribution is bimodal and it is likely that more than 50% of the product is electronically excited. A substantially larger proportion of the products from CO^+ + NO collisions is electronically excited than from $CO^+ + O_2$ collisions.

As the initial energy is further raised the total cross section declines due to product stability restrictions as intensity is further "eaten away". Figure 53 shows the contour diagram measured at an initial energy $T = 12.03$ ev, the highest energy at which a full contour diagram was measured. The forward peak lies just inside the stability zone for formation of $CO_2^+(X^2\Pi_g) + N(^2D)$. The backward peak now lies outside the ground state product stability zone. At this energy it is not possible to form ground state backward

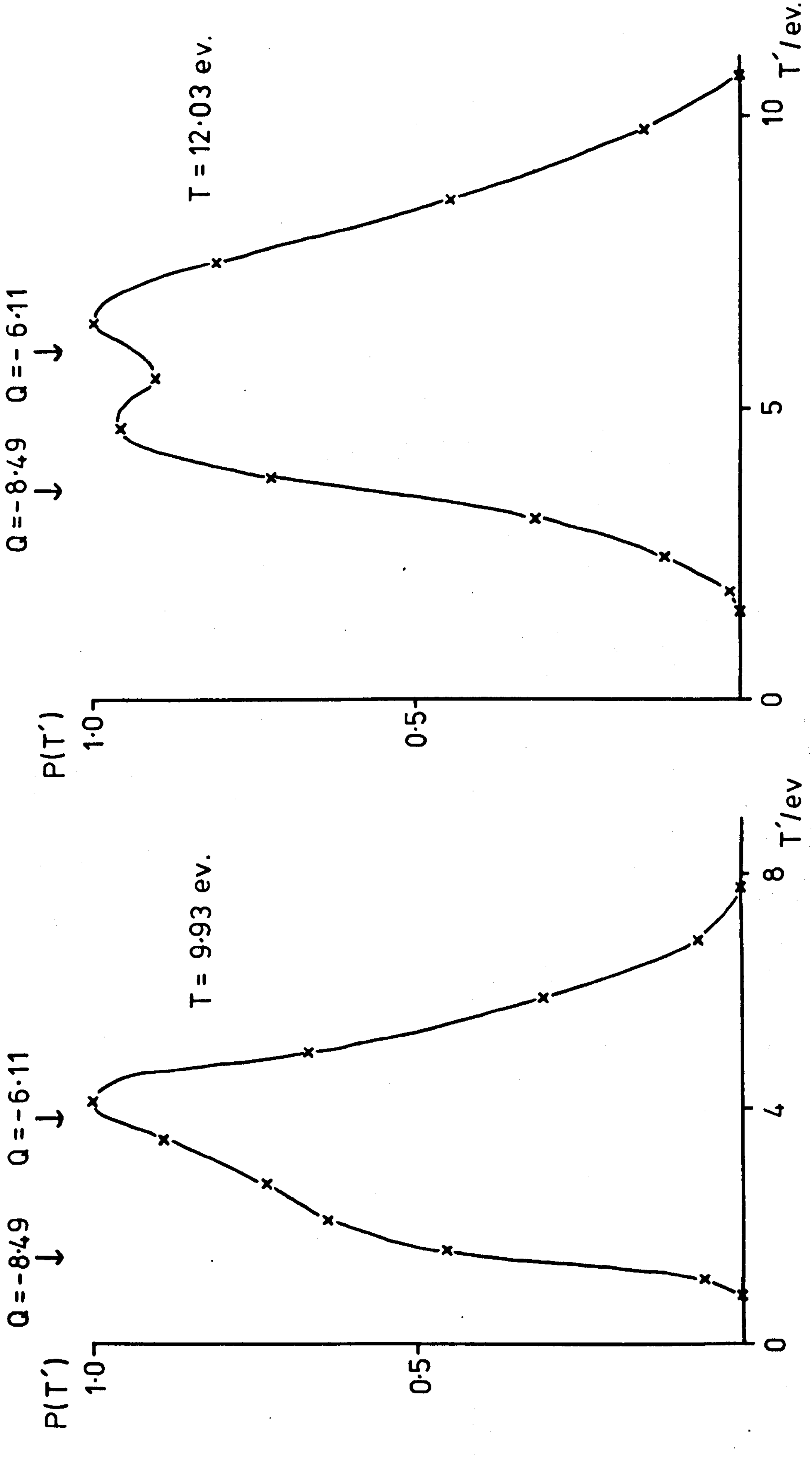

Figure 52. Product translational energy distribution, P(T′), of the reaction $CO^{+} + NO = CO_2^{+} + N$ for initial energies of 9·93 and 12·03 ev.

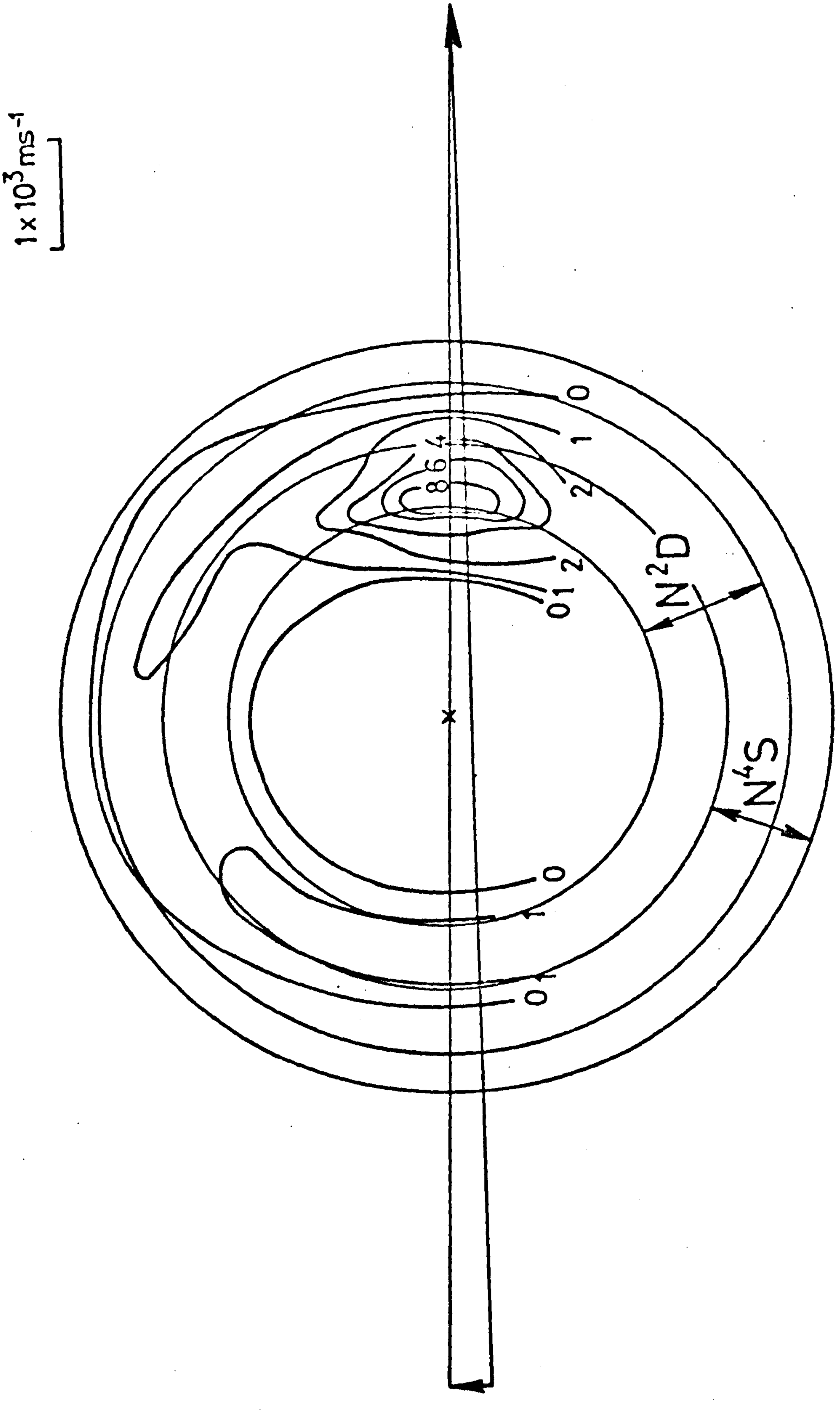

Figure 53. Contour map of intensity of CO_2^+ from $CO^+ + NO$ collisions for initial energy of 12·03 ev.

scattered product by the mechanism discussed above. No significant intensity lies outside the Q = -3.19 ev circle except at $\chi \simeq 50°$. There is also an intensity ridge along the ground state product stability circle at this CM scattering angle, which is presumably due to ground state product. It seems likely that this wide angle ground state product arises from collisions in which all atoms strongly interact enabling substantial transfer of momentum to occur in a manner similar to the sequential impulse model. Although a dissociation threshold is evident around Q = -8.49 ev there is substantial intensity inside the Q = -8.49 ev circle, particularly at 0°, where significantly more intensity occurs inside the forbidden zone than would be expected from consideration of experimental resolution. This could arise from a number of different sources - formation of some highly rotationally excited CO_2^+ with a substantial centrifugal barrier to dissociation, the formation of a small component of the product $CO_2^+ + N$ in a more highly electronically excited state, or possibly CO_2^+ which does not predissociate before reaching the detector. (It was not possible to resolve this contribution as above because of the lower resolution in the CM system at this initial energy and because of the reduced S/N ratio of the data due to lower product ion intensities.) The Q_{MP} vs T plot (figure 44) shows a second inflection at this initial energy, as the forward peak is again eaten away by product stability restrictions.

CHAPTER 6.

The reaction $CO^+ + NO = (NCO)^+ + O$.

6.1 Introduction.

In chapter 5 the observation of the atom transfer product $(NCO)^+$ from CO^+ and NO collisions was reported. In this chapter the results of a study of the dynamics of the reaction

$$CO^+ + NO = (NCO)^+ + O \qquad 6.1$$

are reported and discussed. The microscopic molecular dynamics of reaction 6.1 are potentially very complicated since there possibly exist three stable isomers of the ion $(NCO)^+$ and the neutral product O could conceivably be derived from CO^+ as well as NO.

It appears that no experimental properties of $(NCO)^+$ are known except for its existence in the ICR spectrum of Nitromethane [89]. A limited <u>ab initio</u> SCF-CI theoretical investigation of the ion has been performed by Wu and Schlier [3]. They found that all three isomers were stable and probably have linear $^3\Sigma^-$ ground states. The SCF stability was found to have the order $NCO^+ > NOC^+ > CNO^+$. CI calculations were performed only for the most stable isomer NCO^+, for which the adiabatic dissociation energy was calculated to be 3.81 ev relative to $N + CO^+$. This value would make reaction 6.1 2.70 ev endothermic.

6.2 Results and discussion.

Product intensity contour diagrams for reaction 6.1 have been measured over the initial relative energy range 3.5 to 10 ev. In addition a limited number of experiments were performed in which the product energy distribution was measured only at the maximum in the LAB angular distribution to determine the most probable translational exoergicity, Q_{MP}.

Since no previous measurements of the total cross section for reaction 6.1 have been reported the relative cross sections have been derived from the contour diagrams. Figure 54 shows a plot of the relative cross section (σ_R) versus the initial translational energy (T). Also shown in figure 1 are the relative cross sections for the competing reaction (5.1) plotted on the same scale for comparison. Because of the difficulty in measuring absolute product and reactant fluxes in a crossed beam instrument absolute values have not been assigned to these measurements, and the relative values are probabably only accurate within a factor of 2-3.

Figure 54 shows that at low energy the CO_2^+ product predominates. However, as the initial energy is raised the total cross section for the formation of $(NCO)^+$ rises from a threshold (apparently at approximately 2.7 ev) to a broad peak at around 8 ev. The total cross section for CO_2^+ formation rises to a peak at around 6 ev and then declines

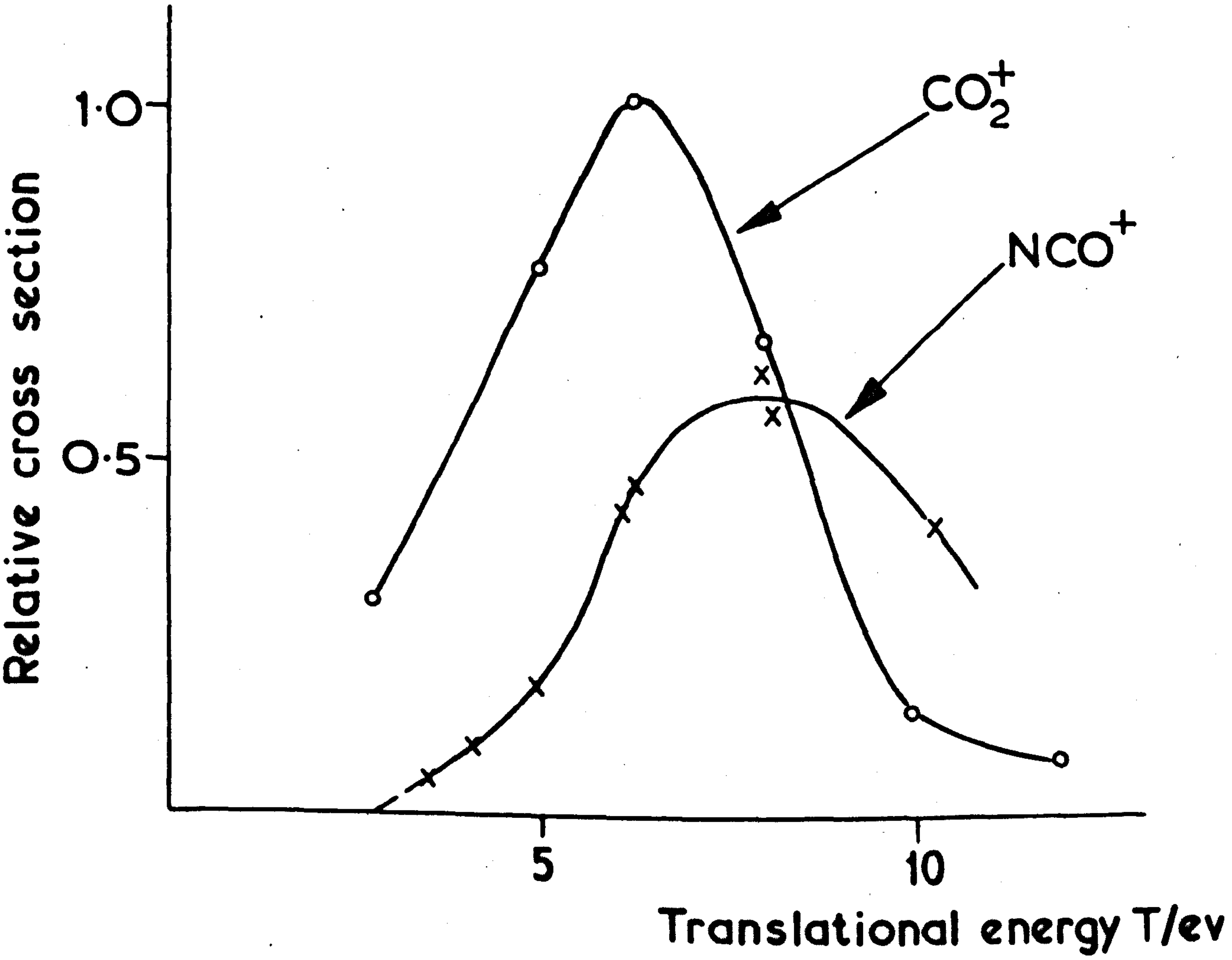

Figure 54. Plot of relative cross sections, σ_R, (obtained from the contour diagrams) versus initial energy, T, for CO_2^+ and $(NCO)^+$ formation from $CO^+ + NO$ collisions.

sharply as product stability restrictions dominate the dynamics. At high energy the $(NCO)^+$ product predominates.

For reaction 6.1, assuming that the products are the most stable isomer NCO^+ and O in their ground electronic states and that the reactants are in their ground electronic and vibrational states, the translational exoergicity, Q, (as defined on page 73) has the limits $-2.70 > Q > -6.51$ ev for adiabatic dissociation of the NCO^+ isomer into the fragments N + CO^+. For the less stable isomers, NOC^+ and CNO^+, it is not possible to estimate the Q stability limits with such precision. According to Wu and Schlier [3] the $^3\Sigma^-$ ground state of the NOC isomer dissociates adiabatically to N + CO^+ and the $^5\Sigma^-$ ground state of the CNO^+ isomer dissociates adiabatically to the lowest energy fragments C + NO^+ (for which $Q > -6.36$ ev). Since these isomers appear to be less stable than NCO^+ the upper stability limits will be less than for NCO^+. Thus it is likely that the Q stability limits for the NOC^+ and CNO^+ isomers will lie within those defined for the NCO^+ isomer.

Figures 56, 58, 59, 61, and 62 show the $(NCO)^+$ product intensity contour diagrams at relative energies 3.53, 5.01, 6.13, 7.93, and 10.22 ev. All the contour diagrams are asymmetric with respect to the ±90° axis, indicating that the reaction proceeds by a direct mechanism over the whole energy range studied, although there is evidence for the coupling of the motion of all atoms in the collision. The 3D-CM angular distributions, derived by integration of the intensity on the contour diagrams, show that at low energy the product $(NCO)^+$ is mainly forward scattered but with substantial backward scattering (figure 55). As the initial energy is raised above 6 ev there is an increase in backward scattering and a shift to mainly backward scattered product at high energy (figure 55). The shift from mainly forward to mainly backward scattering presumably arises at least partly from product stability restrictions. In contrast CO_2^+ product was found to be predominantly forward scattered over the energy range 2.5 - 12 ev, with the degree of forward scattering initially increasing as the energy is raised and then remaining approximately constant as the total cross section declines sharply due to restrictions on product stability. This makes it attractive to speculate that CO_2^+ is derived mainly from larger impact parameter grazing collisions and that $(NCO)^+$ is derived from lower impact parameter collisions in which all atoms strongly interact. Such behaviour might be expected from consideration of the potential energy requirements for an endoergic reaction. However trajectory calculations [35] show that care is required in interpreting forward scattering as arising from grazing collisions alone since low impact parameter collisions in which all atoms strongly interact can lead to strongly forward peaked scattering. Model calculations [36,90] suggest that the focussing effect of the ion-induced dipole potential as the products separate is an important factor in producing the predominantly forward scattering often observed in the dynamics of ion-molecule reactions.

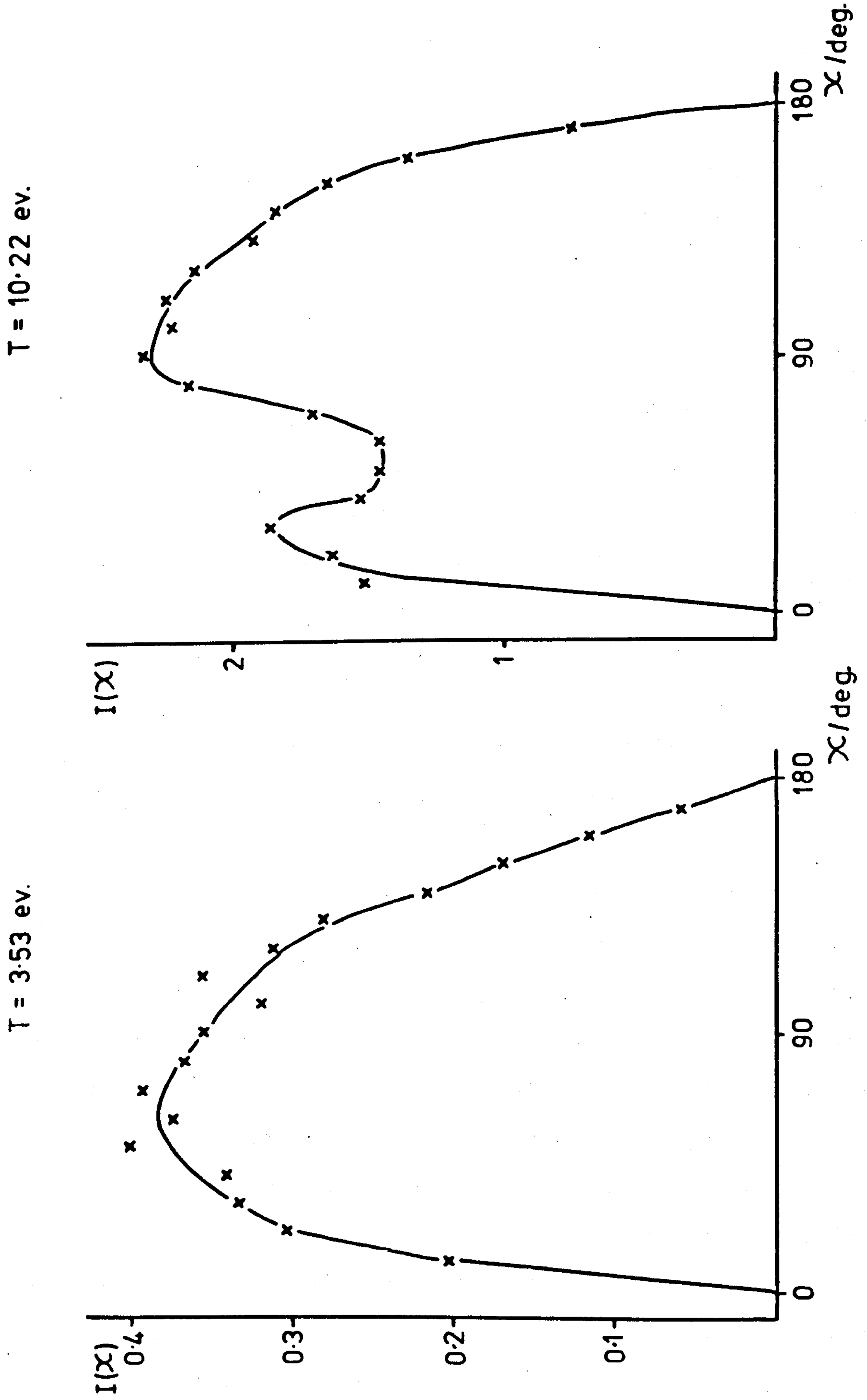

Figure 55. 3D-CM angular distribution of $(NCO)^+$ from $CO^+ + NO$ collisions for initial energies of 3·53 and 10·22 ev.

Figure 56 shows the intensity contour diagram measured at an initial energy T = 3.53 ev. It can be seen that the intensities are very low and long accumulation times (upto 24 hours) were required to measure these data. Despite this it is difficult to define the zero contour with precision because of low intensity tails in the energy distributions. It is however clear that substantial intensity lies outside the Q = -2.70 ev circle. The product translational energy distribution, P(T'), (figure 57), derived by integration of the intensity on the contour diagram, shows that in excess of 40% of the intensity lies outside the -2.70 ev circle. This is particularly evident in the forward direction where the zero contour deviates by in excess of 1.4 ev from the -2.70 ev circle. It seems unlikely that the CI calculations from which the value of -2.70 ev was derived should be in error by this much. It is more likely that intensity outside the circle arises predominantly from the reaction of electronically or vibrationally excited CO^+ in the beam. Although the CO^+ is predominantly in the ground electronic state (probably $\simeq$ 2% in excited states) there is significant vibrational excitation. Moran et al [80] have calculated the vibrational state distribution for a range of impacting electron energies. Their calculations show that at 30 ev, although the v=0 state is predominantly populated (approximately 70%) vibrational levels upto v=5, corresponding to a vibrational excitation of 1.32 ev, show a relative population greater than 1%.

Thus it seems probable that at this energy a substantial fraction (>40%) of the product is derived from

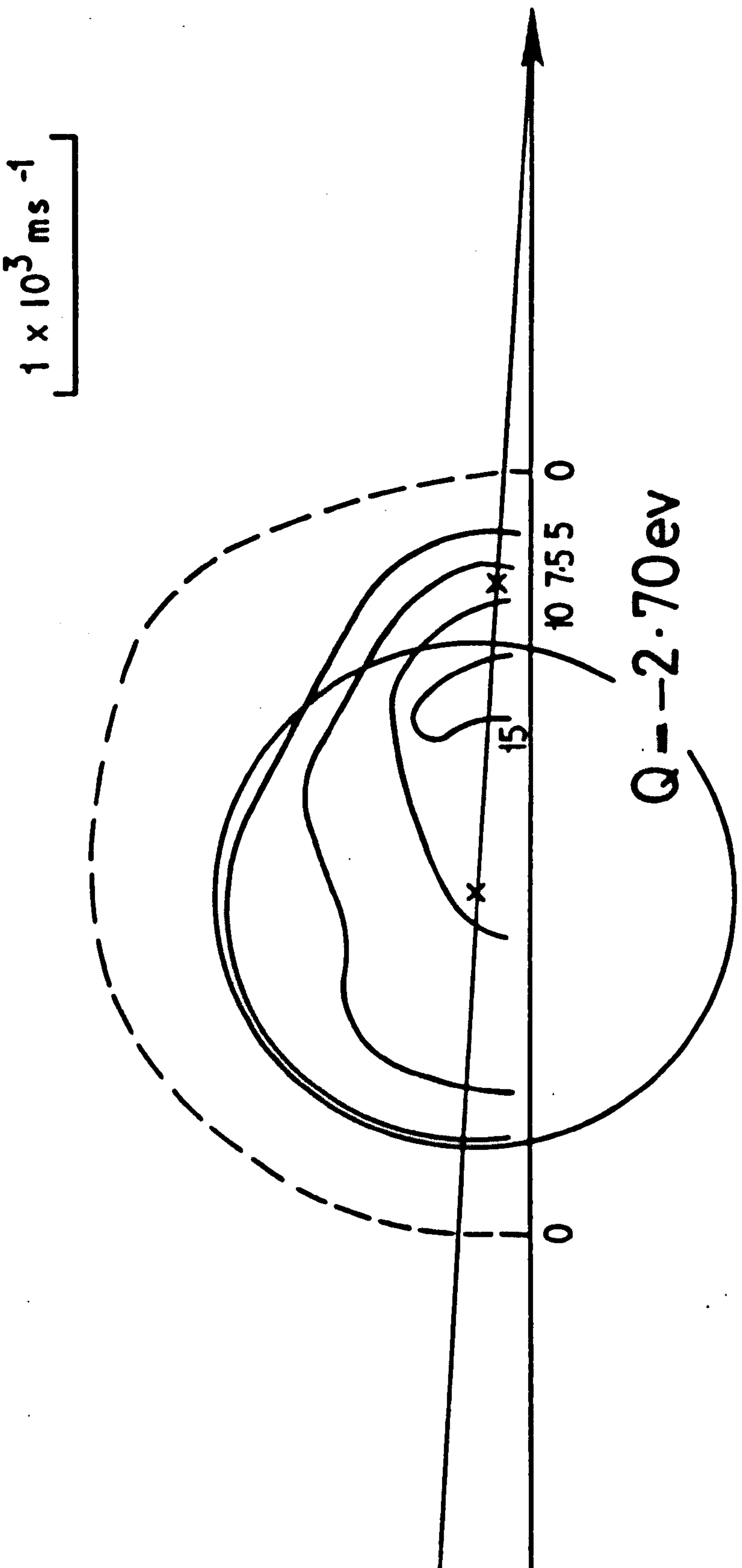

Figure 56. Contour map of intensity of $(NCO)^+$ from $CO^+ + NO$ collisions for initial energy of 3·53 ev.

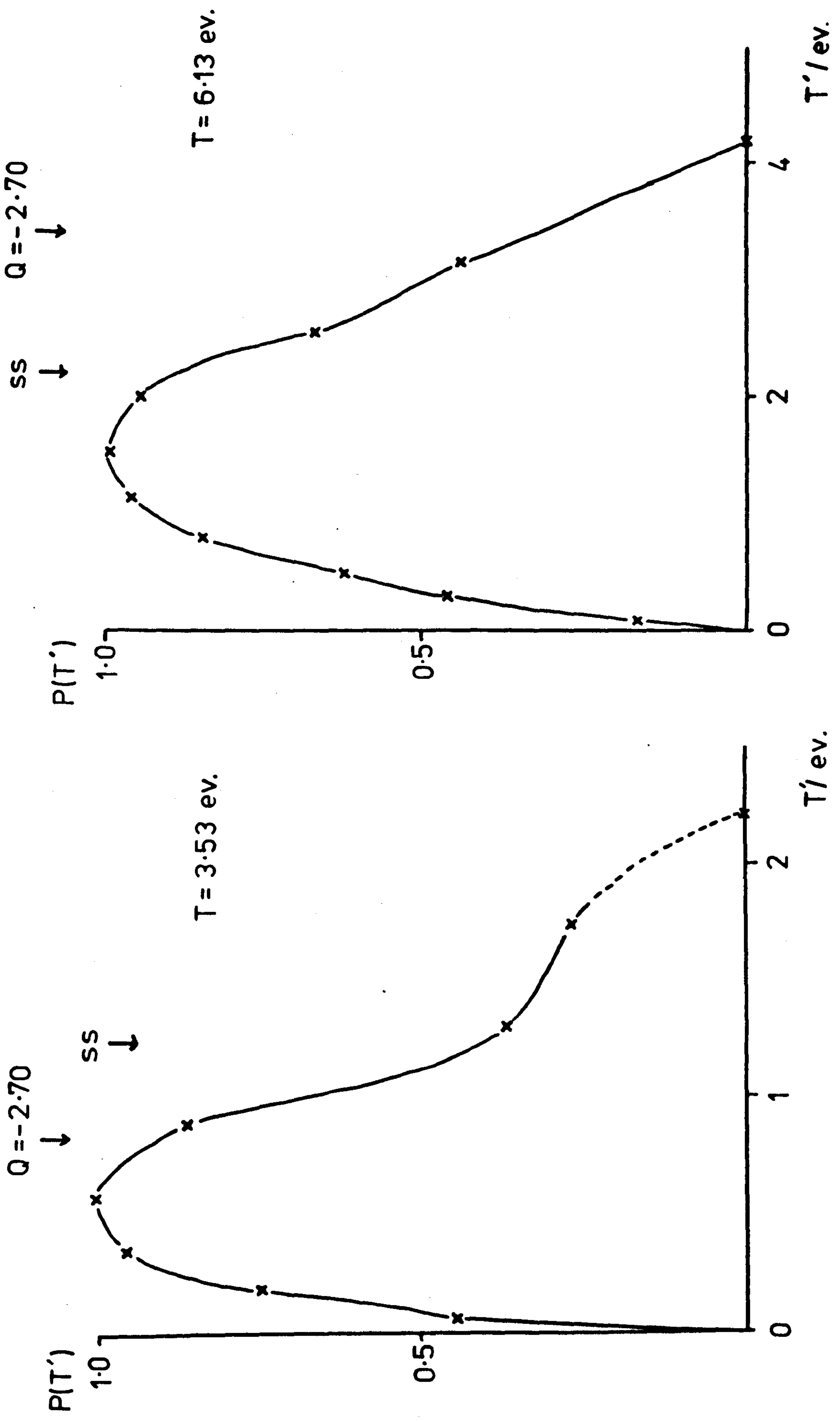

Figure 57. Product translational energy distribution, P(T′), of the reaction $CO^+ + NO = (NCO)^+ + O$ for initial energies of 3·53 and 6·13 ev.

the reaction of vibrationally excited CO^+. If this is so, and the CO^+ is 70% in the v=0 state, this indicates that the total cross section is sensitive to the CO^+ vibrational state. Unfortunately it is not possible to investigate the effect of CO^+ vibrational excitation on the total cross section, as the CO^+ vibrational distribution cannot be appreciably varied. The most detailed experimental data on the effect of vibrational excitation on endothermic reactions [91] comes from the application of the principle of microscopic reversibility to detailed rate constants, k(V,R,T), for exothermic reactions. This shows that for A + BC = AB + C vibrational excitation effectively promotes reaction. However very little data exists for reactions of the type AB + CD = ABC + D. While we might predict that vibrational excitation of CD would promote reaction, rather little is known about how vibrational excitation in bonds other than the one broken in atom exchange reactions affects the rate. One obvious way in which AB vibration could be envisaged as increasing the total cross section is by simply relaxing the potential energy requirements for reaction and enabling larger impact parameter collisions to lead to products.

There is a small forward peak in figure 56, just inside the -2.70 ev limit, with a low intensity tail which extends beyond the centre of mass. The spectator stripping velocity lies outside the Q = -2.70 ev circle, so that it is not energetically possible to form products by the stripping mechanism at this energy. As the initial energy is raised the forward peak becomes a more dominant feature of the scattering. Figure 58 shows the contour diagram measured at an initial energy T = 5.01 ev. The forward peak is much narrower and lies just inside the Q = -2.70 ev circle, and at a lower velocity than predicted by the spectator stripping model. The stripping velocity now lies inside the Q = -2.70 ev circle so that at this energy it is energetically possible for ground state reactants to form products by the stripping mechanism. There is still substantial intensity outside the Q = -2.70 ev circle in the forward direction, with the zero contour approximately corresponding to Q = -1.3 ev.

At this energy there is also substantial backward scattering, although no backward peak is apparent within the accuracy of the data. A backward peak first becomes apparent in the contour diagram measured at an initial energy T = 6.13 ev (figure 59). However it is not clear whether the appearance of the backward peak at this energy is due to the operation of product stability restrictions or some other factors. The sharp minimum at the centre of mass at this energy may indicate that product stability restrictions have started to operate. For the NCO^+ isomer, assuming ground electronic and vibrational state reactants, consideration of the energy and angular distributions of the primary beams indicates that product stability restrictions would not be expected to operate at this energy. This will be discussed in detail below. Figure 59 shows that at an initial energy of 6.13 ev the intensity has contracted so that little lies outside the Q = -2.70 ev circle (see figure 57, the P(T') distribution at this energy). This is observed at all

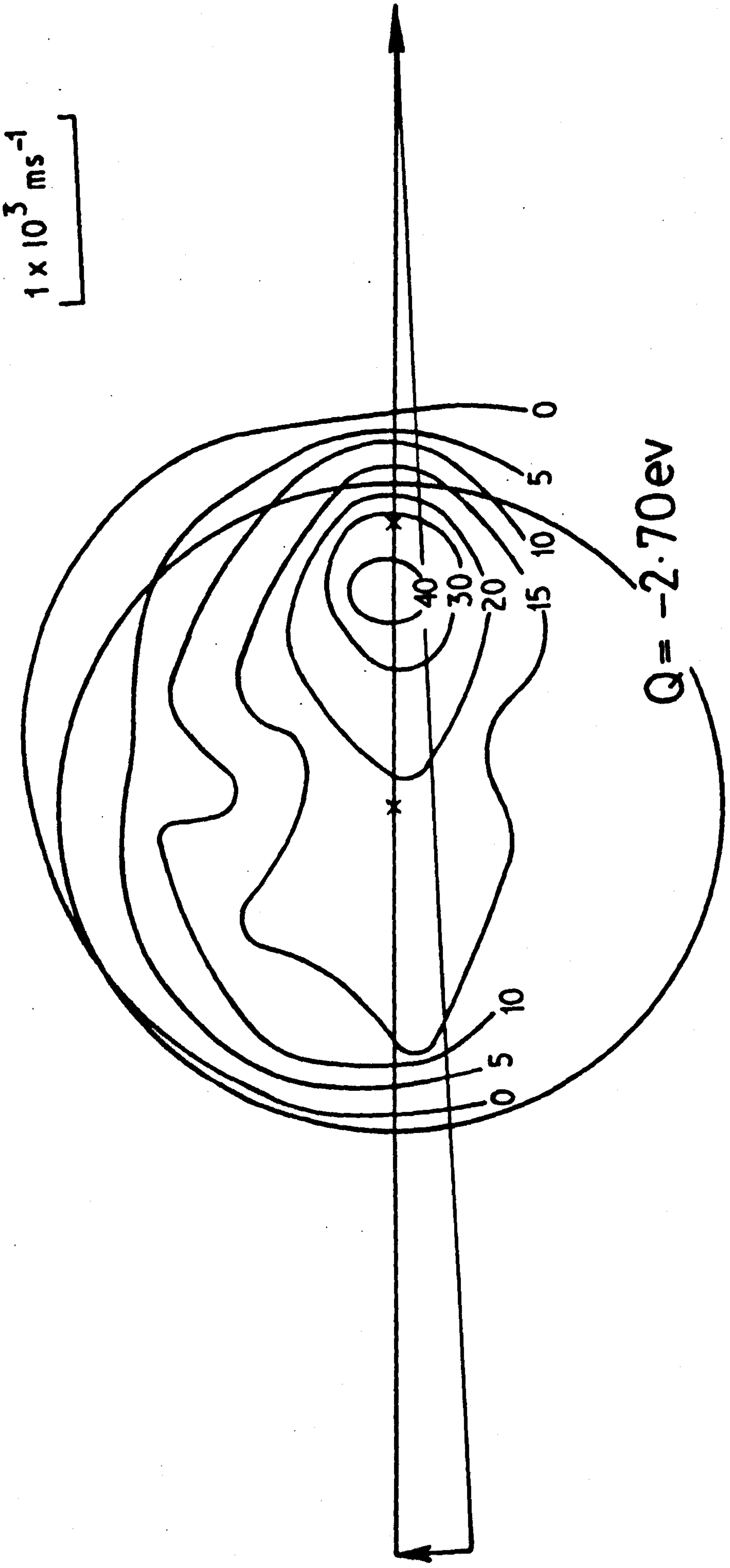

Figure 58. Contour map of intensity of $(NCO)^+$ from $CO^+ + NO$ collisions for initial energy of 5·01 ev.

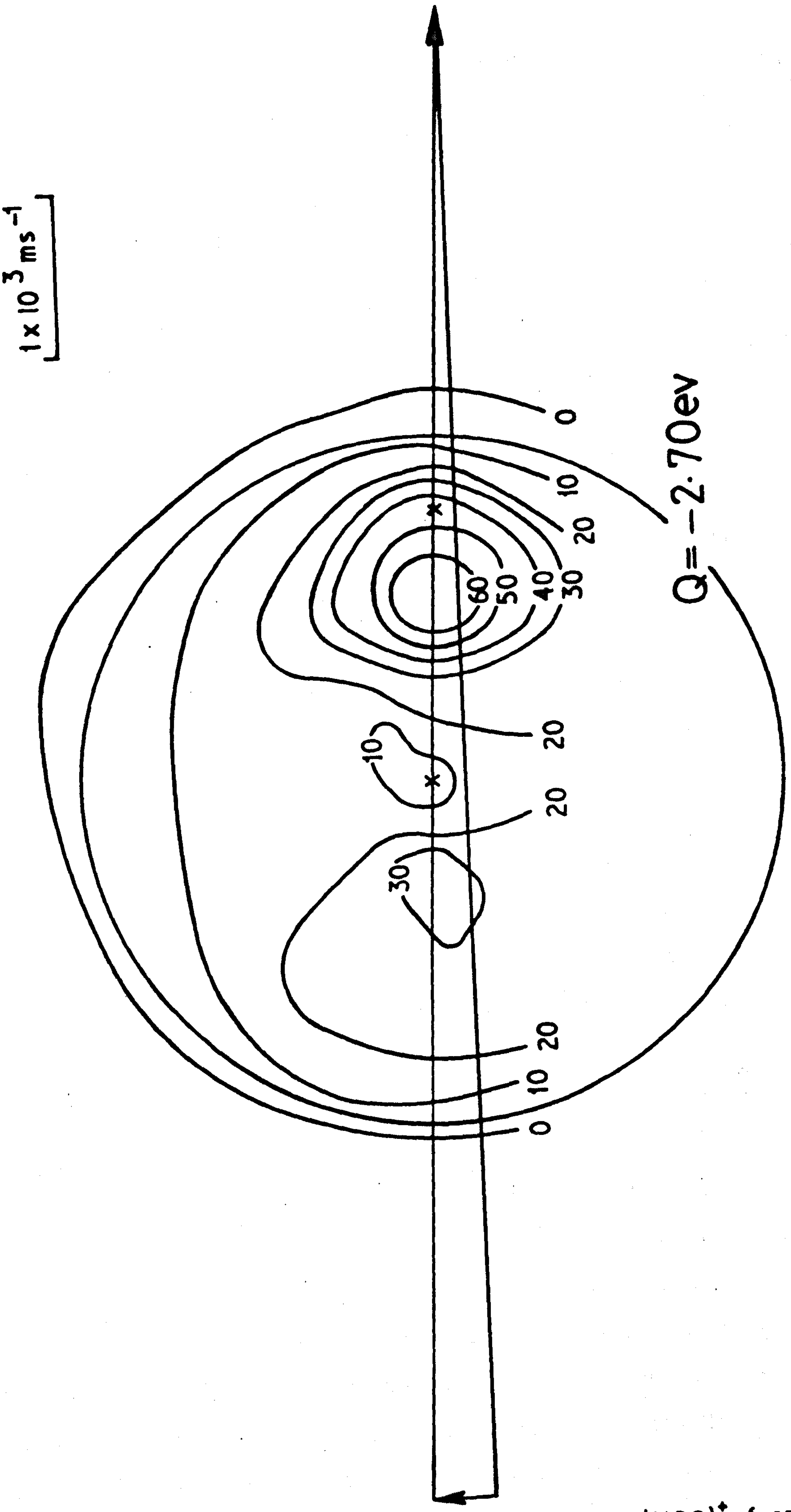

Figure 59. Contour map of intensity of $(NCO)^+$ from $CO^+ + NO$ collisions for initial energy of 6·13 ev.

energies above 6.13 ev. In contrast, for CO_2^+ the intensity was found to contract within the equivalent Q = -0.81 ev circle as the initial energy was raised.

As the initial energy is raised further product stability restrictions begin to dominate the dynamics (see figures 61 and 62). In the low energy regime where product stability restrictions do not strongly influence the dynamics a plot of the most probable translational exoergicity (Q_{MP}) against initial energy (T) (figure 60) is a straight line given by $Q_{MP}(T) = -0.49\ (\pm 0.20) - 0.715\ (\pm 0.037)\ T$ ev (least squares analysis, ± estimated standard deviation). The points for this plot were derived from the maxima in the product ion LAB energy distributions. Compared with the predictions of the spectator stripping model ($Q_{MP} = -0.644.T$) it is clear that the line is offset from the predictions of this model with the deviation increasing slightly the initial energy is raised. The observation that the internal excitation increases more rapidly than spectator stripping predictions appears to be a common feature of reactions of this type. Similar behaviour was found in reactions 4.1 and 5.1. This is in contrast to the well studied hydrogen atom and proton transfer reactions, where spectator stripping or elastic spectator stripping models generally provide good agreement with experimental results. These results indicate coupling of the motion of all atoms in reactive collisions. We are unable to derive a simple model which could be used to rationalise this behaviour. A quantitative explanation of these results may have to await trajectory calculations on high quality

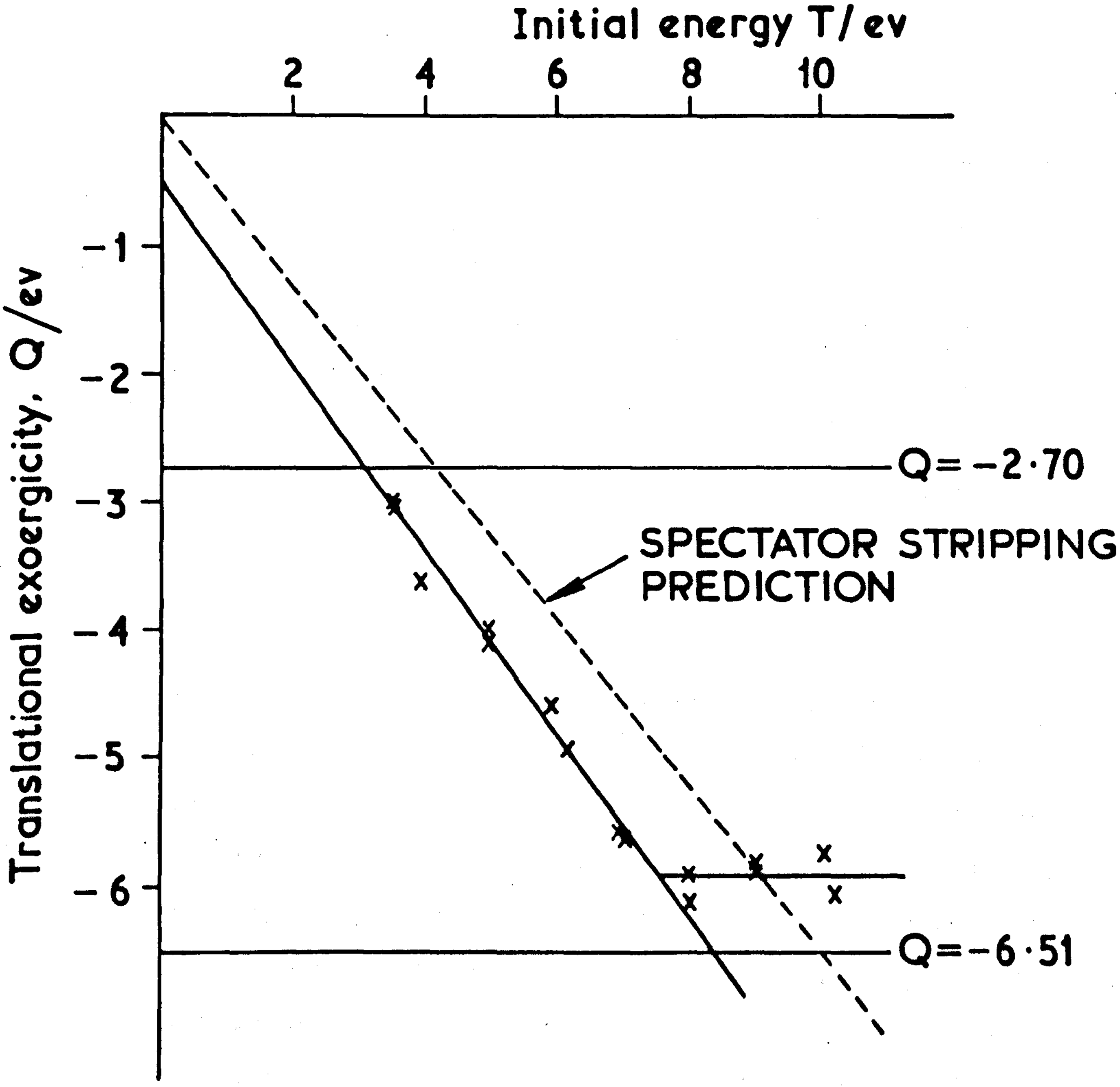

Figure 60. Plot of most probable translational exoergicity (Q_{mp}) versus initial energy (T) for the reaction $CO^+ + NO = (NCO)^+ + O$.

potential energy surfaces. Figure 57 shows that the product translational energy distributions in the low energy regime also peak at energies substantially below spectator stripping predictions.

Table 2 shows a summary of the experimental results from the Q_{MP} vs T plots for the reactions 4.1, 5.1, and 6.1. Presumably the extent of the deviation of the line from spectator stripping predictions is a measure of how closely the four atoms are coupled in reactive collisions. From these results it would appear that reaction to form $(NCO)^+$ occurs on a potential energy surface in which the four atoms are not as closely coupled as in collisions which yield CO_2^+.

The observation of a non-zero intercept in the Q_{MP} vs T plot is not uncommon, however an intercept as large as this has not been reported previously. From table 2 there appears to be a correlation between intercept and reaction exoergicity. Franklin and Haney [92] have reported a linear relationship between product translational energy and reaction exothermicity for a series of hydrogen atom transfer reactions at thermal energy. In general some degree of correlation between product translational energy (or intercept as in these measurements) and reaction exoergicity might be expected, but clearly the partitioning of reaction exoergicity between internal and translational energy will depend on the details of the potential surfaces involved. It is however attractive to suggest that the substantial negative intercept observed here is related to the features of the potential surface due to reaction endoergicity. A

TABLE 2. Summary of experimental results from plots of Q_{MP} vs T.

Reaction		Experiment		Spectator stripping	
	$-\Delta E$/ev	slope	intercept/ev	slope	intercept/ev
$CO^+ + O_2 = CO_2^+ + O$	+0.58	-0.842 (±0.029)	+0.11 (±0.10)	-0.682	0
$CO^+ + NO = CO_2^+ + N$	-0.81	-0.813 (±0.019)	-0.04 (±0.08)	-0.703	0
$CO^+ + NO = (NCO)^+ + O$	-2.70	-0.715 (±0.037)	-0.49 (±0.20)	-0.644	0

Confidence limits represent ± estimated standard deviation from least squares analysis.

number of models have been concerned with non-zero intercepts in Q_{MP} vs T plots. In particular the polarisation stripping model [31] ascribes this to the difference between the ion-induced dipole potential for reactants and products. It seems likely that any contribution this makes in these reactions is small in comparison with the chemical forces.

For the reaction A + BC = AB + C the assumption of the ideal stripping model is that atom transfer occurs without transfer of momentum to the spectator C. Product internal energy is given by the relative energy between the ion and abstracted atom. This model is strictly applicable only to thermoneutral reactions. For exoergic reactions the reaction exoergicity is often arbitrarily added to the product internal energy. This is consistent with experimental results. We could relate this to an attractive or early downhill surface [90] in which a large part of the released potential energy appears as product vibration. The converse, a repulsive or late downhill surface results in product translation. There is little experimental data on endoergic reactions. However, treating endoergic reactions in an analogous manner, if the barrier to reaction occured early (ie early uphill surface) a large part of the energy to overcome the barrier would be derived from energy which in a thermoneutral reaction would become product internal energy. Whereas if the barrier were late (ie late uphill surface) the energy to overcome the barrier would be derived from product translation. The results for reaction 6.1 suggest that most of the energy to overcome the barrier due to the 2.70 ev reaction endoergicity is derived from energy which in a thermoneutral reaction would become product vibration, suggesting that reaction occurs on an early uphill surface. This is not surprising since it is a well known concept in molecular dynamics that translational energy is effective in overcoming early barriers but ineffective in overcoming late barriers, for which reactant vibration is preferred.

Figure 61 shows the contour diagram measured at an initial energy T = 7.93 ev. There is a forward peak just inside the Q = -6.51 ev stability circle, and a lower intensity backward peak. In addition there is substantial wide angle scattering. A clear dissociation threshold is evident around the Q = -6.51 ev circle, although the dissociation threshold is not sharp and the maximum is displaced from the Q = -6.51 ev circle. A plot of the most probable translational exoergicity against initial energy in this energy regime (figure 60) shows that the most probable translational exoergicity is invariant with initial energy as the forward peak is "eaten away" by product stability restrictions. Above some features of the contour diagram measured at T = 6.13 ev were noted which suggested premature operation of product stability restrictions, and here it is evident that the most probable translational exoergicity is displaced from the Q = -6.51 ev line by significantly more than would be expected from consideration of experimental resolution. This suggests that substantial components of the product are derived from the reaction of vibrationally excited CO^+ in the high energy regime as well as at low energy. In addition there exists the possibility that a substantial fraction of the product is the less stable

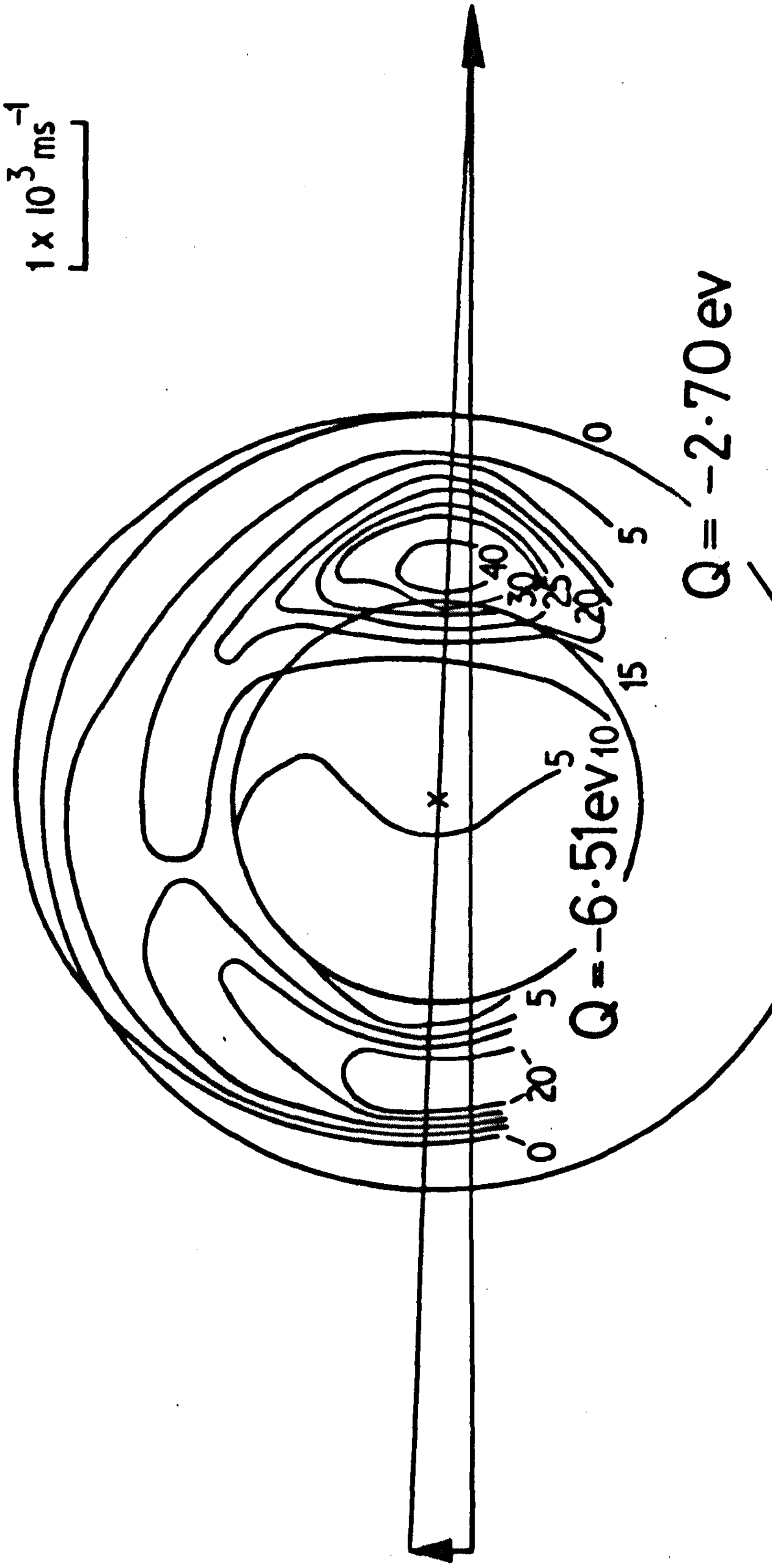

Figure 61. Contour map of intensity of (NCO)⁺ from CO⁺+ NO collisions for initial energy of 7·93 ev.

isomer CNO , which may undergo adiabatic dissociation to the lowest energy fragments C + NO^+.

Although most of the intensity lies outside the Q = -6.51 ev circle, a small but significant amount of intensity lies inside the circle indicating that a small component of the product is electronically excited at this initial energy.

Figure 54 shows that the total cross section for CO_2^+ formation declines sharply when product stability restrictions begin to operate. However, the total cross section for $(NCO)^+$ formation continues to rise after the operation of product stability restrictions. Consideration of the contour diagrams and 3D-CM angular distributions show that there is an increase in backward and wide angle scattered intensity as the initial energy is raised above 6 ev. This may simply be a consequence of the product stability restrictions with low impact rebound collisions in which all atoms strongly interact leading to product recoil and stable product whereas collisions which lead to forward scattering cannot. However the substantial increase in backward scattered intensity suggests the possibility that an alternative mechanism is becoming important in this high energy regime. This could involve the formation of the less stable isomers NOC^+ and CNO^+ by "stripping" of C^+ by NO.

Figure 62 shows the $(NCO)^+$ intensity contour diagram measured at an initial energy of T = 10.22 ev. The forward peak has been further "eaten away" by product stability

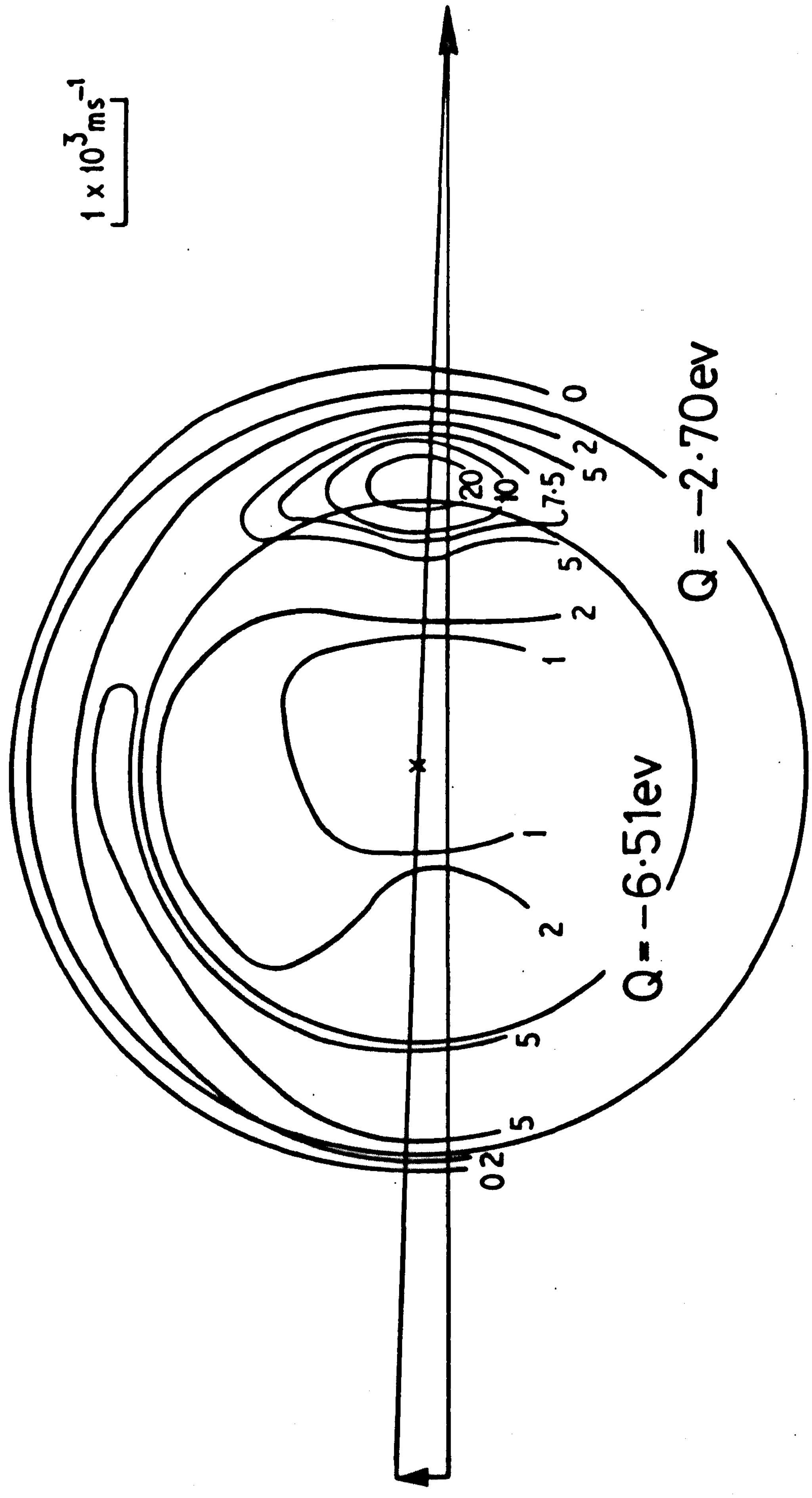

Figure 62. Contour map of intensity of $(NCO)^+$ from $CO^+ + NO$ collisions for initial energy of 10·22 ev.

restrictions but is retained having been shifted to higher velocity, and lies just inside the ground state product stability zone. It seems likely that at this energy to achieve the required forward recoil the forward scattered product is derived from intimate collisions in which all atoms strongly interact enabling substantial momentum transfer to occur between the incipient products. In addition there is a less intense backward peak with a ridge of intensity just inside the ground state stability zone which extends around to $\chi \approx 90°$. The 3D-CM angular distribution shows that the product is mainly backward scattered at this energy. There is substantial intensity inside the Q = -6.51 ev circle indicating that some of the product, either $(NCO)^+$ or O (or both), is electronically excited. There appears to be no clear second dissociation threshold as was evident in the data for CO_2^+ product, so that it is not possible to make any suggestions as to which product is excited as was possible for the CO_2^+ + N products. Figure 63 shows the product translational energy distribution at this energy. The maximum in the distribution occurs at a translational energy just above the Q = -6.51 ev limit and although a significantly smaller proportion of the product is electronically excited here than for CO_2^+ product at this initial energy, in terms of relative intensities, only marginally more intensity lies inside the ground state stability circle for CO_2^+ than for $(NCO)^+$. This is a consequence of the larger total cross section for $(NCO)^+$ formation than for CO_2^+ formation at this initial energy.

The observation that the $(NCO)^+$ ground state forward

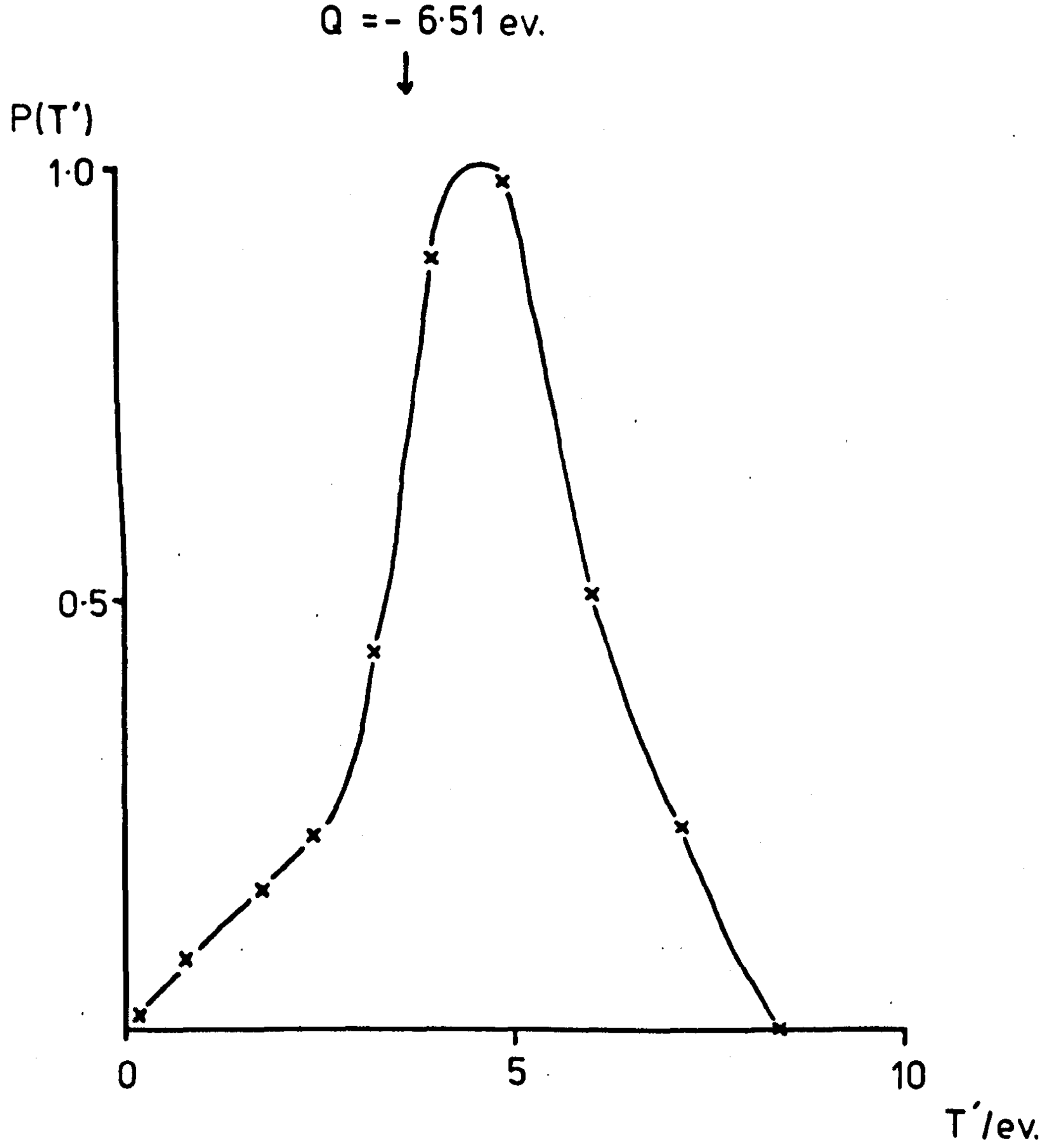

Figure 63. Product translational energy distribution, P(T′), of the reaction $CO^+ + NO = (NCO)^+ + O$ for initial energy of 10·22 ev.

peak is retained whereas the forward peak for CO_2^+ lies in the stability zone for electronically excited product is not consistent with the view that direct forward recoil of products is related to features of the potential surface due to reaction exoergicity. As noted above it seems likely that forward scattered product arises from intimate collisions in which all atoms strongly interact. The predominence of $(NCO)^+$ may reflect the fact that in hard intimate collisions of this type (in which several impulsive collisions between the individual atoms could be envisaged) there is statistically more chance that the product is $(NCO)^+$ rather than CO_2^+. This explanation may also rationalise the increase in backward scattered intensity observed in the high energy regime and the larger total cross section for $(NCO)^+$ formation than for CO_2^+ formation.

CHAPTER 7.

Conclusions and recommendations.

The substantial experimental results described in the preceeding chapters amply demonstrates the potential of the crossed beam apparatus developed in this work. With the recent addition of a microcomputer to handle data reduction there remains perhaps one area in which the instrument could be improved. Although the differentially pumped capillary array has been trouble free throughout this work, the substantial increase in intensity obtainable from a nozzle source would make it attractive, although substantial modifications would be required to accomodate the increased pumping capacity.

The aim of this work has been to investigate the dynamics of a series of ion-molecule reactions of the type

$$AB^+ + CD = ABC^+ + D$$

The reactions studied have shown a number of interesting features. All the reactions were found to proceed by a direct mechanism over the energy range studied although there is substantial evidence for the coupling of the motion of all atoms in reactive collisions. At high energy the total cross sections decline as the dynamics become dominated by product stability restrictions and there is evidence for the formation of electronically excited product. There are a number of features of the dynamics of the reactions studied in this work which remain to be explained and it is hoped that these results will stimulate theoretical work. The failure of the simple models (which have been so successful in rationalising the dynamics of hydrogen atom and proton transfer reactions) when applied to the reactions studied here, reinforces the idea that hydrogen atom and proton transfer reactions are special cases in which the dynamics are dominated by kinematics and long range forces.

The application of beam techniques to study the dynamics of ion-molecule reactions has progressed rapidly since the pioneering work in the 1960's. The dynamics of the reactions of an atomic ion with a diatomic molecule are now relatively well understood, as are proton transfer and H atom abstraction reactions. It seems that future work should proceed in at least two directions. The programme, initiated at Warwick, to study the dynamics of the reactions of diatomic ions with diatomic molecules should be continued to provide a larger data base. In addition work should be extended to more complicated systems with interest focussing on reactions which proceed through an intermediate complex. The application of beam techniques to studying the dynamics of unimolecular reactions by measuring the angular and velocity distributions of the products has, perhaps surprisingly, only been extensively exploited in the field of neutral-neutral chemistry.

REFERENCES.

1. a) R Grice, Adv Chem Phys, 30, 247, (1975).

   b) D L King and D R Herschbach, Disc Farad Soc, 55, 331, (1973).

   c) F Engelke, J C Whitehead, and R N Zare, Disc Farad Soc, 62, 222, (1977).

   d) M J Berry, Ann Rev Phys Chem, 26, 259, (1975).

   e) D R Herschbach, Pure & Appl Chem, 47, 61, (1976).

   f) S H Bauer, Ann Rev Phys Chem, 30, 271, (1979).

2. "Reaction Rate Handbook", 2nd Edn, M H Bortner and J Baurer (editors), Defense Nuclear Agency, 1972.
3. A A Wu and Ch Schlier, Chem Phys, 28, 73, (1978).
4. W R Gentry, in "Gas Phase Ion Chemistry", Vol 2, M T Bowers (editor), Academic Press, 1979.
5. D R Herschbach, Adv Chem Phys, 10, 332, (1966).
6. R Wolfgang and R J Cross Jr, J Chem Phys, 73, 743, (1969).
7. S Chapman and R K Preston, J Chem Phys, 60, 650, (1974).
8. J R Krenos, R K Preston, R Wolfgang, and J C Tully, J Chem Phys, 60, 1634, (1974).
9. A Pipano and J J Kaufman, J Chem Phys, 56, 5258, (1972).
10. P K Pearson and E Roueff, J Chem Phys, 64, 1240, (1976).
11. D M Hirst, Mol Phys, 35, 1559, (1978).
12. B H Mahan, J Chem Phys, 55, 1436, (1971).

13. a) R M Bilotta, F N Preuninger, and J M Farrar, J Chem Phys, 72, 1583, (1980).

b) J A Fair and B H Mahan, J Chem Phys, 62, 515, (1975).

14. a) G Bosse, A Ding, and A Henglein, Z Naturforsch, 26A, 932, (1971).

b) A Henglein, J Phys Chem, 76, 3883, (1972).

c) C H Douglass, D J McClure, and W R Gentry, J Chem Phys, 67, 4931, (1977).

15. W B Miller, S A Safron, and D R Herschbach, Disc Farad Soc, 44, 108, (1967).

16. A Lee, R L Leroy, Z Herman, R Wolfgang, and J C Tully, Chem Phys Letts, 12, 569, (1972).

17. C E Klots, J Chem Phys, 64, 4269, (1976).

18. Z Herman, A Lee, and R Wolfgang, J Chem Phys, 51, 452, (1969).

19. Z Herman and K Birkinshaw, Ber Bunsenges Physik Chem, 77, 566, (1973).

20. G H Bearman and W R Gentry, J Chem Phys, 71, 1128, (1979).

21. a) D J McClure, C H Douglass, and W R Gentry, J Chem Phys, 67, 2362, (1977).

b) D J McClure, C H Douglass, and W R Gentry, J Chem Phys, 66, 2079, (1977).

22. R Wolfgang, Acc Chem Res, 3, 48, (1970).

23. W R Gentry, E A Gislason, B H Mahan, and Chi-wing Tsao, J Chem Phys, 49, 3058, (1968).

24. a) P A Gorry, C V Nowikow, and R Grice, Mol Phys, 37, 347, (1979).

b) B H Mahan and T M Sloane, J Chem Phys, 59, 5561, (1973).

25. G A Fisk, J D McDonald, and D R Herschbach, Disc Farad Soc, 44, 228, (1967).
26. P M Hierl, Z Herman and R Wolfgang, J Chem Phys, 53, 660, (1970).
27. K Lacmann and A Henglein, Ber Bunsenges Physik Chem, 69, 286, (1965).
28. J C Polanyi, Disc Farad Soc, 44, 293, (1967).
29. A Henglein, K Lacmann, and B Knoll, J Chem Phys, 43, 1048, (1965).
30. Z Herman and R Wolfgang, in "Ion-Molecule Reactions", Vol 2, J L Franklin (editor), Butterworths, 1972; and references quoted therein.
31. Z Herman, J D Kerstetter, T L Rose, and R Wolfgang, J Chem Phys, 46, 2844, (1967).
32. J D Kerstetter and R Wolfgang, J Chem Phys, 53, 3765, (1970).
33. C M Connally and E A Gislason, Chem Phys Letts, 14, 103, (1972).
34. P J Kuntz, Chem Phys Letts, 4, 129, (1969).
35. P J Kuntz and A C Roach, J Chem Phys, 59, 6299, (1973).
36. a) T F George and R J Suplinskas, J Chem Phys, 51, 3666, (1969).

    b) T F George and R J Suplinskas, J Chem Phys, 54, 1037, (1971).

    c) T F George and R J Suplinskas, J Chem Phys, 54, 1046, (1971).

37. D T Chang and J C Light, J Chem Phys, 52, 5687, (1970).

38. M L Vestal, A L Wahrhaftig, and J H Futrell, J Phys Chem, 80, 2892, (1976).

39. M L Vestal, PhD dissertation, University of Utah, 1975.

40. D R Herschbach, Appl Opt Suppl, 2, 128, (1965).

41. D R Bates, C J Cook, and F J Smith, Proc Phys Soc London, 83, 49, (1964).

42. B H Mahan, W E W Ruska, and J S Winn, J Chem Phys, 65, 3888, (1976).

43. a) K T Gillen, B H Mahan, and J S Winn, J Chem Phys, 59, 6380, (1973).

    b) B H Mahan and W E W Ruska, J Chem Phys, 65, 5044, (1976).

44. B D Power, N T M Dennis, R D Oswald, and B H Calwell, Vacuum,, 24, 117, (1974).

45. B R Turner, J A Rutherford, and D M J Compton, J Chem Phys, 48, 1602, (1968).

46. M L Vestal, C R Blakley, P W Ryan, and J H Futrell, Rev Sci Inst, 47, 15, (1976).

47. Z Herman and V Pacak, Int J Mass Spect & Ion Phys, 24, 355, (1977).

48. "Quadrupole Mass Spectrometry and its applications", P H Dawson (editor), Elsevier, 1976.

49. J E Campana and P C Jurs, Int J Mass Spect & Ion Phys, 33, 119, (1980).

50. P H Dawson, Int J Mass Spect & Ion Phys, 6, 33, (1971).

51. P H Dawson, Int J Mass Spect & Ion Phys, 17, 423, (1975).

52. a) W M Brubaker, Adv Mass Spect, 4, 293, (1968).
    b) W M Brubaker, J Vac Sci & Tech, 10, 291, (1973).

53. Z Herman, J D Kerstetter, T L Rose, and R Wolfgang, Rev Sci Inst, 40, 538, (1969).

54. B E Evans and R W Supple, J Vac Sci & Tech, 8, 270, (1971).

55. J F J Todd, private communication, 1979.

56. E W McDaniel, V Cermak, A Dalgarno, E E Ferguson, and L Friedman, "Ion-Molecule Reactions", Wiley Interscience (New York), 1970, p 114.

57. N F Ramsey, "Molecular Beams", OUP (London), 1956, p 20.

58. H N Hoskettler and R B Bernstein, Rev Sci Inst, 31, 872, (1960).

59. C V Nowikow and R Grice, J Phys E, 12, 515, (1979).

60. a) J J Valentini, M J Coggiola, and Y T Lee, Discuss Farad Soc, 62, 232, (1977).
    b) P A Gorry, C V Nowikow, and R Grice, Chem Phys Lett, 49, 116, (1977).

61. T S Green, Plasma Phys, 12, 877, (1970).

62. R Jones, Rev Sci Inst, 49, 21, (1978).

63. J A Simpson, Rev Sci Inst, 32, 1283, (1961).

64. See any standard text on electron optics, for example: O Klemperer and M E Barnett, "Electron Optics", 3rd Edn, Cambridge, 1971.

65. D W Mason, Plasma Phys, 6, 553, (1964).

66. "MOS MCS6500 Hardware Manual", MOS Technology Inc, Norristown PA, 1976.

67. R6522 Data Sheet, Rockwell International, 1977.

68. M L Vestal, C R Blakley, and J H Futrell, Phys Rev A, 17, 1321, (1978).

69. M L Vestal, C R Blakley, and J H Futrell, Phys Rev A, 17, 1337, (1978).

70. F T Smith, R P Marchi, and K G Dedrick, Phys Rev, 150, 79, (1966).

71. a) F C Fehsenfeld, A L Schmeltekopf, and E E Ferguson, J Chem Phys, 45, 23, (1966).

b) R S Hemsworth, R C Bolden, M J Shaw, and N D Twiddy, Chem Phys Letts, 5, 237, (1970).

72. N G Adams, D Smith, and D Grief, Int J Mass Spect & Ion Phys, 26, 405, (1978).

73. N Kobayashi and Y Kaneko, J Phys Soc Japan, 37, 1082, (1974).

74. a) D Gauyacq, M Horani, S Leach, and J Rostas, Can J Phys, 53, 2040, (1975).

b) V E Bondybey and T A Miller, J Chem Phys, 67, 1790, (1977).

75. S W Jorgensen and G Sorensen, J Chem Phys, 62, 2550, (1975).

76. G R Mohlmann and F J De Heer, Chem Phys Letts, 43, 170, (1976).

77. J F M Aarts and F J De Heer, Physica (Utrecht), 49, 425, (1970).

78. a) V Cermak and Z Herman, Collect Czech Chem Commun, 30, 1343, (1965).

b) J J Leventhal and L Friedman, J Chem Phys, 46, 997, (1967).

c) M T Bowers, M Chau, and P R Kemper, J Chem Phys, 63, 3656, (1975).

79. K R Ryan and H M Stock, Int J Mass Spect & Ion Phys, 21, 389, (1976).

80. T F Moran, J B Wilcox, and L E Abbey, J Chem Phys, 68, 261, (1978).

81. a) T F Moran and L Friedman, J Chem Phys, 42, 2391, (1965).

b) V E Bondybey and T A Miller, J Chem Phys, 69, 3597, (1978).

c) C R Blakley, M L Vestal, and J H Futrell, J Chem Phys, 66, 2392, (1977).

82. J F Paulson, private communication, 1979.

83. L W Sieck and R Gorden, J of Res of NBS, 78A, 315, (1974).

84. J H D Eland, Int J Mass Spect & Ion Phys, 9, 397, (1972).

85. T E Sharp and H M Rosenstock, J Chem Phys, 41, 3453, (1964).

86. C R Brundle and D W Turner, Int J Mass Spect & Ion Phys, 2, 195, (1969).

87. K E McCulloh, J Chem Phys, 59, 4250, (1973).

88. F C Fehsenfeld and E E Ferguson, J Chem Phys, 56, 3066, (1972).

89. P Kriemler and S E Butrill, JACS, 95, 1365, (1973).

90. J C Polanyi, Acc Chem Res, 5, 161, (1972); and references quoted therein.

91. C B Moore and I W M Smith, Farad Disc Chem Soc, 67, 146, (1979).

92. J L Franklin and M A Haney, J Phys Chem, 73, 2857, (1969).